POLITECNICO DI TORINO

Corso di laurea in Ingegneria Aerospaziale

Tesi di Laurea Magistrale

Micromechanics analysis of fiber-reinforced composites

Relatori

Prof. Erasmo Carrera

Prof. Marco Petrolo

Candidato

Michele Magnetta

Supervisore esterno

University of Massachusetts Lowell

Prof. Marianna Maiarù

Luglio 2018

Dedica

Abstract

The fiber-reinforced composite materials are now widely used also in sectors different from the aerospace one. The main problem of the composite structural parts design is to understand how they can fail. Considering the small diameters of the fibers, the failure analysis on this kind of materials should be done at micro-scale using the micro-mechanics. This thesis work proposes an innovative approach to the problem able to reduce the computational time and to obtain consistent results in reduced time. Indeed the code that will be used is based on the Carrera Unified Formulation (CUF) and the matrix with fibers cells are modelled through the 1D formulation that requires the use of beam elements and Lagrange polynomials to define the cross-section. The failure analysis is based on the crack band theory that was implemented by the Professor Marianna Maiarù during her PHD work. This work is organized as follows: an introduction to composite material and laminates is provided in chapter 1, a brief theoretical introduction to 1D (CUF) together with the description of the pardiso library implementation is given in chapter 2, static analysis are replicated in order to acquire manual skills with the code in the chapter 3, a brief reference to micromechanics is given in chapter 4 and finally in the chapters 5 and 6 are reported the achieved results of progressive failure analysis and the conclusions.

Contents

Chapter 1

Introduction

In this chapter composite materials structure, their properties and modes of failure will be described while, in the last subsection, computational cost for a failure analysis will be considered.

1.1 Typical Structure and laminates

By the term "composite materials" are defined all the materials composed of fiber reinforcements and a matrix (Fig. 1.1[1]). The fibers give strength and stiffness to the materials while the matrix has the task of binding the fibers together, in this way the matrix transfer applied load to the fibers and also protects them from the environmental attack. Composites are anisotropic materials because their properties vary as a function of fiber direction, indeed they have hight values of young modulus (E) long the fibers direction whereas in the transverse direction it has a significant drop off because the most of the applied loads are absorbed by matrix. For there reasons the laminates were invented (Fig. 1.2[2]) and in order to improve the mechanical properties in other direction, layers were added with fibers in different direction. For example, to improve the behavior of laminates in the transverse direction, a cross-ply laminates [0°/90°] is used.

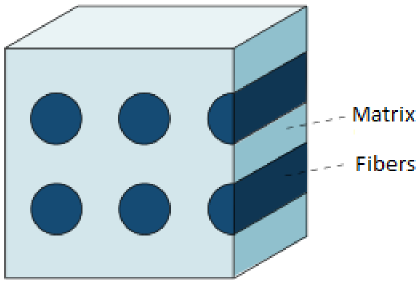

Figure 1.1: Composite material structure

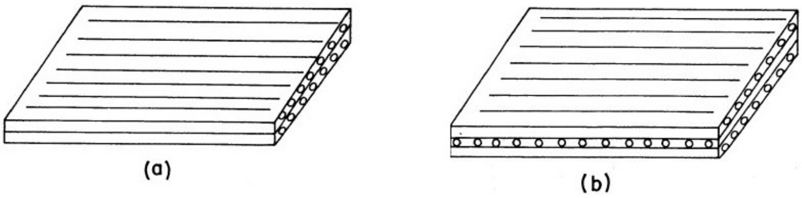

Figure 1.2: (a)=Simple laminate; (b)=Cross-ply laminate

1.2 Properties and applications

The "composites materials" offer many advantage compared to the traditional metallic materials, the main ones are:

- High strength long the fiber direction;
- Light weight and small basis weight;
- Radar transparency;

For these reasons they are widely used in aeronautical industry, where weight and density are among the most important factors. A composite structures could have higher stiffness and lower density than an aluminium made one, in the table 1.1 are compared the mechanical properties between two typical aluminum alloys (Dural and Ergal) and a laminate composed by carbon fibers (All in the same direction), and epoxy resin [3]. It is possible to understand by the data that a composite laminate is lighter than an aluminium alloy plate with the same dimension but it has a better values of the young modulus only long the fibers direction (134000 MPa vs 73000 MPa), indeed in the transverse direction this value fall down from 134000 MPa to 7000 MPa and it is significantly lower than the young modulus of aluminum alloy.

Table 1.1: Materials properties

Material	$E_l[MPa]$	$E_t[MPa]$	$\gamma[Kg/dm^3]$	Saving in γ
Dural-Ergal	73000	73000	2.8	-
Carbon fibers laminate	134000	7000	1.53	46 %

From 1970 to nowadays, the composite materials percentage used for Commercial Aircraft components has been rising. The Fig. 1.3 [4] shows this trend over the years, Airbus A350 and the Boing 878 are the first ones to overcome the 50% of total weight for the composite components and the value is expected to rise over the nest few years.

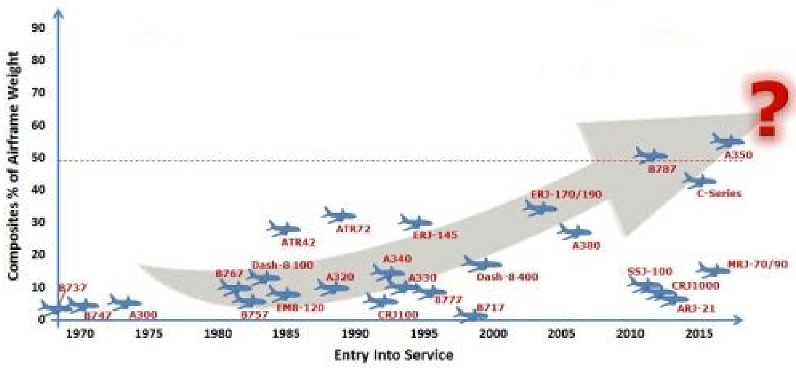

Figure 1.3: Percentage trend of composite weight parts in commercial transport airplanes

1.3 Failure

Composite materials laminates have different failure types, if compared to isotropic materials, due to their complex structure (Fig. 1.4). The critical zones are: the fiber-matrix interface and the lamina-lamina interface because both the parts are stuck together and if the glue fail, the whole laminate could fail. Below are reported the mains ones failure ways:

- Matrix failure due to transverse traction loads (Fig. 1.7) [5];
- Fibers failure due to applied loads (Fig. 1.6) [6] ;
- Delamination (Fig. 1.5) [7];
- Debonding between fiber and matrix (Fig. 1.5) [8];

In this thesis work only one type of failure will be considered, ie the matrix failure due to transverse traction loads. Will be analyzed only a very small part of a generic structure composed by five fibers, it is in the micron ($10^{-6}m$) order of size. This study approach is called micromechanics because study is concentrated only in one point of the whole structure.

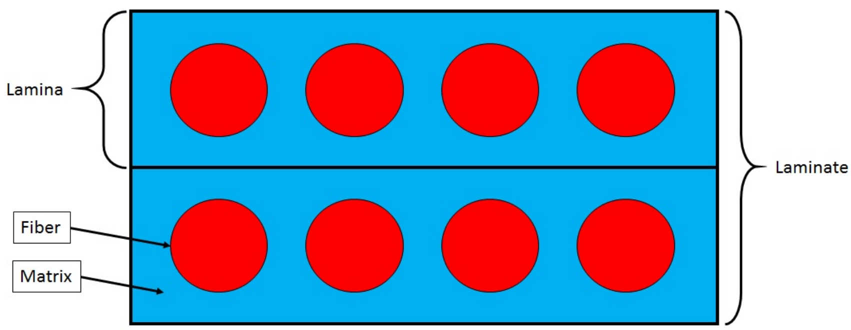

Figure 1.4: Simple laminate structure

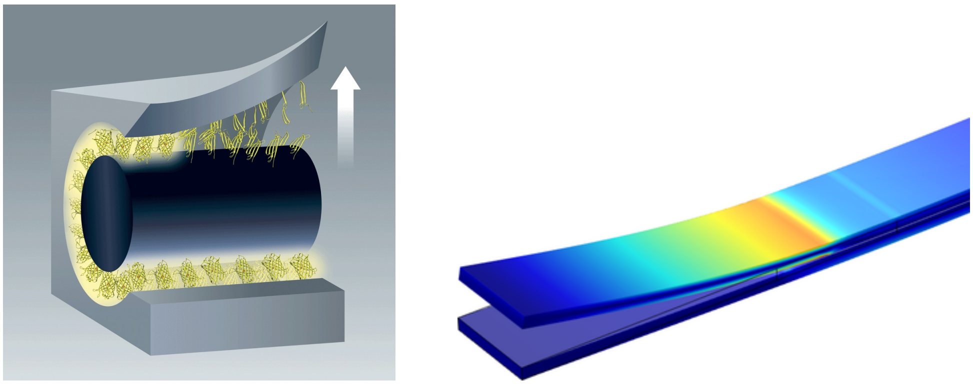

Figure 1.5: Fiber-matrix debonding (on the left) and delamination (on the right) examples

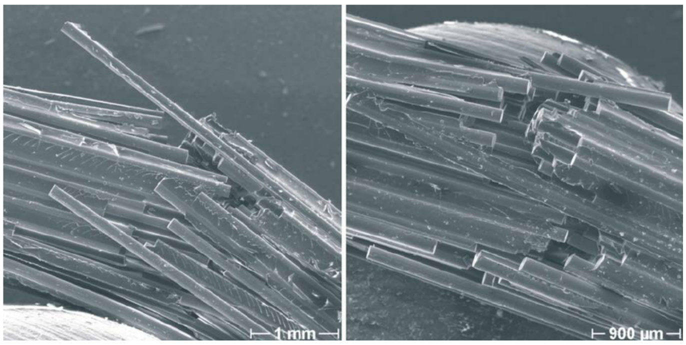

Figure 1.6: Fiber fracture example

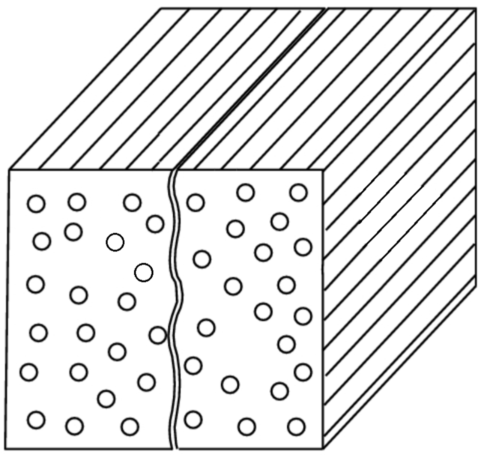

Figure 1.7: Matrix fracture example

1.4 Finite element method (FEM)

Except for some simple cases, the differential equations of a structural problem, combined with the boundary condition, do not allow analytical solution. It is necessary to switch from the strong form to weak form of the problem system equation, in other words the system equation must be satisfied globally and no punctually in the problem domain. Mathematically the system equation switch from differential formulation to integral formulation, however this switch is not sufficient to find a problem solution. To overcome this issue finite element method was invented, using this method the entire domain is divided into a small parties called finite elements and each of them is composed by a finite number of point called nodes. The solution is evaluated only in the nodes, and in all the other points it is interpolated by particular functions called shape function. So the entire domain must be discretized as shown in Fig. 1.9 [9], but the discretizaion inevitably forms a gap between the physical and computational domain and only the increment in the finite element number can reduce it. If one or two problem dimension are predominant over the other, it is possible to reduce the 3D problem to 2D or 1D problem, e.g. a 3D blade can be discretized by simple beam elements. Solve a structural problem means to find the displacement field $u(x, y, z)$ that is a 3D function in the three coordinates x,y and z. It is possible write a complex and unknown function f(x,y,z) as a infinite summation of simple functions $\phi(x, y, z)$ times a coefficient c:

$$\mathbf{f}(\mathbf{x}, \mathbf{y}, \mathbf{z}) = \sum_{n=1}^{\infty} c_n \phi_n(x, y, z) \tag{1.1}$$

For numerical solution it is impossible to have infinity summation, so the term "n" vary from 1 to the total number of the structural nodes and in addition:

- The generic function f(x,y,z) turn into u(x,y,z) for structural problem;
- The constants c_n turn into u_n that are the nodal displacement;

- The functions ϕ turn into N that are the shape function;

$$\mathbf{u(x,y,z)} \simeq \sum_{n=1}^{N_tot} u_n N_n(x,y,z) \tag{1.2}$$

For instance, one beam element composed by two nodes and linear shape function is now considered (Fig. 1.8). The displacements in the nodes are u_1 and u_2 and the two shape function are: $N_1(x) = 1-x$ and $N_2(x) = x$ (where x is the beam axis). So the displacement in a generic beam point of coordinate x can be write as:

$$\mathbf{u(x)} = u_1 N_1 + u_2 N_2 \tag{1.3}$$

Solve a structural problem using 3D elements is computationally expensive, but it is possible to obtain good results, in a reasonable time, using an axiomatic method based on Carrera unified formulation (CUF). This method use only beam elements along y direction and 2D shape function F(x,z) to describe the behaviour of the cross-section, so the 3D displacement field became:

$$\mathbf{u(x,y,z)} = \sum_{i=1}^{N_tot} N_i(y) F_\tau(x,z) u_{\tau i} \tag{1.4}$$

where τ is related to the polynomial degree F(x,z) used to describe the cross-section. In the Fig. 1.10 [9] are shown the main differences between the classic 3D FEM model and 1D CUF model, the choice of the function F(x,z) is arbitrary and in the next chapter will be present two polynomials class: Taylor and Lagrange.

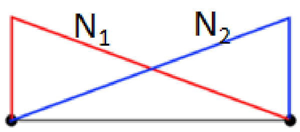

Figure 1.8: Beam element with shape funtions

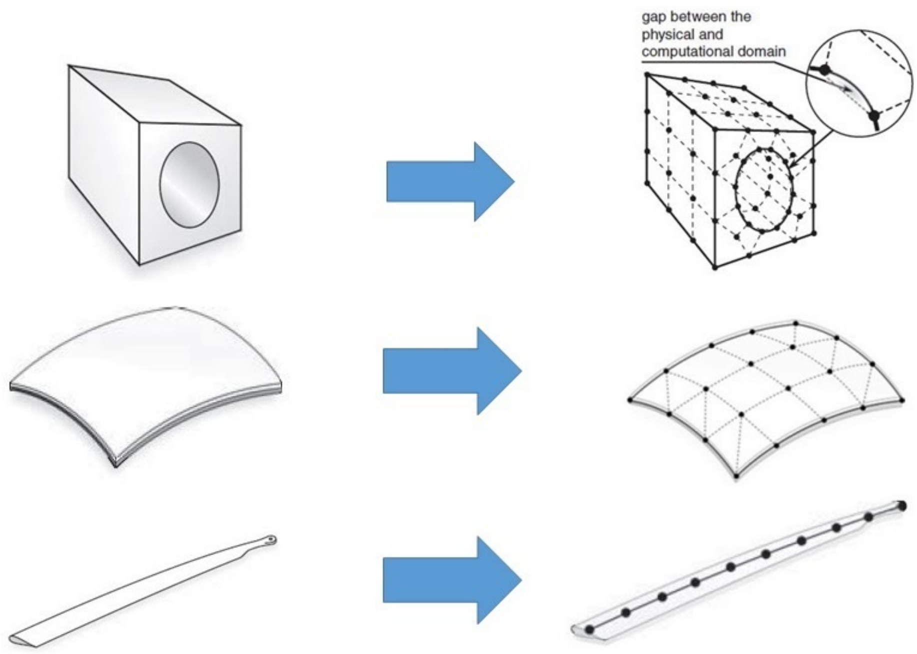

Figure 1.9: Domains discretization

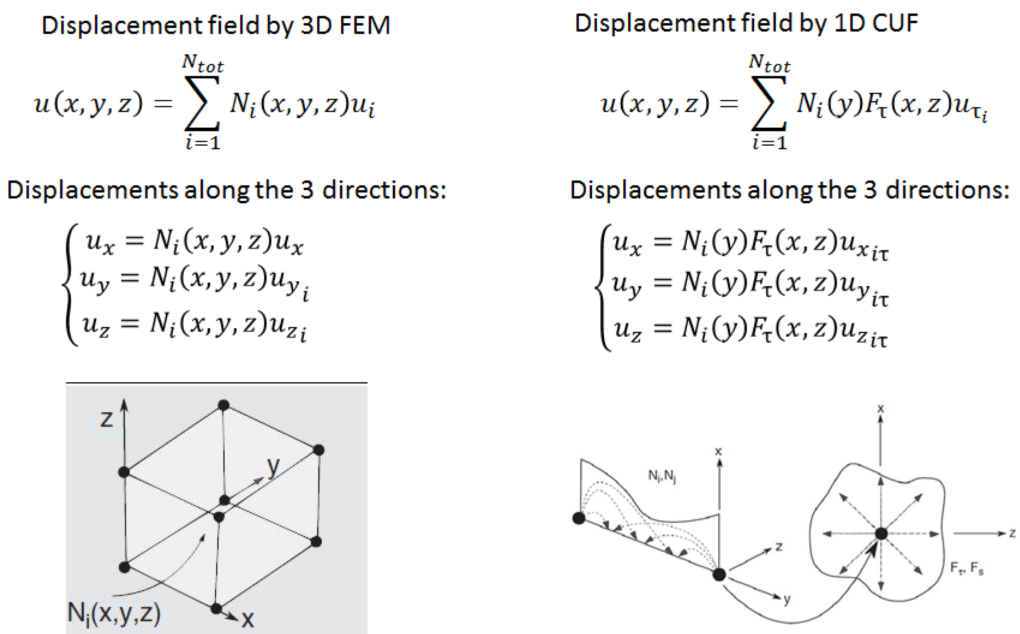

Figure 1.10: 3D Classical FEM v.s. CUF 1D

Chapter 2

Carrera unified formulation

Carrera unified formulation "is a new approach for the derivation of FE matrices" [9], indeed stiffness matrix [k] and all the other FE vectors are derived in terms of "fundamental nuclei". The fundamental nucleus is an (3 by 3) array and is defined by four indexes τ, s, i and j but, key thing, "its form does not change for 1D,2D or 3D problems" [9].

2.1 Principle of virtual work (PVW)

To derive the fundamental nucleus, it is necessary to use the PVW. So in this subsection it is briefly explained and a simple structural example is also shown. First of all it is necessary define the virtual variation (δ), it is an infinitesimal variation of the quantity that must be respect the congruence and the boundary condition. Now let's consider two system "a" and "b":

- System "a" is composed by real stresses $\{\sigma^a\}$ and forces $\{F^a\}$, it respect the equilibrium conditions: $\sum F_i^a = 0$ and $\sum M_i^a = 0$;
- System "b" is composed by virtual strain $\{\delta\epsilon\}$ and displacements $\{\delta u^b\}$, it respect the congruence (no tear in the body) and boundary condition;

In the static case, the PVW indicates that: the virtual work done by real stresses time virtual strain is equal to the virtual work done by the real forces time the virtual displacements:

$$\delta W_{int} = \delta W_{ext} \tag{2.1}$$

Where:

- $\delta W_int=$ virtual internal work variation$=\int\{\sigma^a\}^T \times \{\delta\epsilon\}^b dV$;
- $\delta W_ext=$ virtual external work vatiation$=\sum\{F_i^a\}^T \times \{\delta u_i^b\}$;
- $\delta\epsilon=$ virtual variation of strains;
- $\delta u_i=$ virtual variation of displacements;
- $\sigma=$ internal stresses;
- $P_i=$ external forces;

Now it is proposed a simple example of PVW application, tip displacement of cantilever beam will be evaluated. The Fig. 2.1 shows the problem, a vertical force F is applied at the free tip (B) while the other one is fixed. Normal, shear stresses and bending moment along the beam are the following:

- $N_x(x) = 0$;
- $T_y(x) = F$;
- $M(x) = F(x - L)$;

In order to apply the PVW, it is necessary to consider a virtual system, identical, but with a vertical unit load applied at the tip (B). In this case: normal stress, shear stress and bending moment along the beam are:

- $N'_x(x) = 0$;
- $T'_y(x) = 1$;
- $M'(x) = 1(x - L)$;

Now it is possible to write the internal and external work:

$$\begin{cases} \delta W_{ext} = 1 \times \delta u_b \\ \delta W_int = \int_0^L N_x(x) \frac{N'_x(x)}{EA} dx + \int_0^L T_t(x) \frac{T'_y(x)}{GA} dx + \int_0^L M_z(x) \frac{M'_z(x)}{EI_z} dx \end{cases} \tag{2.2}$$

The first term of δW_{int} is null because the normal stress is null along all the beam. Replacing the terms in the principle of virtual work:

$$\delta u_b = \frac{F}{GA} \int_0^L T_t(x) dx + \frac{F}{EI_z} \int_0^L (x - L)^2 dx \tag{2.3}$$

Solving the integrals, it is possible to find the problem solution in term of tip displacement:

$$\delta u_b = \frac{FL}{GA} + \frac{FL^3}{3EI_z} \tag{2.4}$$

The tip displacement δu_b is composed by two terms:

- Shear contribution=$\frac{FL}{GA}$;
- Bending contribution=$\frac{FL^3}{3EI_z}$;

2.2 Fundamental Nucleus derivation

In structural problems the unknown is the displacement field u(x,y,z). In a classical cartesian reference system (x,y,z), it is possible identify three displacement

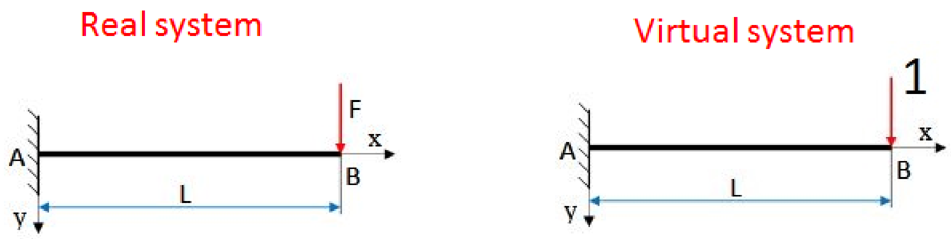

Figure 2.1: Real system on the left and virtual system on the right

components called u_x, u_y and u_z that are dependent by the coordinates x,y and z.

$$\begin{cases} u_x = u_n(x,y,z) \\ u_y = u_y(x,y,z) \\ u_z = u_z(x,y,z) \end{cases} \tag{2.5}$$

These three component can be included in the vector $\{u\}$:

$$\{u\}^T = \{u_x, u_y, u_z\} \tag{2.6}$$

Now, "in according with axiomatic method, it's possible to suppose the behavior of cross-section using F_τ expansion function (Taylor, Lagrange, etc.)" [9] :

$$u = N_i(x)F_\tau u_{\tau i} \qquad\qquad \tau = 1, M; \tag{2.7}$$

Where:

- M= is the number of expansion terms (it can be arbitrary);
- u_τ;= is the vector of unknown displacement;
- N_i= are the shape function

It is now possible to define the virtual variation displacement, it requires two new indexes "j" and "s":

$$\delta u = N_j(x)F_s\delta u_{sj} \qquad\qquad s = 1, M; \tag{2.8}$$

Once know the displacements, it is easy to calculate the six strains components ($\{\epsilon\}^T$=$\{\epsilon_{xx}$; ϵ_{yy}; ϵ_{zz}; ϵ_{zz}; ϵ_{xz}; ϵ_{yz}; $\epsilon_{xy}\}$) and stress ($\{\sigma\}^T$=$\{\sigma_{xx}$; σ_{yy}; σ_{zz}; σ_{xz}; σ_{yz}; $\sigma_{xy}\}$) by the geometrical relations and Hooke's law. The geometrical relations are valid in small displacements hypothesis and connect the displacement with strains by first order derivative:

$$\epsilon_{ij} = \frac{1}{2}\left(\frac{\partial u_i}{\partial x_j} + \frac{\partial u_j}{\partial x_i}\right) \qquad\qquad i, j = x, y, z; \tag{2.9}$$

The Hooke's low connect the strains to the stresses by the material coefficient matric [C]:

$$\{\sigma\} = [C]\{\epsilon\} \tag{2.10}$$

Coefficient matrix is six by six matrix and for composite material in the main orthotropy axes is the following:

$$\mathbf{C} = \begin{bmatrix} C_{11} & C_{12} & C_{13} & 0 & 0 & 0 \\ C_{21} & C_{22} & C_{23} & 0 & 0 & 0 \\ C_{13} & C_{23} & C_{33} & 0 & 0 & 0 \\ 0 & 0 & 0 & C_{44} & 0 & 0 \\ 0 & 0 & 0 & 0 & C_{55} & 0 \\ 0 & 0 & 0 & 0 & 0 & C_{66} \end{bmatrix} \tag{2.11}$$

Replacing the CUF formulation of displacements in the previous relations, the following relations are obtained:

$$\begin{cases} \{\epsilon\} = [b]N_i(y)F_\tau(x,z)\{u\}_{\tau i} \\ \{\sigma\} = [C][b]N_i(y)F_\tau(x,z)\{u\}_{\tau i} \end{cases} \tag{2.12}$$

Where [b] is three by six matrix composed by differential operators:

$$\mathbf{b} = \begin{bmatrix} \partial/\partial x & 0 & 0 \\ 0 & \partial/\partial y & 0 \\ 0 & 0 & \partial/\partial z \\ \partial/\partial z & 0 & \partial/\partial x \\ 0 & \partial/\partial z & \partial/\partial y \\ \partial/\partial y & \partial/\partial x & 0 \end{bmatrix} \tag{2.13}$$

The virtual variation of strains becomes:

$$\{\delta\sigma\} = [b]N_i(y)F_\tau(x,z)\delta\{u\}_{\tau i} \tag{2.14}$$

Now it is possible to evaluate the fundamental nucleus by virtual variation of internal work:

$$\begin{aligned} \delta W_{int} = \int_V \delta\{\epsilon\}^T\{\sigma\}dV = \int_V \delta\{\epsilon\}^T[C]\{\epsilon\} \\ = \delta\{u_{sj}\}^T \int_V [F_s(x,z)N_j(y)[b]^t[C][b]N_i(y)F_\tau(x,z)]dV\{u_{\tau i}\} \end{aligned} \tag{2.15}$$

The fundamental nucleus is the volume integral between the virtual and not displacement vectors:

$$k^{\tau sij} = \int_V [F_s(x,z)N_j(y)[b]^t[C][b]N_i(y)F_\tau(x,z)]dV \tag{2.16}$$

If all the components of the displacement are considered, the nucleus is a $[3 \times 3]$

matrix. Fixed the indexes τ,s,i and j fundamental nucleus became:

$$\mathbf{k}^{\tau \mathbf{sij}} = \begin{bmatrix} K_{11} & K_{12} & K_{13} \\ K_{21} & K_{22} & K_{23} \\ K_{13} & K_{23} & K_{33} \end{bmatrix} \tag{2.17}$$

"its form does not change for 1D,2D or 3D problems" [9].

2.3 Stiffness matrix assembly procedure

Thanks to the four indexes τ, s, i and j,"the assembly of the stiffness matrix consist of four loop on the indexes and a fundamental nucleus (FN)is calculated for each combination of them" [9]. The Fig 2.2 [9] shows the assembly procedure starting from the structural node until the whole matrix:

- The FN is the core;
- The loop on τ and s build the node matrix;
- The loop on i and j build the element matrix;
- The loop from 1 to N_e (Total number of structural elements) build the stiffness matrix;

In the Fig 2.3 is showed the general for of the stiffness matrix, "the FN work as the core of the matrix construction" [9].

2.3.1 Stiffness matrix evaluation by classical FEM

Now a simple example is proposed, it will be evaluated the stiffness matrix [K] by traditional FEM and by CUF in order to highlight the differences. A ROD element with two nodes is now considered (Fig 2.4), two punctual loads are applied in the

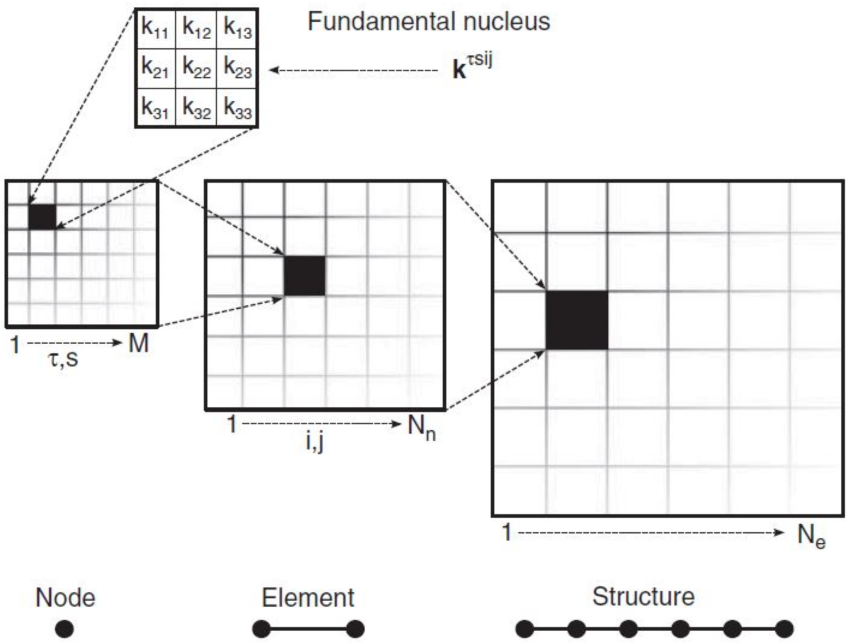

Figure 2.2: Representation of the assembly procedure

$$
\begin{array}{lc|ccc|c|ccc}
 & & \multicolumn{3}{c|}{\overbrace{\tau = 1 \quad \cdots \quad \tau = M}^{i=1}} & & \multicolumn{3}{c}{\overbrace{\tau = 1 \quad \cdots \quad \tau = M}^{i=N_{NE}}} \\
\multirow{3}{*}{$j = 1$} & s = 1 & \boldsymbol{k}^{1111} & \cdots & \boldsymbol{k}^{1M11} & & \boldsymbol{k}^{111N_n} & \cdots & \boldsymbol{k}^{1M1N_n} \\
 & \vdots & \vdots & & \vdots & \cdots & \vdots & & \vdots \\
 & s = M & \boldsymbol{k}^{M111} & \cdots & \boldsymbol{k}^{MM11} & & \boldsymbol{k}^{M11N_n} & \cdots & \boldsymbol{k}^{MM1N_n} \\
 & & & \vdots & & \ddots & & \vdots & \\
\multirow{3}{*}{$j = N_n$} & s = 1 & \boldsymbol{k}^{11N_n1} & \cdots & \boldsymbol{k}^{1MN_n1} & & \boldsymbol{k}^{11N_nN_n} & \cdots & \boldsymbol{k}^{1MN_nN_n} \\
 & \vdots & \vdots & & \vdots & \cdots & \vdots & & \vdots \\
 & s = M & \boldsymbol{k}^{M1N_n1} & \cdots & \boldsymbol{k}^{MMN_n1} & & \boldsymbol{k}^{M1N_nN_n} & \cdots & \boldsymbol{k}^{MMN_nN_n}
\end{array}
$$

Figure 2.3: General stiffness matrix

two nodes $(P_{y1}; P_{y2})$ and linear shape functions are considered $(N_1; N_2)$ (Fig 1.8). The displacement field is the following

$$u_y(y) = N_1(y)u_{y1} + N_2u_{y2} \tag{2.18}$$

Where:

- $N_1 = 1 - \frac{y}{L}$
- $N_2 = \frac{y}{L}$

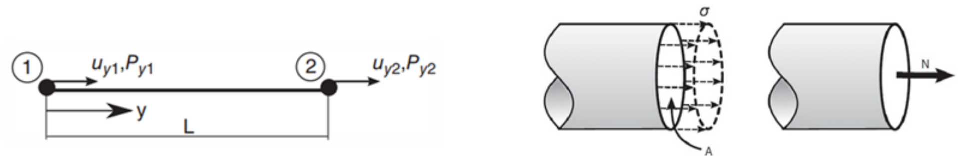

Figure 2.4: ROD element with two nodes (on the left) and relation between force and stress (on the right) [9]

It is possible to evaluate the resultant of normal force "N" on the cross section using the following relation (Fig 2.4):

$$N = \sigma \times A = E \times \epsilon \times A \tag{2.19}$$

Using the geometric relation, the strain trend along the beam axes is the following:

$$\epsilon = \frac{du_y}{dy} = \frac{1}{L}(u_{y2} - u_{y1}) \tag{2.20}$$

While the relation between the normal resultant nodal forces (N) and the applied forces (P) is:

$$\begin{cases} N_1 = -P_{y1} \\ N_2 = P_{y2} \end{cases} \tag{2.21}$$

The normal vector on the node "1" is opposite to the direction of the applied load (Fig 2.4). The final equation system is the following:

$$\begin{cases} P_{y1} = \frac{EA}{L}(u_{y1} - u_{y2}) \\ P_{y2} = \frac{EA}{L}(-u_{y1} + u_{y2}) \end{cases} \tag{2.22}$$

That in matrix form became:

$$\frac{EA}{L}\begin{bmatrix} 1 & -1 \\ -1 & 1 \end{bmatrix}\begin{pmatrix} u_{y1} \\ u_{y2} \end{pmatrix} = \begin{pmatrix} P_{y1} \\ P_{y2} \end{pmatrix} \tag{2.23}$$

So, the stiffness matrix is:

$$[K] = \frac{EA}{L}\begin{bmatrix} 1 & -1 \\ -1 & 1 \end{bmatrix} \tag{2.24}$$

2.3.2 Stiffness matrix evaluation by CUF

For the same problem showed in Fig 2.4, the stiffness matrix is now evaluated by CUF. Displacements, strains and their virtual variation can be write in the following manner:

$$\begin{cases} u_y(y) = N_i(y)u_{yi} \\ \delta u_y(y) = N_j(y)u_{yj} \\ \epsilon = N_{i,y}u_{yi} \\ \delta\epsilon = N_{j,y}\delta_{yj} \end{cases} \tag{2.25}$$

Where: $N_{i,y} = \frac{dN_i}{dy}$.

Now it is possible rewrite the virtual variation of internal work, in order to obtain the fundamental nucleus.

$$\begin{aligned} \delta W_{int} = \int_V \{\delta\epsilon\}^T\{\sigma\}dV &= \int_V \{\delta\epsilon\}^T E\{\epsilon\}dV \\ &= \delta u_{yi}\Big(\int_V B_{i,y}EN_{i,y}dV\Big)u_{yi} \\ &= \delta u_{yi}k^{ij}u_{yi} \end{aligned} \tag{2.26}$$

k^{ij} is the fundamental nucleus of the bar:

$$k^{ij} = \int_V N_{j,y} E N_{i,y} dV \tag{2.27}$$

It is invariant respect to the number of elements nodes and the choice oh the shape function (N). The explicit form of the nucleus is the following:

$$\begin{aligned}
k^{11} &= \int_V N_{1,y} E N_{1,y} dV = \frac{1}{L} E \frac{1}{L} AL = \frac{EA}{L} \\
k^{12} &= \int_V N_{2,y} E N_{1,y} dV = -\frac{1}{L} E \frac{1}{L} AL = -\frac{EA}{L} \\
k^{21} &= \int_V N_{1,y} E N_{2,y} dV = -\frac{1}{L} E \frac{1}{L} AL = -\frac{EA}{L} \\
k^{22} &= \int_V N_{2,y} E N_{2,y} dV = \frac{1}{L} E \frac{1}{L} AL = \frac{EA}{L}
\end{aligned} \tag{2.28}$$

Thus the stiffness matrix is:

$$\mathbf{k} = \begin{bmatrix} K_{11} & K_{12} \\ K_{21} & K_{22} \end{bmatrix} = \frac{EA}{L} \begin{bmatrix} 1 & -1 \\ -1 & 1 \end{bmatrix} \tag{2.29}$$

Obviously the stiffness matrix is identical to the previous one.

2.4 The Taylor expansion class (TE)

The Taylor Expansion class (TE) is based on Taylor-like polynomial expansions to describe the cross-section behaviour, the 1D model has 2D functions ($F_\tau(x,z)$ and $F_s(x,z)$) in the variables x and z. The order of expansion (N) could be arbitrary but a convergence study of solution generally is necessary, tab. 2.1 shows the Taylor-like polynomial terms and the total number of variable (M) as the order of expansion increases. In according to the Einstein notation and Carrera unified formulation, the displacement field on the cross-section can be write as:

$$u = F_\tau u_\tau \tag{2.30}$$

For example if N=2, the displacement field decomposed in the three direction is:

$$\begin{cases} u_x = u_{x1} + xu_{x2} + zu_{x3} + x^2u_{x4} + xzu_{x5} + z^2u_{x6} \\ u_y = u_{y1} + xu_{y2} + zu_{y3} + x^2u_{y4} + xzu_{y5} + z^2u_{y6} \\ u_z = u_{z1} + xu_{z2} + zu_{z3} + x^2u_{z4} + xzu_{z5} + z^2u_{z6} \end{cases} \tag{2.31}$$

This model (N=2) has 18 displacement variables:

- 3 constant terms;
- 6 linear terms;
- 9 parabolic terms;

Classical beam theories as Euler-Bernoulli and Timoshenko are particular cases of the model with unitary order."Nevertheless the use of Taylor-type expansions has some intrinsic limitations that led to the introduction of different polynomial classes" [10]. In particular, Taylor-like polynomials on the cross-section entail that:

- The introduced variables have a mathematical meaning (derivatives at the beam axes) [10];
- Higher order terms cannot have a local meaning, they can have cross-section properties only [10];
- The extension to large rotation formulation could experience difficulties [10];

Table 2.1: Taylor-like expansion [9]

N	M	F_τ
0	1	$F_1 = 1$
1	3	$F_2 = x,\ F_3 = z$
2	6	$F_4 = x^2,\ F_5 = xz,\ F_6 = z^2$
3	10	$F_7 = x^3,\ F_8 = x^2z,\ F_9 = xz^2,\ F_{10} = z^3$
$\vdots$	$\vdots$	$\vdots$
N	$(N+1)(N+2)/2$	$F_{(N^2+N+2)/2} = x^N,\ \dots,\ F_{(N+1)(N+2)/2} = z^N$

2.5 Lagrange expansion class (LE)

In this chapter another expansion class based on Lagrange polynomials is explained. The finite elements model is based, as in previous subsection, on 1D Carrera unified formulation, so the $F_\tau(x,z)$ and $F_s(x,z)$ function are now the Lagrange polynomials and the unknown variable u_τ are the nodal displacement. The use of Lagrange expansion to describe the cross-section behaviour has many advantages, the main ones are the following:

- LE model variables and boundary conditions can be located above the physical surfaces of the structure as shows the Fig 2.5 [9];
- The problem unknown variables are the pure displacement components;
- It is possible to refine locally the cross-section in order to catch local effects, so the computational cost are reduced;

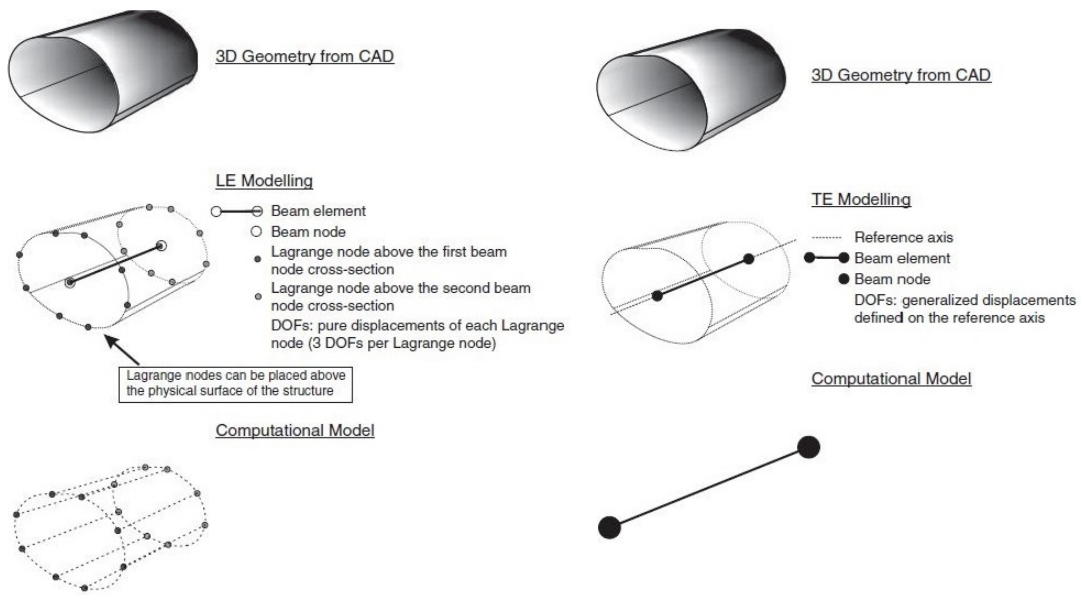

Figure 2.5: Comparison between LE and TE class

The Lagrange polynomials are usually given in terms of normalized coordinates "α" and "β". It is convenient because in the normalized plane any complex element is reduced to a square or a triangle, so it becomes easy to calculate elements area. The Fig 2.6 [9] shows three different type of Lagrange elements in the physical plane (x,y) and in the normalized plane (α,β), they are:

- Three nodes Lagrange elements called L3, the first one in the Fig 2.6;
- Six nodes Lagrange elements called L6, the second one in the Fig 2.6;
- Nine nodes Lagrange elements called L9, the last one in the 2.6;

For reasons related to the algorithms stability, L9 is the type element will be used for the static and failures analysis.

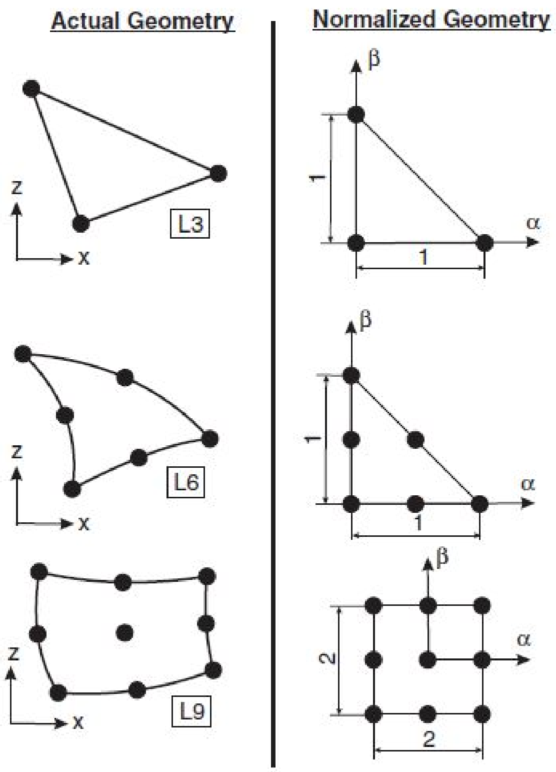

Figure 2.6: L3, L6 and L9 elements in physical (x,y) and normalized (α, β) plane

2.5.1 L9 elements

The Fig 2.7 [9] shows an L9 element in both the planes, physical and normalized. This type of element is composed by nine nodes, the middle node is necessary for the evaluation of the local normal vector which in turn is necessary for the Gauss integration. The numeration of the nodes, called element connectivity, is not random but starts from an edge point and finish to the middle point following an anticlockwise sense.

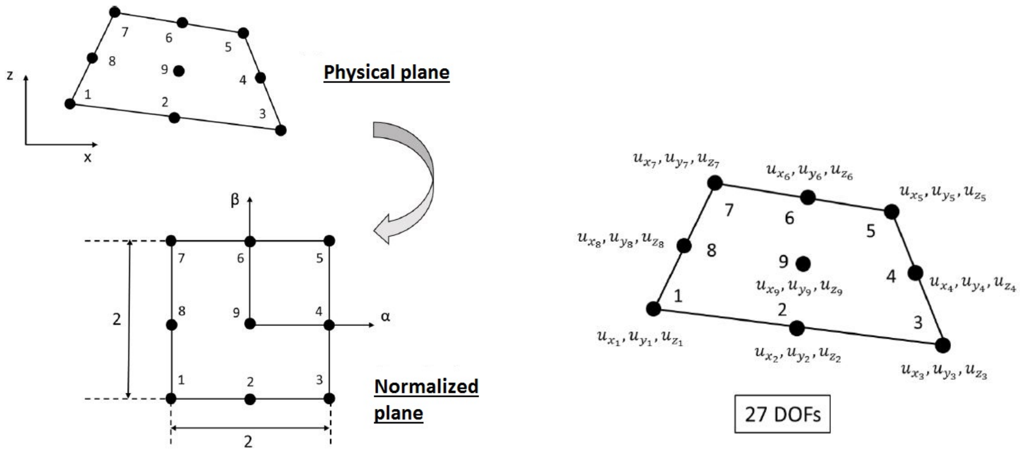

Figure 2.7: L9 type element in physical (x,y) and normalized (α, β) plane (left) and L9 DOFs (right)

The Lagrange polynomials are given in terms of normalized coordinates α and β, so the generic L9 element became a square with long sides equal to two. The nodes coordinates, in normalized plane, are summarized in the tab. 2.2 and the Lagrange polynomials F_τ are the following:

$$\begin{cases} F_\tau = \dfrac{1}{4}\left(\alpha^2 + \alpha\alpha_\tau\right)\left(\beta^2 + \beta\beta_\tau\right), \quad \tau = 1,\, 3,\, 5,\, 7 \\ F_\tau = \dfrac{1}{2}\alpha_\tau^2\left(\alpha^2 + \alpha\alpha_\tau\right)\left(1 - \beta^2\right) + \dfrac{1}{2}\beta_\tau^2\left(\beta^2 + \beta\beta_\tau\right)\left(1 - \alpha^2\right), \quad \tau = 2,\, 4,\, 6,\, 8 \\ F_\tau = \left(1 - \alpha^2\right)\left(1 - \beta^2\right), \quad \tau = 9 \end{cases} \tag{2.32}$$

Table 2.2: Normalized coordinates of L9 type element

Point	α_τ	β_τ
1	-1	-1
2	0	-1
3	1	-1
4	1	0
5	1	1
6	0	1
7	-1	1
8	-1	0
9	0	0

"L9 elements can be seen as a parabolic expansion plus two cubic terms ($\alpha\beta^2$ and $\alpha^2\beta$) and a quadratic term ($\alpha^2\beta^2$)" [9].
The displacements field is:

$$\begin{cases} u_x = F_1 u_{x_1} + F_2 u_{x_2} + \dots + F_9 u_{x_9} \\ u_y = F_1 u_{y_1} + F_2 u_{y_2} + \dots + F_9 u_{y_9} \\ u_z = F_1 u_{z_1} + F_2 u_{z_2} + \dots + F_9 u_{z_9} \end{cases} \tag{2.33}$$

Where "$u_{x_1} \dots u_{z_9}$" are the problem displacements variables and they stand for pure displacement component of each of the nine L9 elements nodes, it is not difficult now to calculate the problem degrees of freedom (DOFs) because it is given by the number of the displacements variables. The Fig 2.7 [9]shows the DOFs related to one L9 element, it has 3 displace components (u_x, u_y, u_z) for each node so the DOFs number is equal to 27. In conclusion, "LE model provide elements that have only pure displacement variables" [10]. The cross-section can be discretized trough L9 elements and they can be assembled by the common nodes (Fig 2.8), this cross-section assembly process is independent by the choice of the type and the number of beam elements.

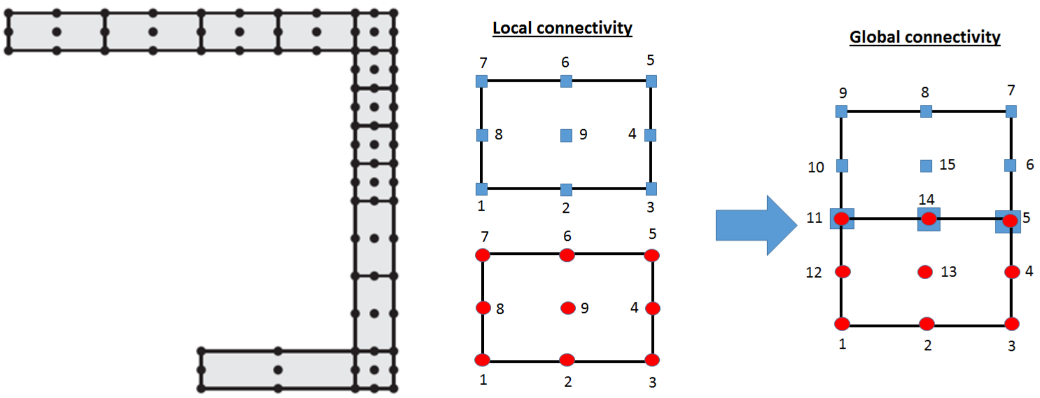

Figure 2.8: Cross-section discetization example (left) and L9 elements assembly process (right)

The Lagrange expansion class has an important feature, previously mentioned, related to the possibility to refine locally the cross-section, it is possible because the stiffness matrix is assembled in a different way compared to Taylor expansion (TE). The Fig 2.9 [10] shows a part of stiffness matrix assembly process referred to multi-component structure composed by two layers: the first one is a homogeneous layer while the second one is composed by matrix and fiber. This is only the assembly process part of the cross-section elements, in order to arrive at the global stiffness matrix [k], the assembly procedure along the beam elements must be added. The matrix is assembled for both TE and LE approaches, in the first one (TE) a sort of properties homogenization is operate because the number of the unknown variable is fixed by the model order adopted while in the second one (LE) the number of the unknowns variable is related to the total number of the cross-section node, thus homogenization does not occur. For these reasons with LE models is possible refine only a part of the cross-section to catch local effects, as shown in the Fig 2.10 [9], without having to refine the whole cross-section with a significant computational savings.

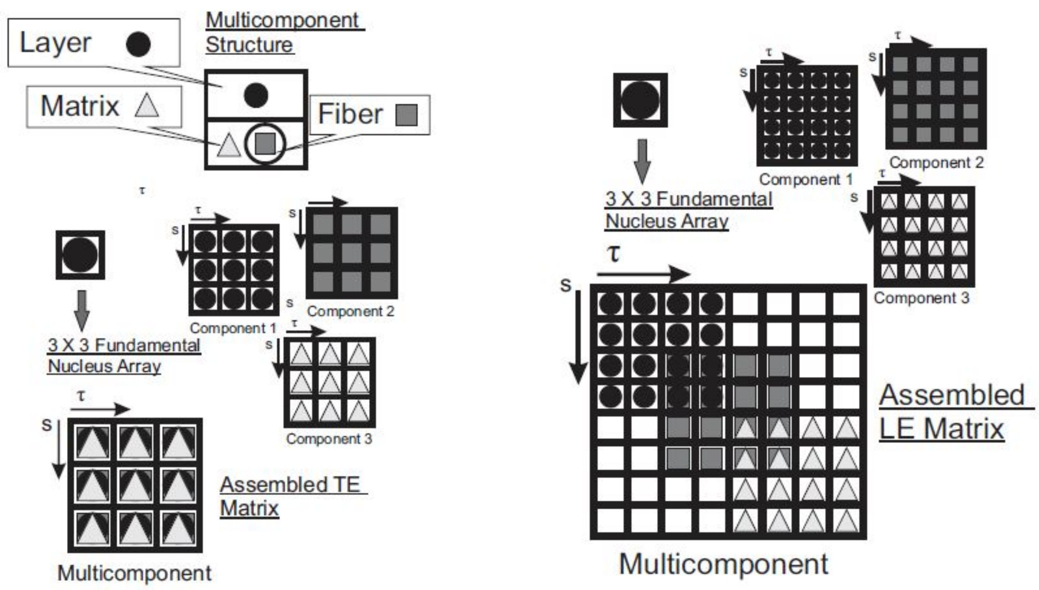

Figure 2.9: TE (left) and LE (right) assembly technique for a multi-component structure

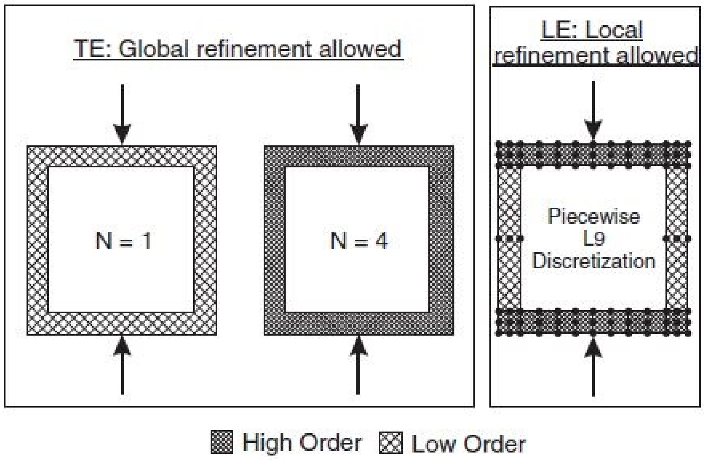

Figure 2.10: Global vs local refinements on the cross-section

2.6 Sparse matrix and computational cost analysis

Progressive failure analysis, will be described in the micromechanical chapter, consist in solving hundreds of times a the linear system 2.34, and if the process is not optimized the computational cost became unacceptable. For the progressive failure analysis only the LE class are used to describe the cross-section behaviour and in this case the stiffness matrix [k] contains a lot of null element. When a matrix has a lot of zero elements it is called sparse matrix and specific algorithms exist to solve linear system equation with them, for istance the "PARDISO" library implemented by Intel. Below a simple examples that shows the null elements in the stiffness matrix is proposed.

$$[k]\{U\} = \{F\} \tag{2.34}$$

2.6.1 Example

In this example are showed the zero elements of the stiffness matrix [k] for a cell composed by 6 beam element with two nodes and 2 cross-section elements with four point (Fig. 2.11). The value of the indexes "s" and "τ" varies from 1 to 6 because six is the total number of section nodes while the indexes "i" and "j" varies from 1 to 2 because two is the number of the beam nodes. The Fig. 2.12 shows, starting from the fundamental nucleus [3 $times$3], the nodal contribution to stiffness matrix [18 $\times$ 18], the circles are referred to the first cross-section element while the square to the second and the white space are the null elements. The next step is the beam element contribution, it is shown in the Fig. 2.13 and it is possible to understand that it is composed by four nodal contribution forming a matrix [36 $\times$ 36]. Lastly is the global stiffness matrix shown in Fig 2.14 , it is a NDOFs $\times$ NDOFs matrix i.e. [126 $\times$ 126] and it is composed by six element matrix with the corners overlapped due to the joint node. In the last figure all the blue space represent the zero elements, so it is possible to affirm that the stiffness matrix with LE class is a sparse matrix.

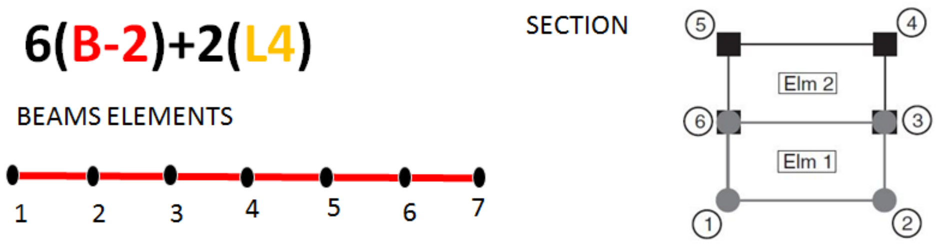

Figure 2.11: 2(B-2)+1(L3)

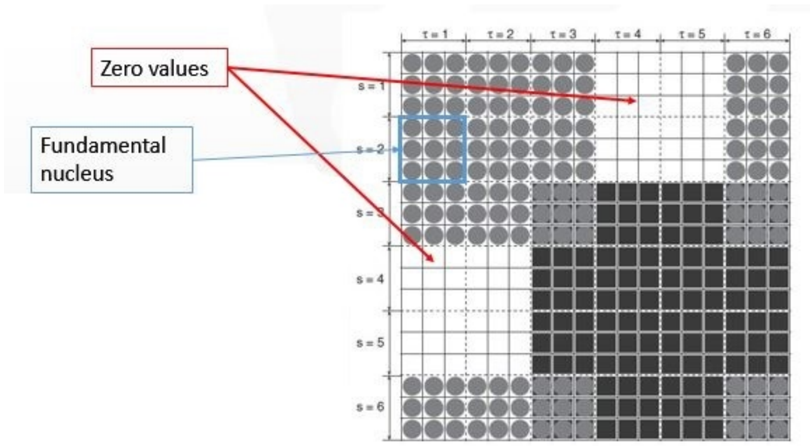

Figure 2.12: Node contribution to stiffness matrix

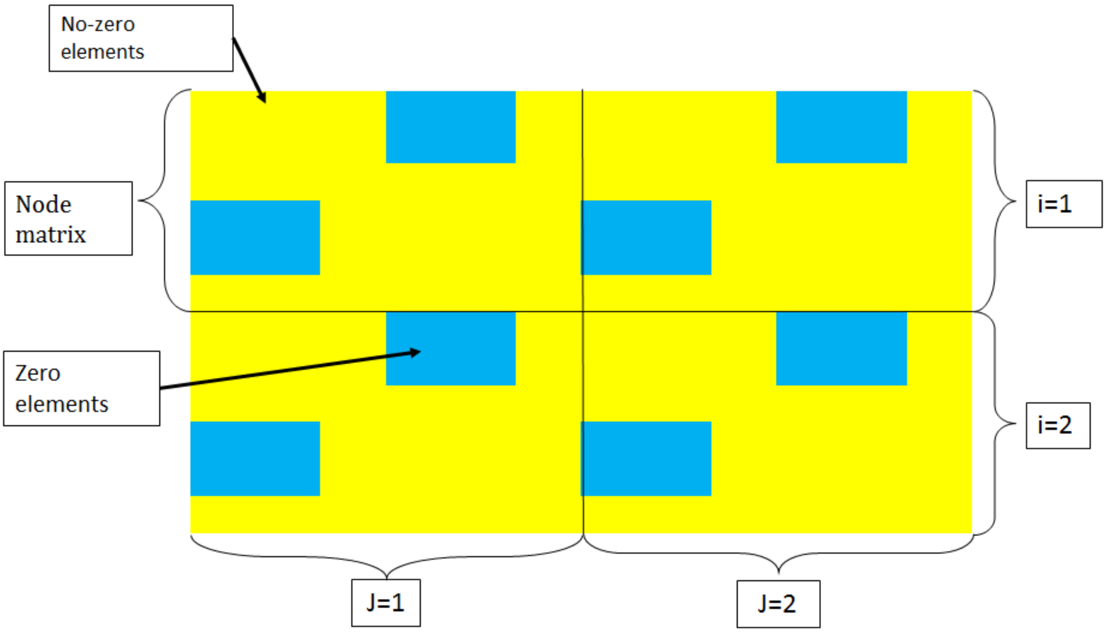

Figure 2.13: Beam element contribution to stiffness matrix

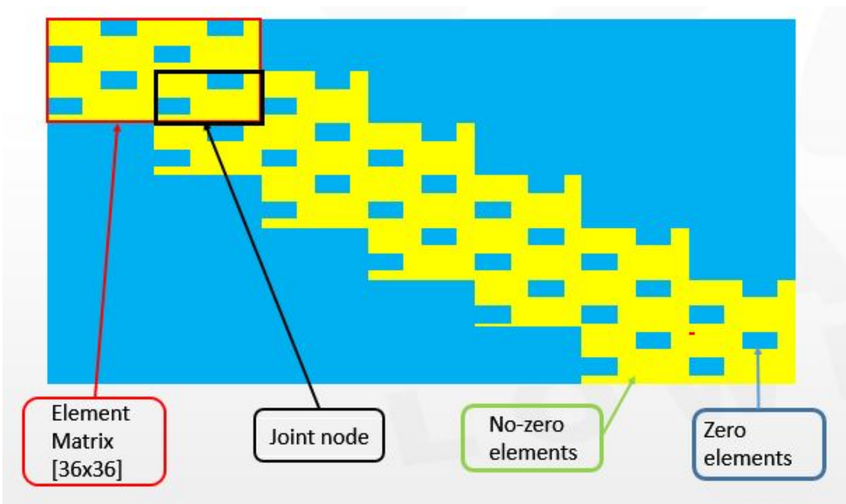

Figure 2.14: Zero elements in global stiffness matrix

2.7 Pardiso library

PARDISO is a Intel MKL Library [11] [12], it is high-performance software for solving large sparse symmetric and nonsymmetric linear system of equations. The Fig. 2.15 shows all the type of sparse matrix that can be solve the software, but in this thesis work we are interested only to real symmetric and real un-symmetric matrix. The software solve the liner system equation as $[A]\{x\} = \{b\}$ and it want in input the two vector x and b and the matrix rewrite in the CRS form.

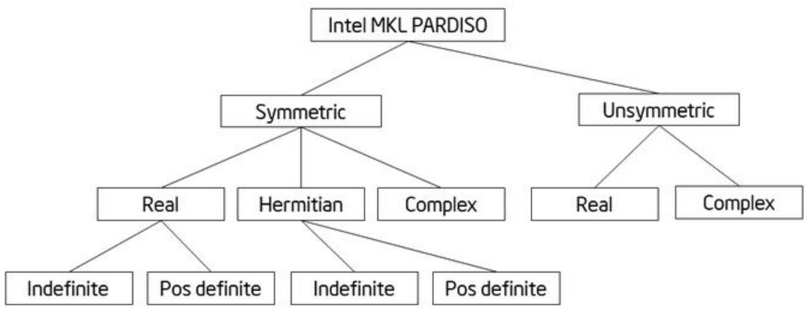

Figure 2.15: Sparse matrices that can be solved by PARDISO

2.7.1 Compress row storage (CRS) implementation

The software is based on the "compress row storage" (CRS), it is a particular storage method where the matrix is rewritten as 3 vectors. As shows the Fig. 2.16 the sparse matrix is transformed in 3 vectors:

- Vector $\{A\}$ contains all the no-zero elements;
- Vector $\{JA\}$ contains the columns indexes of no-zero elements and it is the same length of the vector A;
- Vector $\{IA\}$ contains the indexes elements, referred to vector A, that start a new raw in the matrix;

NOTE: The length of IA vector is equal to "n+1" (n is the number of the matrix rows/column) because the last element is always equal to the no-zero elements number plus one.
In case of symmetric matrix, it is stored only the upper (lower) triangular portion of matrix Fig. (2.16). It is important to note that the matrix is read starting from the first element and scanning all the rows (from left to right). The code is based on Fortran language, so the Fig. 2.18 and 2.17 shows the CRS implementation in this programming language. The CRS implementation for un-symmetric matrix is composed by two nested do-cycle: the fist one count the number of no-zero elements so it is possible to allocate the dimension to JA and A vectors, the second one fills the three vectors as showed before. Instead the CRS implementation for symmetric matrix is a little bit different because only upper triangular portion must be stored. The first do-cycle count the number of no-zero elements of the upper triangular portion except the diagonal, indeed at the end of the cycle, the length of the two vectors JA and A is equal to the no-zero elements number plus the number of system equations. The second do-cycle, like the previous, fill the three vectors, it is more complex because it did non read all the matrix but only the upper triangular side.

2.7.2 PARDISO subroutine

The implementation of PARDISO library [11] [12] in the code, in order to reduce of the computational cost of the failure analysis, it is made introducing a new subroutine in the code for the linear system equations resolution. The input parameters of the subroutine are:

- N DOF TOT = total number of degree of freedom problem;
- K struct = stiffness matrix of problem;
- FORCES = forces vector applied on the structural nodes;

	1	2	3	4	5	6	7	8
1	7.		1.			2.	7.	
2		–4.	8.		2.			
3			1.					5.
4				7.			9.	
5		–4.						
6			7.			3.		5.
7		17.					11.	
8			–3.				2.	5.

	1	2	3	4	5	6	7	8
1	7.		1.			2.	7.	
2		–4.	8.		2.			
3			1.					5.
4				7.			9.	
5					5.	–1.	5.	
6						0.		5.
7							11.	
8								5.

K	Nonsymmetric Matrix			Symmetric Matrix		
	IA(K)	JA(K)	A(K)	IA(k)	JA(K)	A(K)
1	1	1	7.	1	1	7.
2	5	3	1.	5	3	1.
3	8	6	2.	8	6	2.
4	10	7	7.	10	7	7.
5	12	2	-4.	12	2	-4.
6	13	3	8.	15	3	8.
7	16	5	2.	17	5	2.
8	18	3	1.	18	3	1.
9	21	8	5.	19	8	5.
10		4	7.		4	7.
11		7	9.		7	9.
12		2	-4.		5	5.
13		3	7.		6	-1.
14		6	3.		7	5.
15		8	5.		6	0.
16		2	17.		8	5.
17		7	11.		7	11.
18		3	-3.		8	5.
19		7	2.			
20		8	5.			

Figure 2.16: CRS for symmetric and un-symmetric matrices

```
!counts the number of no-zero elements
nnz=0 !variable initialization
do i=1,N_DOF_TOT
    do j=1,N_DOF_TOT
        if(K_struct(i,j) .ne. 0 ) then
            nnz=nnz+1
        end if
    end do
end do
ALLOCATE(ja(nnz))
ALLOCATE(a(nnz))
!procedure to fill the vectors "a,ja,ia"
c=0 !variable initialization
ia(1)=1  !first "ia" vector element is always one

do i=1,N_DOF_TOT
    do j=1,N_DOF_TOT
        if(K_struct(i,j) .ne. 0 ) then
                c=c+1
                a(c)=K_struct(i,j)
                ja(c)=j
        end if
    end do
        ia(i+1)=c+1
end do
```

Figure 2.17: CRS implementation for symmetric matrix

- UNKNOWNS = is the unknowns vector;

They are declared in brackets after the subroutine name and they are essential for the operation of the subroutine. The subroutine output instead is the unknowns

```
!counts the number of no-zero elements locate over the diagonal (i>j)
nnz=0 !variable initialization
do i=1,N_DOF_TOT
    do j=1,N_DOF_TOT
       if (i .lt. j) Then
              if(K_struct(i,j) .ne. 0 ) then
                  nnz=nnz+1
              end if
       end if
    end do
 end do
ALLOCATE(ja(nnz+N_DOF_TOT))
ALLOCATE(a(nnz+N_DOF_TOT))

!procedure to fill the vectors "a,ja,ia"
c=0 !variable initialization
ia(1)=1 !first "ia" vector element is always one
do i=1,N_DOF_TOT
    do j=1,N_DOF_TOT
        if (i .eq. j) then
             c=c+1
             a(c)=K_struct(i,j)
             ja(c)=j
        elseif (i .lt. j) then
                          if(K_struct(i,j) .ne. 0 ) then
                               c=c+1
                               a(c)=K_struct(i,j)
                               ja(c)=j
                     end if
        end if
    end do
        ia(i+1)=c+1
end do
```

Figure 2.18: CRS implementation for un-symmetric matrix

vector, it is empty initially and at the end of the algorithm it is filled with the solution of the linear system equations. Before the declaration of all the subroutine variables, it is necessary to include the library by the command "include" and the name of the library is "mkl pardiso.f77". Furthermore the "implicit none" statement is used, it has the task of inhibit a old feature of Fortran that assign the integer type at all the variables that start with the letters i, j, k, l, m and n and also it makes the detection of the errors easier. In the subroutine there are two type of arrays: dynamic and static, the static arrays have the dimension assigned while the dynamic are declares as "allocatable" and the dimension may be allocated in a later stage. For instance, the size of the vector "a" (the vector containing all the no-zero variables) is allocated after the first do-cycle of the CRS implementation. After the declaration of all the variables (Fig. 2.19), the stiffness matrix (K struct) is decomposed in three vectors by the CRS implementation described in the previous section so the inputs for the PARDISO library are ready. Before to solve the liner system equations, there are some library parameters to be set, in the Fig. 2.20 are shown all the setting parameter using for the analysis, the main ones are:

- iparm(1)= if the value of this parameter is "0" the library work with default setting, otherwise if it is equal to "1" the library does not work in default setting;
- iparm(64)= if the linear system equations is very large, it is convenient to set this parameter equal to two;
- mtype = this parameter set the solution method through the matrix type, for instance "11" stay for un-symmetric matrix;
- iparm(3)= this parameter indicates the number of the processor that the program can be use, it is important because a good setting of it can reduce the computational time;

NOTE: For the sense of all the other parameter the guide can be consulted. Now is possible to call the solve by the command "call", it solve the linear system in three phases:

- Phase 1=Fill-reduction analysis and symbolic factorization;
- Phase 2=Numerical factorization;
- Phase 3=System resolution;

After that the unknowns vector is ready to be processed in other code subroutine, actually there are another phase called "phase zero" that clears all the memory used during the previous phases.

```
********************************************************************************
C-----------------------------------------------------------------------
C Example program to show the use of the "PARDISO" routine
C for symmetric linear systems
C-----------------------------------------------------------------------
      subroutine PARADISO(N_DOF_TOT, K_struct, FORCES,
     &                         UNKNOWNS)
        IMPLICIT NONE
        include 'mkl_pardiso.f77'
C.. Internal solver memory pointer for 64-bit architectures
C.. INTEGER*8 pt(64)
C.. Internal solver memory pointer for 32-bit architectures
C.. INTEGER*4 pt(64)
C.. This is OK in both cases
        INTEGER*8 pt(64)
C.. All other variables
        INTEGER maxfct, mnum, mtype, phase, N_DOF_TOT, nrhs, error
        INTEGER msglvl,nnz,j,c
        INTEGER iparm(64)
        INTEGER ia(N_DOF_TOT+1)
        INTEGER, ALLOCATABLE :: ja( : )
        REAL*8, ALLOCATABLE :: a(:)
        REAL*8 K_struct(N_DOF_TOT,N_DOF_TOT)
        REAL*8 FORCES(N_DOF_TOT)
        REAL*8 UNKNOWNS(N_DOF_TOT)
        INTEGER i, idum(1)
        REAL*8  ddum(1)
```

Figure 2.19: Variable declaration in the subroutine

```
iparm(1) = 1 ! no solver default iparm(1)=1
iparm(2) = 2 ! fill-in reducing ordering for the input matrix...iparm(2)=0 use the minimum degree alhotith
iparm(3) =1 ! numbers of processors
iparm(4) = 0 ! no iterative-direct algorithm
iparm(5) = 0 ! no user fill-in reducing permutation
iparm(6) = 0 ! =0 the array x containes the solution
iparm(7) = 0 ! not in use
iparm(8) = 9 ! numbers of iterative refinement steps
iparm(9) = 0 ! not in use
iparm(10) = 13 ! perturb the pivot elements with 1E-13...it is the default value for non simmetric matrix
iparm(11) = 1 ! use nonsymmetric permutation and scaling MPS...default value for non simmetric matrix
iparm(12) = 0 ! Solve a linear sysyem AX=B
iparm(13) = 1 ! maximum weighted matching algorithm is switched-on (default for non-symmetric)
iparm(14) = 0 ! Output: number of perturbed pivots...if you want to see this number msglvl=1
iparm(15) = 0 ! Output: Peak memory on symbolic factorization...//
iparm(16) = 0 ! Output: Permament memory on symbolic factorization...//
iparm(17) = 0 ! Output: Peak memory on numerical factorization and solution...//
iparm(18) = -1 ! Output: number of nonzeros in the factor LU...//
iparm(19) = -1 ! Output: Mflops for LU factorization
iparm(20) = 0 ! Outpur:Diagnostic report about factorizzation
iparm(64)=2 !For large problems
error = 0 ! initialization of error flag
msglvl = 0 ! print statistical information if msglv=1
mtype = 11 ! Type of matrix...11=real unsymmetric matrix
nrhs = 1 !Number of right-hand sides that need to be solved for...Generally used value is 1
maxfct = 1 !Maximal number of factors in memory...Generally used value is 1
mnum = 1 !The number of matrix (from 1 to maxfct) to solve...Generally used value is 1
```

Figure 2.20: PARDISO library setup

Chapter 3

Static analysis by CUF: assessment of referred structures

In this chapter it will be analyzed a referred structures with different theoretical model using CUF. In all cases which will be reported, the reference system will be the same and it is shown in the figure below (Fig. 3.1).The longitudinal axis of the beam coincides with the coordinate y ($0 \leq y \leq L$) and the cross-section is overlayed on the x-z plane.

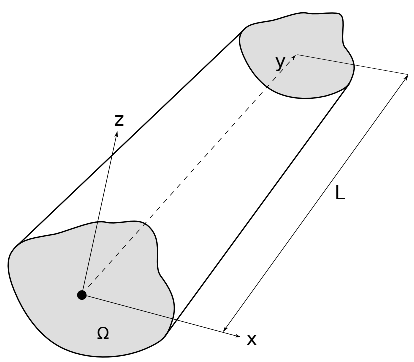

Figure 3.1: Reference system

3.1 Analysis via Euler-Bernoulli beam model

Euler-Bernoulli beam model is obtained as a particular case of the general Nth-order model. Using this theory, the shear deformation γ_{xy} and γ_{yz} are not contemplated. The purpose of analysis is the evaluation of the vertical displacement of the free tip via Euler-Bernoulli model.

3.1.1 Description of the problem

Let's consider a cantilever, rectangular cross-section beam under the action of a punctual load P_z.The load is applied at the center point section of the free tip and it is worth P_z=-10 N. They will be analyzed two similar beam with different length: L=1m and L=10m. The displacement will be evaluated at the center of the section of the beam free tip. The geometrical and material proprieties are listed in table 3.1.

Table 3.1: Geometric and material properties of beam

Parameters	Values	Units
Geometrical Properties		
Beam Length (L)	1.0/10.0	m
Slenderness (L/h)	10/100	-
Cross-section width (w)	2.0	cm
Cross-section height (h)	10.0	cm
Material Properties		
Young's modulus	75.0	GPa
Poisson's Ratio	0.33	-

3.1.2 Results

The analysis results, obtained using five beam elements B2, are summarized in the table 3.2, furthermore these have been compared with the result obtained via analytical theory of Euler-Bernoulli. Below there are the displacement fields representation of two cases taken into account during the analysis (Fig. 3.2 and 3.3). The difference between analytical theory of Euler-Bernoulli and the FEM result are indicated with the "Percentage error" value in table 3.2, they are evaluated with the following equation:

$$\textbf{Error}(\%) = \frac{(ANALYTICAL\,result) - (FEM\,result)}{(ANALYTICAL\,result)} \tag{3.1}$$

Table 3.2: Results with Euler-Bernoulli model

Cases	u_z at free-end [m]	DOF	Percentage error
Beam (L=1m)	$-2.640 * 10^{-4}$	18	0.801
Beam (L=10m)	$-2.640 * 10^{-2}$	18	0.802

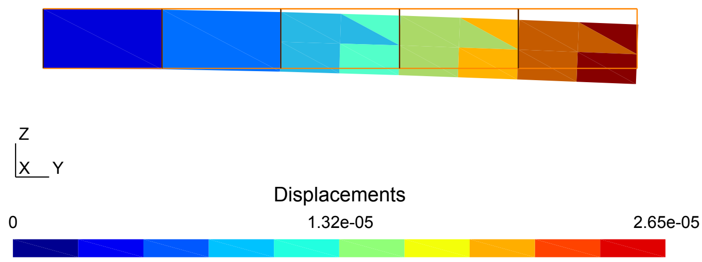

Figure 3.2: Deformed configuration of beam with L=1m

3.2 Analysis via Taylor-like expansion

The reason of the analysis is the evaluation of a beam's point displacement and the maximum value of stress σ_{yy} under the action of a punctual load P_z.These solutions will be obtained via Finite Elements Method varying the type of elements,the number of elements and lastly the order of the Taylor-like expansions.

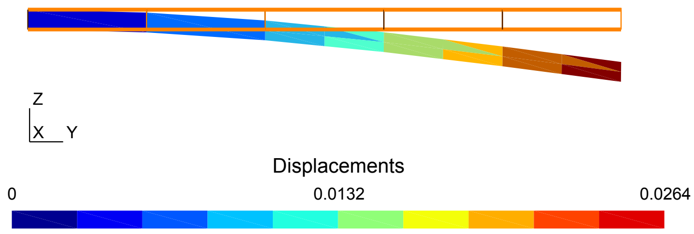

Figure 3.3: Deformed configuration of beam with L=10m

3.2.1 Description of problem

For the following analysis has been used the same cantilever, rectangular cross-section beam employed in the previously one with the same load applied at the free tip. During these analysis it will be analyzed also the stress σ_{yy} in two different points of the section were their value is the maximum one and opposite sign. The coordinates of these points are in centimetres: (0,0,5);(0,0,-5).

3.2.2 Results

For the analysis it was used only the B4 beam element.

The first analysis based on the two beams (L=1m;L=10m) has been performed using twenty elements B4 and varying the order of model (N) until the difference between the results of two consecutive analysis has reached a negligible value. In addition the results can be compared with the values obtained via and the Navier equations. The analysis results are summarized in the table 3.3.

The second analysis, based on the same beams, has been performed using N=4 and varying the number of elements until the difference between the results of two consecutive analysis has reached a negligible value.In addition the results can be compared with the values obtained via the Navier equations. The analysis results are summarized in the table 3.4.

Table 3.3: Result obtained with 20 elements B4

Order model	σ_{yy} top [Pa]	σ_{yy} bottom [Pa]	u_z at free-end [m]	DOF
L=1m				
Navier	$2.994 * 10^5$	$-2.994 * 10^5$	-	-
Euler-Bernoulli	$3.000 * 10^5$	$-3.000 * 10^5$	$-2.667 * 10^{-5}$	183
Timoshenko	$3.000 * 10^5$	$-3.000 * 10^5$	$-2.684 * 10^{-5}$	305
N=1	$3.000 * 10^5$	$-3.000 * 10^5$	$-2.684 * 10^{-5}$	549
N=2	$3.352 * 10^5$	$-3.352 * 10^5$	$-2.670 * 10^{-5}$	1098
N=3	$3.678 * 10^5$	$-3.678 * 10^5$	$-2.673 * 10^{-5}$	1830
N=4	$3.726 * 10^5$	$-3.726 * 10^5$	$-2.674 * 10^{-5}$	2745
N=5	$4.078 * 10^5$	$-4.078 * 10^5$	$-2.675 * 10^{-5}$	3843
N=6	$4.121 * 10^5$	$-4.121 * 10^5$	$-2.675 * 10^{-5}$	5124
N=7	$4.224 * 10^5$	$-4.224 * 10^5$	$-2.675 * 10^{-5}$	6588
N=8	$4.234 * 10^5$	$-4.234 * 10^5$	$-2.675 * 10^{-5}$	8235
N=9	$4.288 * 10^5$	$-4.288 * 10^5$	$-2.675 * 10^{-5}$	10065
N=10	$4.290 * 10^5$	$-4.290 * 10^5$	$-2.675 * 10^{-5}$	12078
L=10m				
Navier	$2.994 * 10^6$	$-2.994 * 10^6$	-	-
Euler-Bernoulli	$3.000 * 10^6$	$-3.000 * 10^6$	$-2.667 * 10^{-2}$	305
Timoshenko	$3.000 * 10^6$	$-3.000 * 10^6$	$-2.667 * 10^{-2}$	549
N=1	$3.000 * 10^6$	$-3.000 * 10^6$	$-2.667 * 10^{-2}$	1098
N=2	$3.468 * 10^6$	$-3.468 * 10^6$	$-2.657 * 10^{-2}$	1830
N=3	$3.502 * 10^6$	$-3.502 * 10^6$	$-2.657 * 10^{-2}$	2745
N=4	$3.503 * 10^6$	$-3.503 * 10^6$	$-2.657 * 10^{-2}$	3843
N=5	$3.505 * 10^6$	$-3.505 * 10^6$	$-2.657 * 10^{-2}$	5124
N=6	$3.505 * 10^6$	$-3.505 * 10^6$	$-2.657 * 10^{-2}$	6588

Table 3.4: Result obtained with elements B4 and N=4

N° elements	σ_{yy} top [Pa]	σ_{yy} bottom [Pa]	u_z at free-end [m]	DOF
L=1m				
5-B4	$3.634 * 10^5$	$-3.634 * 10^5$	$-2.649 * 10^{-5}$	720
10-B4	$3.737 * 10^5$	$-3.737 * 10^5$	$-2.667 * 10^{-5}$	1395
20-B4	$3.726 * 10^5$	$-3.726 * 10^5$	$-2.674 * 10^{-5}$	2745
40-B4	$3.499 * 10^5$	$-3.499 * 10^5$	$-2.677 * 10^{-5}$	5445
60-B4	$3.322 * 10^5$	$-3.322 * 10^5$	$-2.678 * 10^{-5}$	8145
L=10m				
5-B4	$3.474 * 10^6$	$-3.474 * 10^6$	$-2.629 * 10^{-2}$	720
10-B4	$3.481 * 10^6$	$-3.481 * 10^6$	$-2.648 * 10^{-2}$	1395
20-B4	$3.503 * 10^6$	$-3.503 * 10^6$	$-2.657 * 10^{-2}$	2745
40-B4	$3.554 * 10^6$	$-3.554 * 10^6$	$-2.662 * 10^{-2}$	5445

3.3 Evaluation of the σ_{yy} stress trend

In this chapter it will be evaluated the trend of σ_{yy} stress long the z axis on a generical section of beam. The stresses will be evaluated using Taylor-like expansion for the nodes of the mesh.

3.3.1 Description of problem

Let's consider the same beam of the previous chapters. The load applied at the free tip create a bending moment, which in turn, create a σ_{yy} stress on the faces of beam. Since the trend of σ_{yy} stress is the same for all the section of the beam, it is evaluated on the points that have x and y coordinate null while the z coordinate vary from -5cm to 5cm with a step of 1.25 cm (fig. 3.4) .

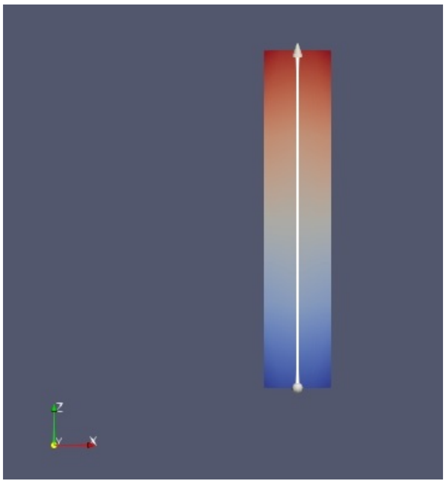

Figure 3.4: Points where is evaluated the trend of σ_{yy} stress

3.3.2 Results

For the evaluation of trend, twenty B4 elements were used while the order of Taylor-like expansion was varied from N=-1 to N=10 (note that N=-1 was Euler-bernoulli theory and N=0 was Timoshenko theory) in the first case (L=1m) and from -1 to

6 in the other case (L=10) . The trends obtained are shown in the figures below (3.5, 3.6, 3.7, 3.8, 3.9). It is clear that, in the case of tin beam the trends of stresses change but they remain linear, while in the case of squat beam the trend change from N=3 onwards and become not linear.

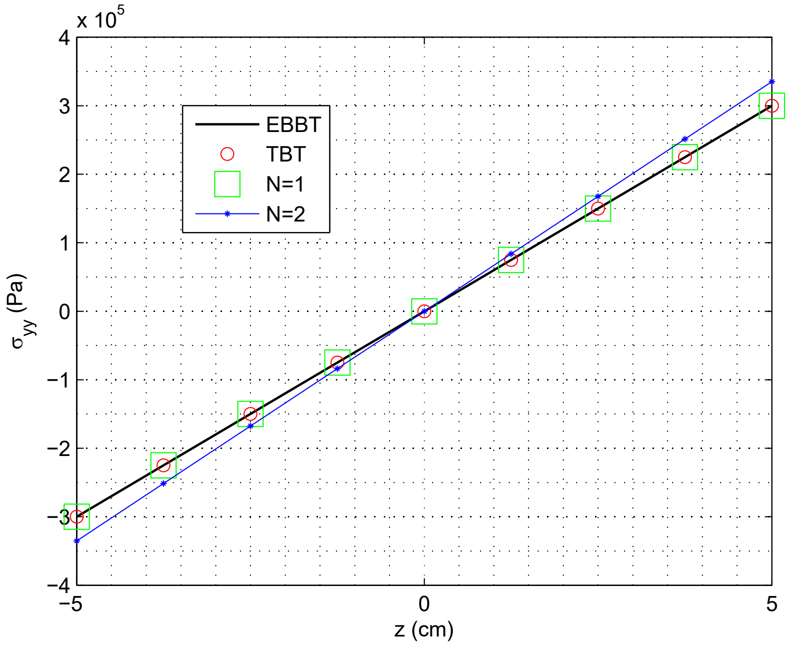

Figure 3.5: Trend of σ_{yy} stress for beam with L=1

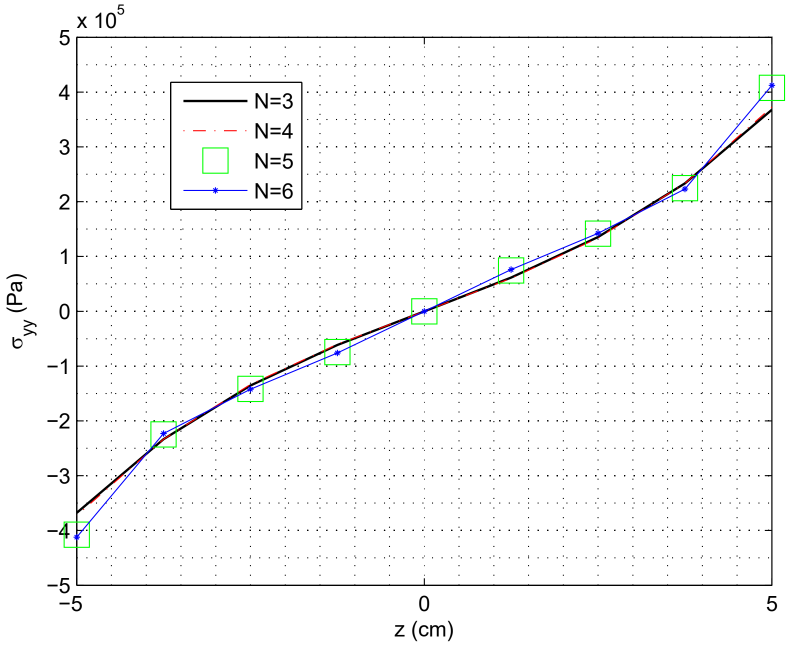

Figure 3.6: Trend of σ_{yy} stress for beam with L=1

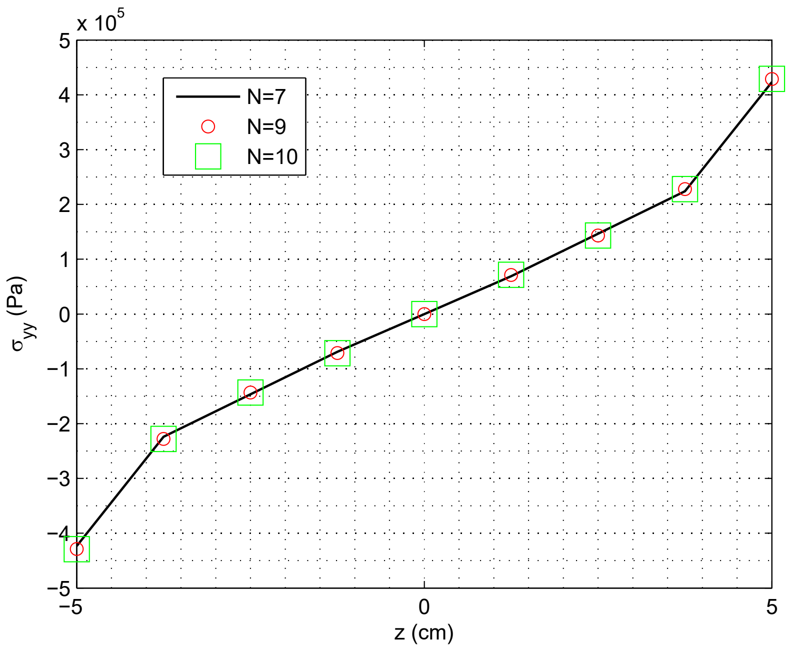

Figure 3.7: Trend of σ_{yy} stress for beam with L=1

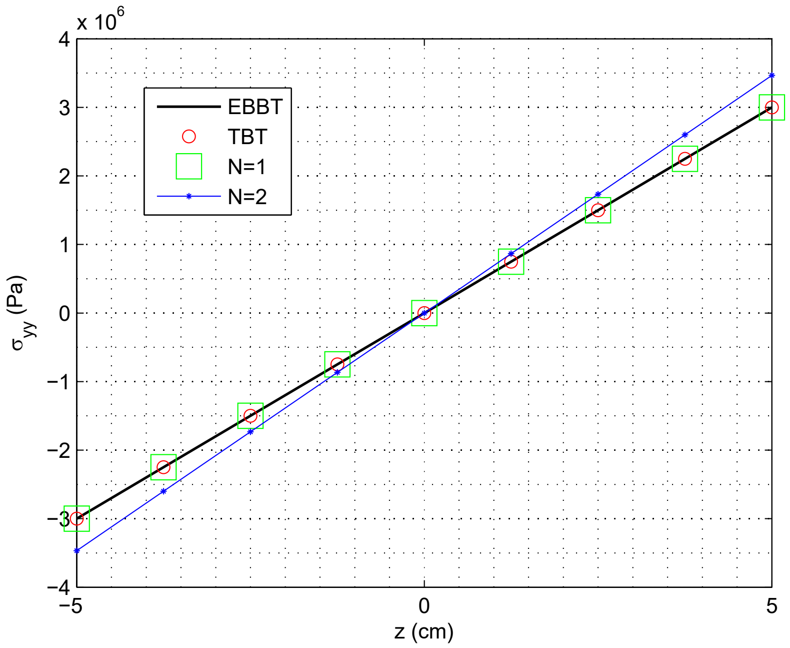

Figure 3.8: Trend of σ_{yy} stress for beam with L=10

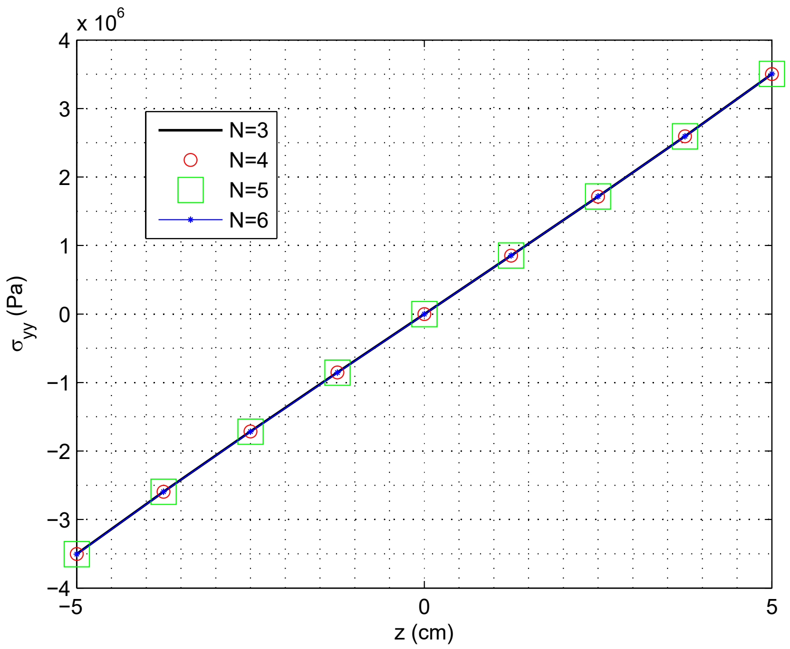

Figure 3.9: Trend of σ_{yy} stress for beam with L=10

3.4 Analysis via Lagrange polynomials

The other way to analyze the beams via FEM is to use Lagrange polynomials for the cross-section discretization. L-elements are used, in particular L9 and its multiple, and it will analyzed the displacement field and the trend of σ_{yz} stress.

3.4.1 Description of the problem

For the analysis are used the same beam of the previous chapters with the same force applied at free tip. The displacement at the free tip and the σ_{yz} trend on the middle section are evaluated by varying the discretization of the section, one, two and four L9 element are used. The coordinates of the point used for the evaluation of the trends are: x=0,$y = L/2$ and z vary from -5cm to 5cm.

3.4.2 Results

For the analysis of beams, in both the cases (L=1m;L=10m), were used: one, two and four L9 elements for the discretizzation of section, B4 beam elements on the length of beam and the number of elements were varied from 5 to 40. The results are shown in the three tables below (3.5; 3.6; 3.7).

Table 3.5: Results obtained with B4 elements and 1×L9

N° elements	σ_{yz} max [Pa]	u_z at free-end [m]	DOF
L=1m			
5-B4	$-5.297 * 10^3$	$-2.645 * 10^{-5}$	432
10-B4	$-5.285 * 10^3$	$-2.663 * 10^{-5}$	837
20-B4	$-5.286 * 10^3$	$-2.670 * 10^{-5}$	1647
40-B4	$-5.286 * 10^3$	$-2.673 * 10^{-5}$	3267
L=10m			
5-B4	$-5.289 * 10^3$	$-2.629 * 10^{-2}$	432
10-B4	$-6.008 * 10^3$	$-2.648 * 10^{-2}$	837
20-B4	$-5.094 * 10^3$	$-2.657 * 10^{-2}$	1647
40-B4	$-5.285 * 10^3$	$-2.662 * 10^{-2}$	3267

Table 3.6: Results obtained with B4 elements and 2×L9

N° elements	σ_{yz} max [Pa]	u_z at free-end [m]	DOF
L=1m			
5-B4	$-8.559 * 10^3$	$-2.648 * 10^{-5}$	720
10-B4	$-8.569 * 10^3$	$-2.666 * 10^{-5}$	1395
20-B4	$-8.569 * 10^3$	$-2.674 * 10^{-5}$	2745
40-B4	$-8.569 * 10^3$	$-2.677 * 10^{-5}$	5445
L=10m			
5-B4	$-8.804 * 10^3$	$-2.629 * 10^{-2}$	720
10-B4	$-8.445 * 10^3$	$-2.648 * 10^{-2}$	1395
20-B4	$-8.379 * 10^3$	$-2.657 * 10^{-2}$	2745
40-B4	$-8.569 * 10^3$	$-2.662 * 10^{-2}$	5445

Table 3.7: Results obtained with B4 elements and 4×L9

N° elements	σ_{yz} max [Pa]	u_z at free-end [m]	DOF
L=1m			
5-B4	$-8.552 * 10^3$	$-2.649 * 10^{-5}$	1200
10-B4	$-8.530 * 10^3$	$-2.667 * 10^{-5}$	2325
20-B4	$-8.569 * 10^3$	$-2.675 * 10^{-5}$	4575
40-B4	$-8.569 * 10^3$	$-2.678 * 10^{-5}$	9075
L=10m			
5-B4	$-8.803 * 10^3$	$-2.629 * 10^{-2}$	720
10-B4	$-8.233 * 10^3$	$-2.648 * 10^{-2}$	1395
20-B4	$-8.723 * 10^3$	$-2.657 * 10^{-2}$	2745
40-B4	$-8.585 * 10^3$	$-2.662 * 10^{-2}$	5445

3.5 Evaluation of the σ_{yz} stress trend

The purpose of the analysis is the evaluation of the σ_{yz} stress trend long the z axis. For the analysis are used Lagrange polynomials and Taylor-like expansion for section nodes, and finally them are compared with Jourawsky theory.

3.5.1 Description of problem

Let's consider the same beams (L=1m;L=10m) of the previous subchapters with the same force applied at the free tip. The σ_{yz} stress is evaluated on a specific points that are, at a later stage, interpolated with a straight line. The point have coordinate: x=0, $y = L/2$ and z that vary from -5cm to 5 cm with a step of 1.25 cm.

3.5.2 Results

For the analysis of σ_{yz} stress on the middle section of beams, 40 elements B4 were used. Moreover the order of Taylor-like was varied from N=-1 to N=10 (where N=-1 was Euler-bernoulli theory and N=0 was Timoshenko theory)and one/two/four L9 Lagrange polynomials were used. For the evaluation of stress with Jourawsky theory the following equation was used:

$$\sigma_{yz} = \frac{T}{2J}\left(\frac{h^2}{2} - z^2\right). \tag{3.2}$$

The results are shown in the next diagrams (Fig. 3.10; 3.11; 3.12; 3.13; 3.14; 3.15). It is noted that in the figures 3.12 and 3.15 only the significant trends are showed .It is clear that:

- Either way (L=1m;L=10m), the EBBT elements return a null values in all the points on the section of σ_{yz} stress. It is correct because the theory not contemplate the shear effects, the shear effects appear from N=2 onwards;

- The trends evaluated via Taylor-like expansion tend to the trend evaluated via Jourawsky theory when the order of model rise ;
- The trends evaluated via Lagrange polynomials tend to a cusp shape ;

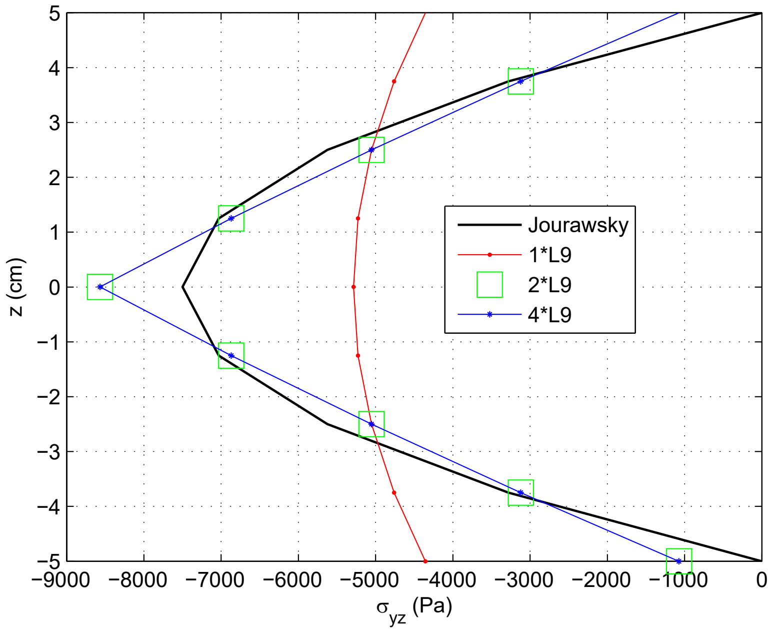

Figure 3.10: Trend of σ_{yz} stress for beam with L=1 (Lagrange polynomials)

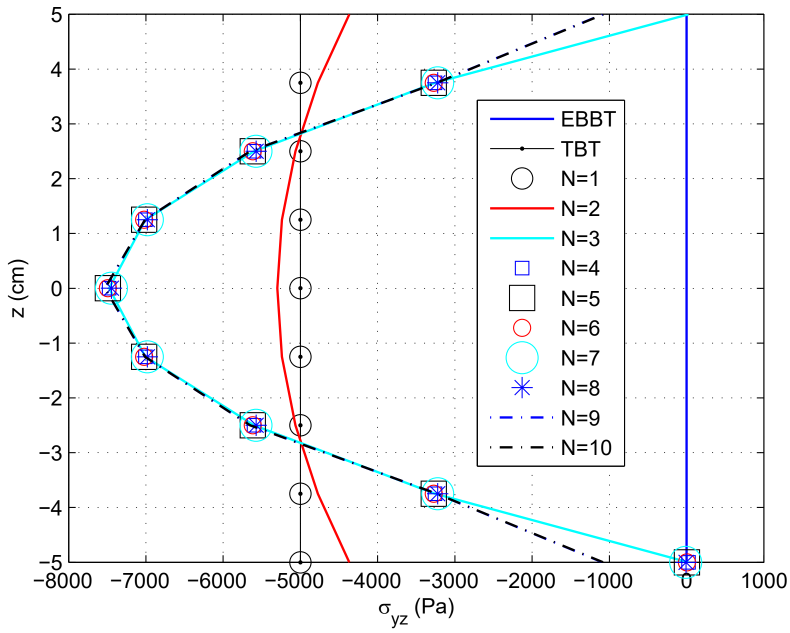

Figure 3.11: Trend of σ_{yz} stress for beam with L=1 (Taylor-like expansion)

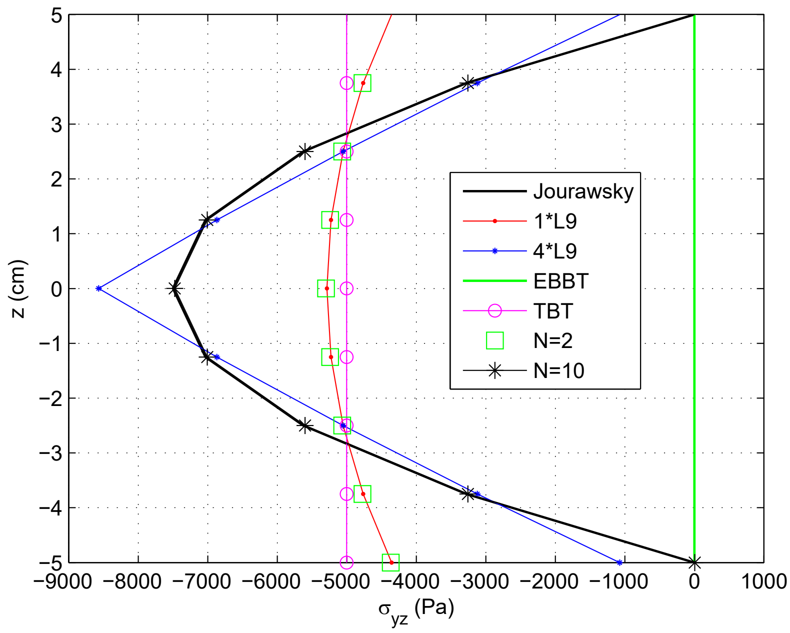

Figure 3.12: Comparison of σ_{yz} trends in the case of L=1

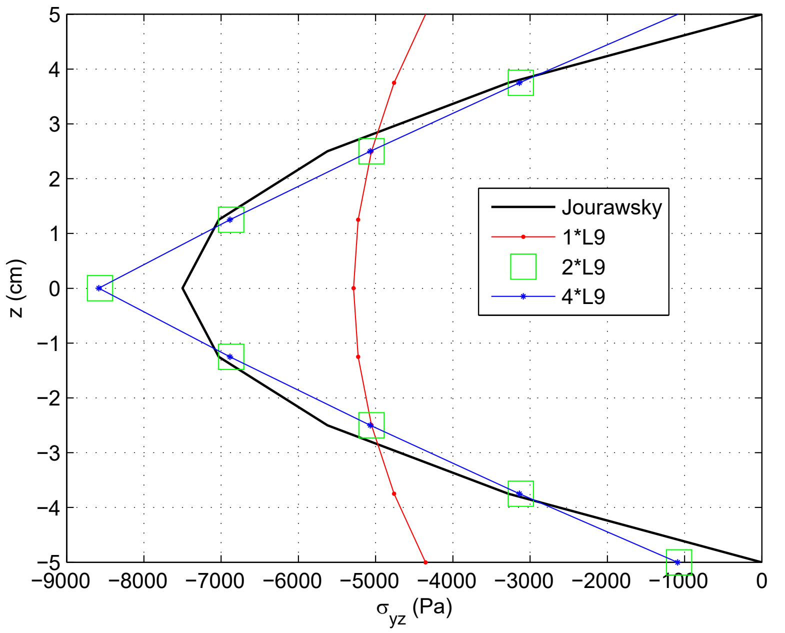

Figure 3.13: Trend of σ_{yz} stress for beam with L=10 (Lagrange polynomials)

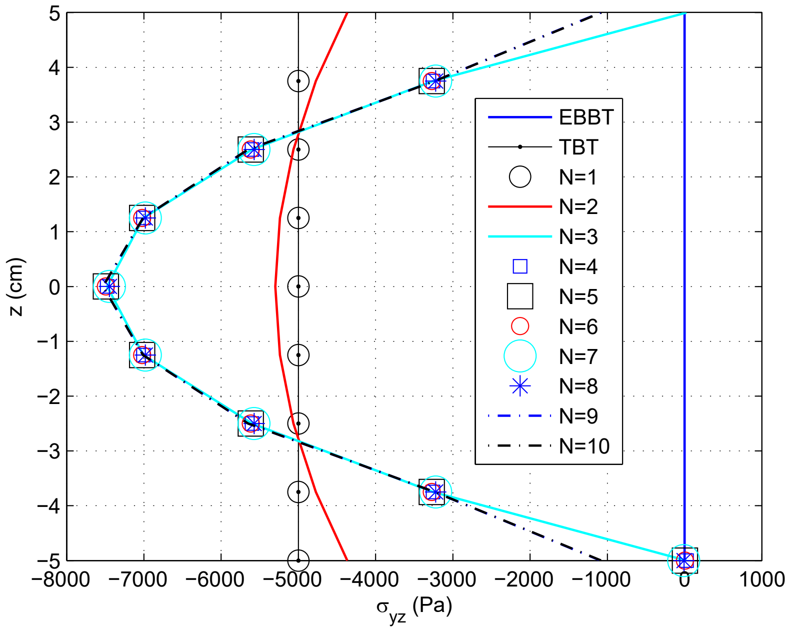

Figure 3.14: Trend of σ_{yz} stress for beam with L=10 (Taylor-like expansion)

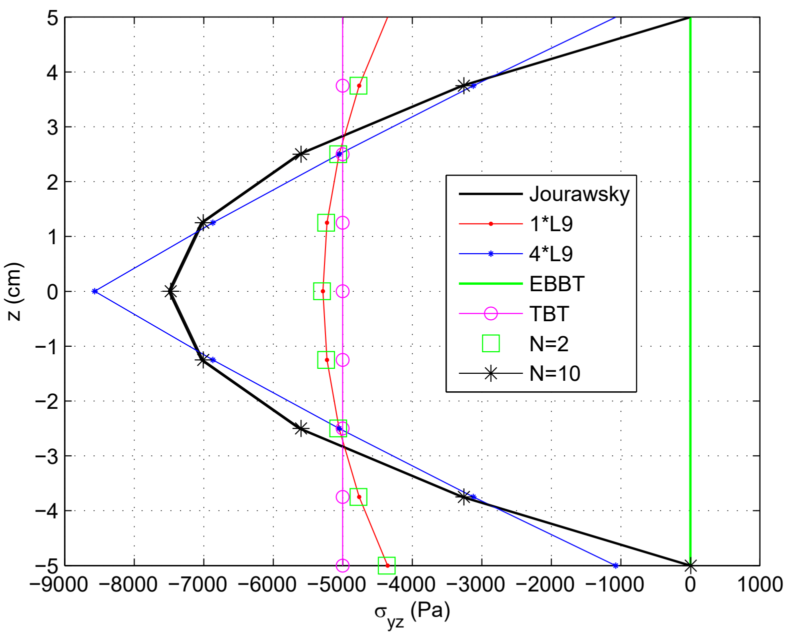

Figure 3.15: Comparison of σ_{yz} trends in the case of L=10

3.6 Static analysis of a hollow square cross-section

A clamped-clamped hollow square cross-section is considered for the next analysis, it is made with an isotropic material with $E = 75GPa$, $\nu = 0.33$ and $\rho = 2700Kg/m^3$, while the cross-section geometry is defined by $L/h = 20$, $h/t = 10$ and $h = 1m$. The purpose of the next analysis is to evaluate the displacement of the loaded points using the Taylor-like expansion and the Lagrange polynomials. For all the analysis will use 10-B4 beam elements.

3.6.1 One point load applied

In this subsection a punctual load ($P_z = 1N$) applied in point of coordinates (0,L/2,-h/2) is considered. For the cross-section discretizations, as shown in Fig. 3.16, three type of L9 mesh are used, the 8L9 mesh is symmetric, whereas 9L9 and 11L9 are mesh refined in the proximity of the loaded point.

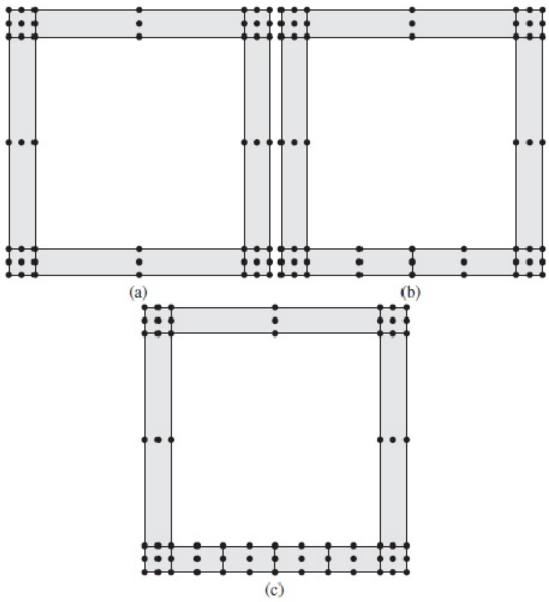

Figure 3.16: Hollow square cross-section discretization:(a)8L9;(b)9L9;(c)11L9

3.6.2 Results

The table 3.8 present the results with the number of DOFs of each model compared with reference values derived from other analysis [9].

Table 3.8: Loaded point transverse displacement of the hollow square beam.

Theory	DOFs	$u_z \times 10^8 m$	Reference [9]
TE			
EBBT	155	1.129	1.129
N=4	1395	1.209	1.209
N=8	4185	1.285	1.291
N=11	7254	1.309	1.309
LE			
8L9	4464	1.277	1.277
9L94	5022	1.308	1.308
11L9	6138	1.326	1.326

3.6.3 Two point loads applied

Two punctual loads are now applied at the same beam ($P_z = \pm 1N$) in the points of coordinate (0,L/2,$\pm\frac{H}{2}$). The L9 distribution are those shown in Fig. 3.16(a) and 3.16(b) that are symmetric and asymmetric distributions.

3.6.4 Results

The table 3.9 gives the displacement of the two loaded points u_{Ztop} and $u_{Zbottom}$ while the Fig. 3.17 shows the deformation of cross-section under the two punctual loads when a 11L9 mesh is used.

Table 3.9: Loaded points transverse displacement of the hollow square beam.

Theory	DOFs	$(u_{z-top}/u_{z-bottom}) \times 10^9 m$	Reference [9]
TE			
EBBT	155	-/+0.0	-/+0.0
N=4	1395	-/+0.178	-/+0.178
N=8	4185	-/+1.045	-/+1.046
N=11	7254	-/+1.269	-/+1.270
LE			
8L9	4464	-/+0.985	-/+0.985
11L9	6138	-0.972/1.456	-0.972/1.456

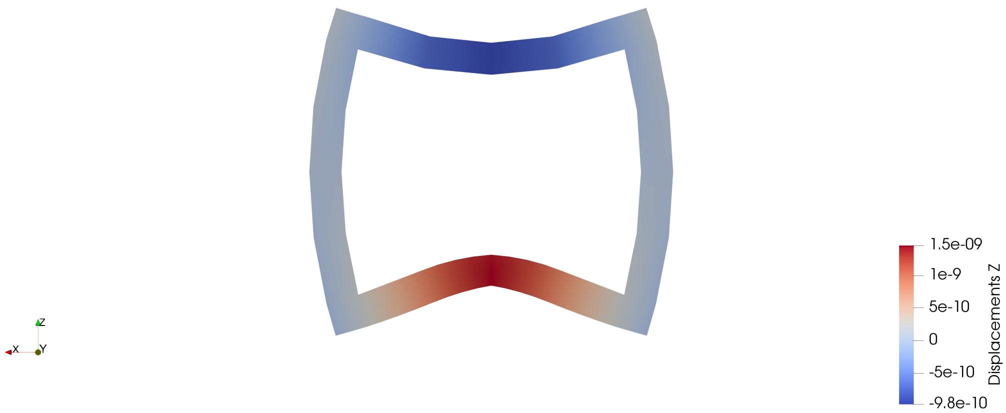

Figure 3.17: Deformation of cross-section (11L9 mesh)

3.7 Static analysis of a C-shaped cross-section beam

A clamped C-shaped cross-section beam is considered for the following analysis, it is made with the same isotropic material of previous analysis. The cross-section is represented in Fig. 3.18 and the geometrical parameters are: L/h=20, h/t=10,h=b_2=1m,$b_1 = b_2/2$.

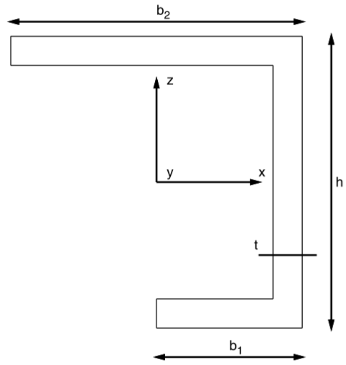

Figure 3.18: C-shaped cross-section

3.7.1 Two point loads

Two point loads are now considered ($P_z = \mp 1N$), and they are applied in two points of coordinates (0, L, ± 0.4). The displacement are evaluated in ($-b_2/2$, L, 0.4). For the analysis by Lagrange polynomials, are used two type of cross-section mesh (6L9 and 9L9) that are shown in Fig. 3.19.

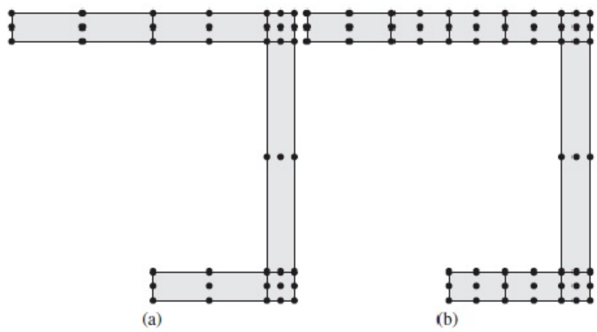

Figure 3.19: C-shaped cross-section discretization: (a)6L9;(b)9L9

3.7.2 Results

The result are summarized in the table 3.10 and in Fig. 3.20 are shown the deformation of beam under the two loads using 9L9 mesh.

Table 3.10: Transverse displacement at $(-b_2/2, L, 0.4)$.

Theory	DOFs	$u_Z \times 10^8 m$	Reference [9]
TE			
EBBT	155	0.0	0.0
N=4	1395	-0.245	-0.245
N=8	4185	-2.160	-2.161
N=11	7254	-2.563	-2.565
LE			
8L9	4464	-2.930	-2.930
11L9	6138	-2.982	-2.982

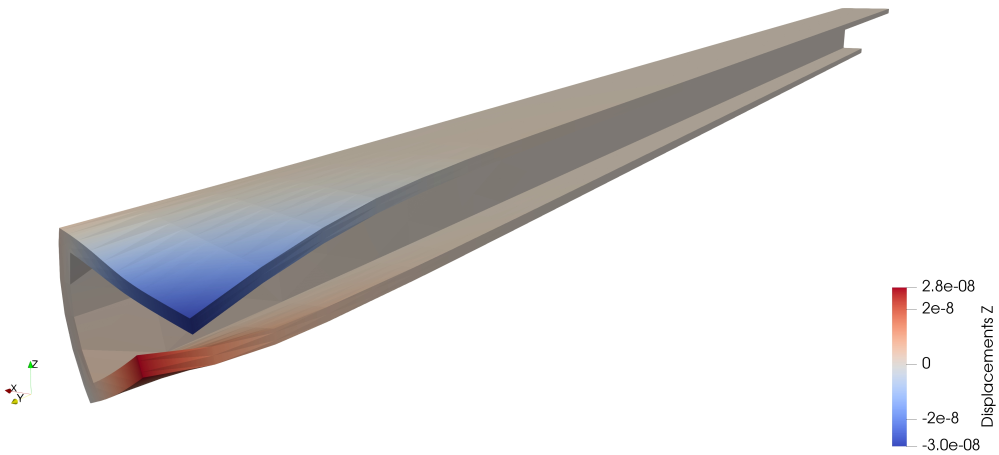

Figure 3.20: Deformed 3D configuration of C-shape cross-section beam (9L9 mesh)

3.7.3 Flexural-torsional load

A flexural-torsional load is now considered, the unitary load ($P_z = -1N$) is applied in a point of coordinate $(b_1, L, -h/2)$. Two length-to-thickness ratio are take into account L/h=20,10 and a 9L9 mesh is used for the analysis.

3.7.4 Results

The result are shown in tale 3.11 while in Fig. 3.21 is shown the deformation of L=10 cross-section beam.

Table 3.11: Transverse displacement at $(-b_2/2, L, +h/2)$.

Theory	DOFs	$u_Z \times 10^7 m$	Reference [9]
L/h=20			
9L9	5310	-14.58	-14.62
L/h=10			
9L9	5310	-2.266	-2.272

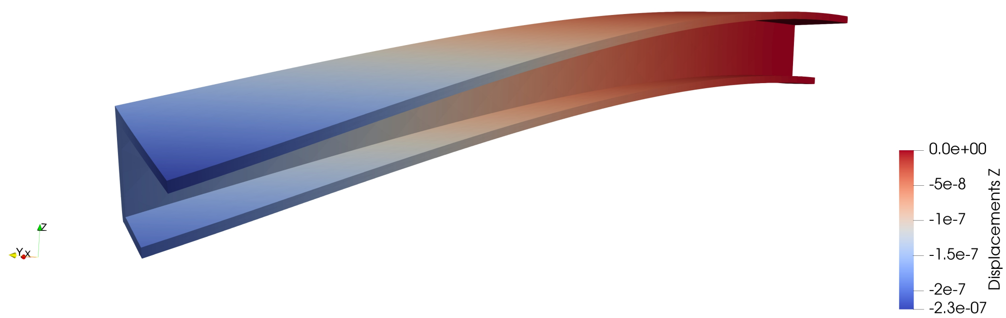

Figure 3.21: Deformed 3D configuration of beam by flexural-torsional load (9L9 mesh and L=10)

3.8 Static analysis of a open hollow square cross-section beam

An open, square cross-section is now considered, in Fig. 3.22 is shown the dimension and the material is the same of the precedent cases. Two opposite unit point loads ($\pm P_x$) are applied at (0, L, -0.45) while for the analysis are adopted three different L9 distribution that are showed in Fig. 3.23.

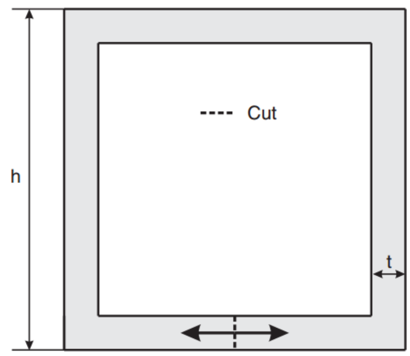

Figure 3.22: Open, hollow square cross-section.

3.8.1 Results

In the table 3.12 are summarized the result obtained by the analysis and in Fig. 3.24 is shown how the tip cross-section of beam is deformed from the loads.

Table 3.12: Horiziontal displacement at $(0, L, -h/2)$.

Theory	DOFs	$u_x \times 10^8 m$	Reference [9]
9L9	5310	4.879	4.884
11L9	6417	4.889	4.888
11L9*	6417	5.117	5.116

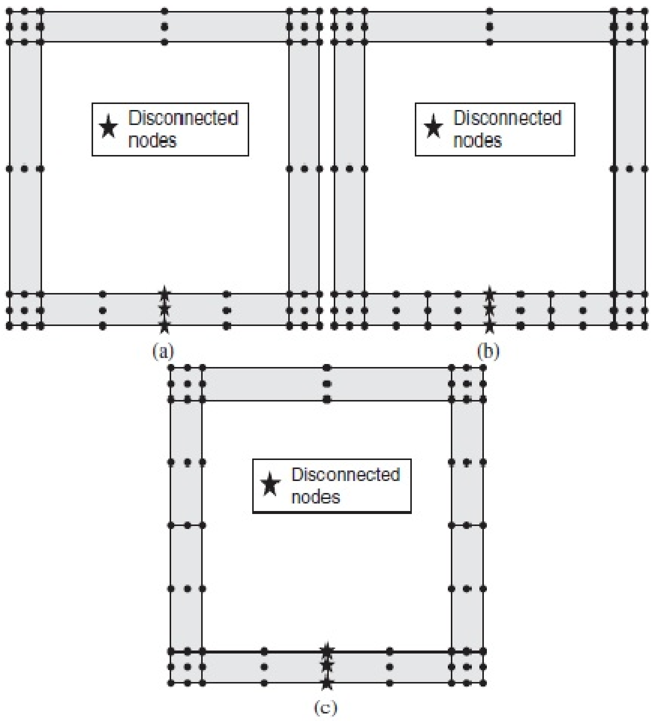

Figure 3.23: Open, hollow square cross-section discretization: (a)9L9;(b)11L9;(c)11L9*.

Figure 3.24: Deformation of C-shape cross-section (9L9 mesh)

3.9 Static analysis by solid-like geometrical BCs

In the following analysis the geometrical boundary condition will be impose over the entire cross-section.In all the following cases,the beams are made with the same isotropic material of previous analysis.

3.9.1 Compact rectangular beam

A compact rectangular beam clamped at the lateral edge is considered (Fig. 3.25), the beam have the following geometrical characteristics: L/h=100,b/h=10 and h=0.01m. A set of 21 unitary point loads is applied along the mid-span cross-section on the top surface (z=h/2) with constant step in x stating from the edge of cross-section. Two L9 distributions are adopted (5L9 and 10L9) for the analysis.

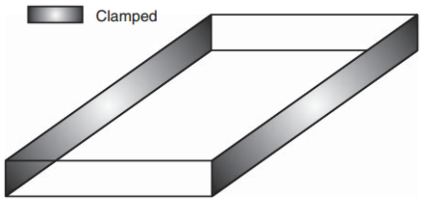

Figure 3.25: Compact rectangular beam, clamped at the edges.

3.9.2 Results

The results are showed in the table 3.13 and in Fig. 3.26 is illustrated the deformation of the middle cross-section under the effect of the loads.

Table 3.13: Trasverse displacement at $(0, L/2, 0)$ of rectangular beam.

Theory	DOFs	$u_Z \times 10^7 m$	Reference [9]
5L9	3069	-1.075	-0.959
10L9	5859	-1.110	-1.110

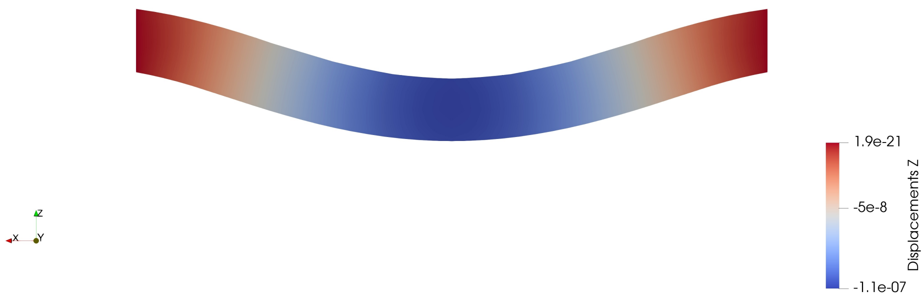

Figure 3.26: Deformation of the middle cross-section of compact rectangular beam (10L9).

3.9.3 Compact rectangular curved beam

Now let us consider a circular arch cross-section beam clamped at the lateral edges (Fig.3.27).The length of the beam (L) is equal to 2 m, the outer (r_1) and inner (r_2) radii are equal to 1 and 0.9 m, respectively. The angle of the arch (θ) is equal to $\pi/4$ rad. Three unitary point loads are applied on the bottom surface at y=0, y=L/2 and y=L with $\vartheta = \vartheta/2$ and each load acts in the radial direction from the inner to the outer direction. For the analysis is used the L9 cross-section discretization showed in Fig. 3.28.

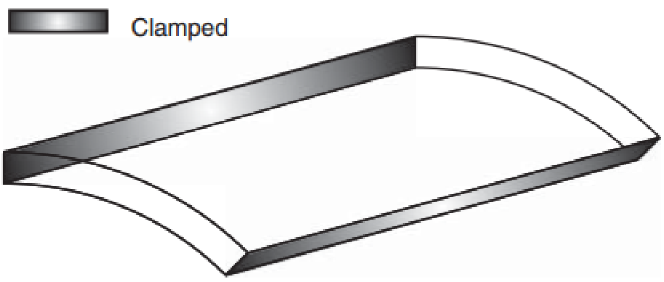

Figure 3.27: Compact rectangular curved beam, clamped at the edges.

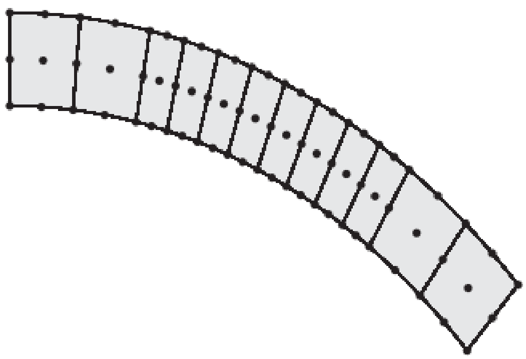

Figure 3.28: L9 mesh for the arch beam clamped at the lateral edges, 12L9.

3.9.4 Results

Table 3.14 shows the transverse displacement of a point of the mind-span cross-section and Fig. 3.26 shows the 3D deformed configuration.

Table 3.14: Trasverse displacement on the external surface of the arch beam ($y = L/2, \theta = \theta/2$)

Theory	DOFs	$u_Z \times 10^{10} m$	Reference [9]
12L9	6975	4.602	4.809

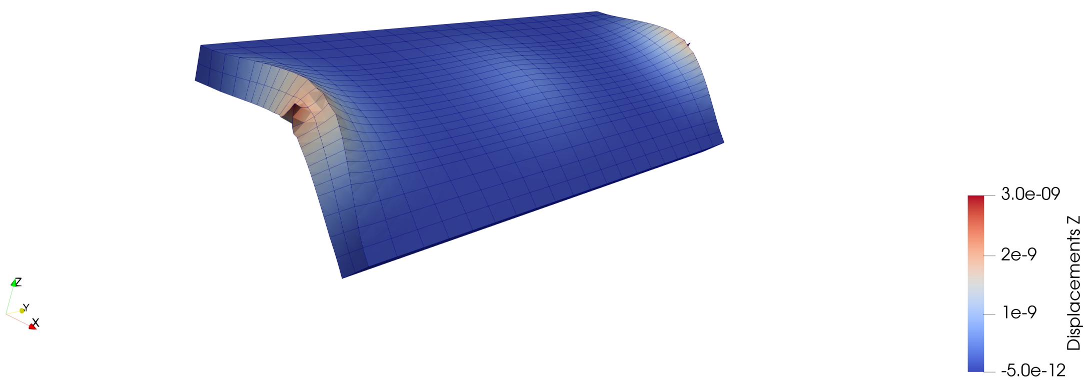

Figure 3.29: Deformed 3D configuration of the arch beam clamped at the lateral edges.

3.9.5 C-shaped cross-section beam

Finally it is taken into consideration the previous c-shaped cross-section beam (Fig. 3.18) with the same geometrical parameters.The boundary condition are shown in Fig. 3.30 and the L9 mesh shows in Fig. 3.31 is used for the analysis (13L9).Two point load ($P_z = -1N$) are applied at (0,0,0.4) and (0,L,0.4).

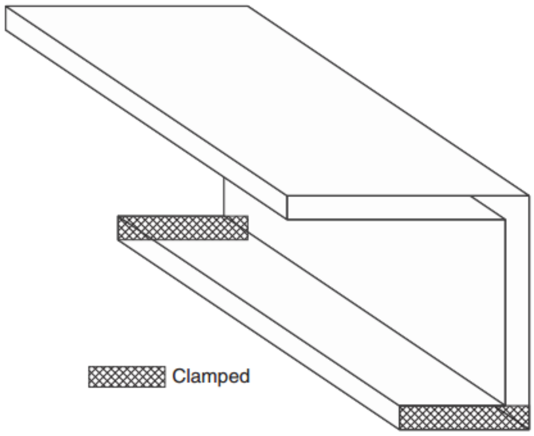

Figure 3.30: C-shaped cross-section beam,bottom flangers clamped.

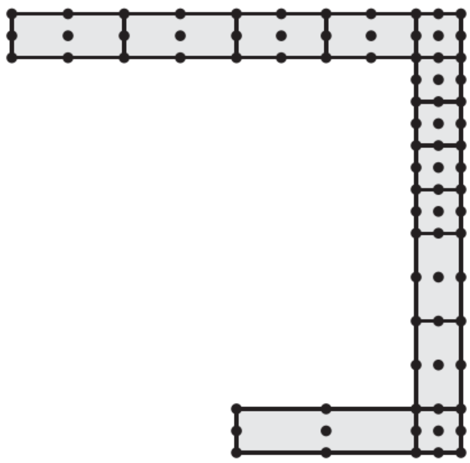

Figure 3.31: Mesh of C-shaped cross-section beam.

3.9.6 Results

The vertical displacements of loaded point are summarized in table 3.15 and in Fig 3.32 is shown the deformed 3D configuration of the entire beam.

Table 3.15: Displacement of the loading point of the C-shape beam clamped at the bottom flanges.

Theory	DOFs	$u_Z \times 10^8 m$	Reference [9]
13L9	7533	-3.686	-3.662

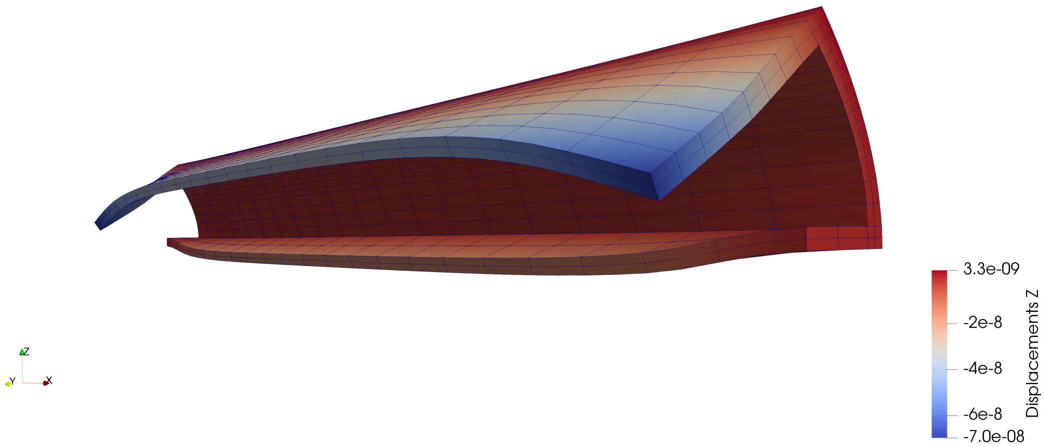

Figure 3.32: Deformed 3D configuration of the C-shaped beam clamped at the bottom flangers.

3.10 Static analysis of laminated beams

In this section will be analysed the laminated beams by Taylor-Like expansion and Lagrange polynomials.

3.10.1 Antisymmetric laminated beam

A two-layer antisymmetric beam is considered first. The dimension of the beam are the follows:

- b=0.2 m (width)
- h=0.1 m (height)
- L=2 m (length)
- L/b=10 (slenderness ratio)

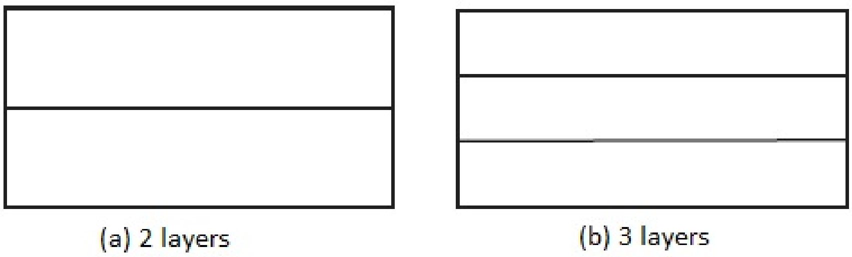

Figure 3.33: Cross-section domain configuration of the antisymmetric (a) and symmetric laminated beams (b).

The mesh of section are shown in the Fig.3.33(a)[13],in this particular case each layer has a sub-domains compose by nine nodes. An orthotropic material is employed for the two layers that has the following properties:

- $E_L = 25.0GPa$
- $E_T = E_Z = 1.0GPa$

- $\nu_{LT} = \nu_{LZ} = \nu_{TZ} = 0.25$
- $G_{LT} = 0.5GPa$
- $G_{TZ} = G_{LZ} = 0.2GPa$

An antisymmetric [0,90] cross-ply laminate is analyzed (started for the bottom) using seven B4 elements.The beam is clamped at y=0 while at y=L are applied four force in the four corners of the section, the forces have a value of 25N.

3.10.2 Results

The results obtained are shown in the table 3.16,the Fig.3.34 shows the normal stresses while the Fig.3.35 shows the shear stresses, both the stresses are evaluated at the middle section.

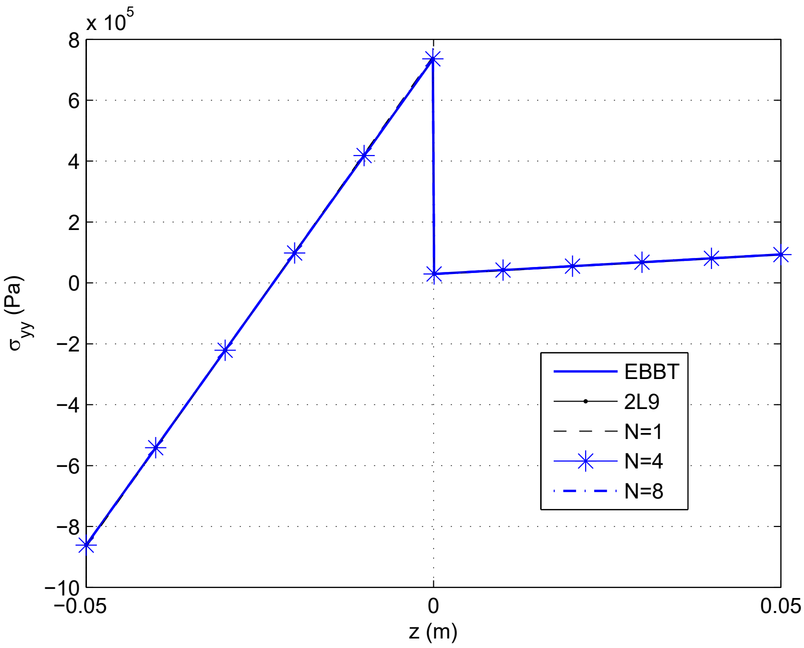

Figure 3.34: Normal stress (σ_{yy}) along the height of the middle cross section of the beam.

Table 3.16: Deflection and stresses of the antisymmetric laminated beam.

Model	$-u_z \times 10^{-3}[m]$ [0,L,h/2]	$\sigma_{yy} \times 10^3[Pa]$ [0,L/2,h/2]	$\sigma_{yz} \times 10^3[Pa]$ [0,L/2,-h/4]	DOFs
Reference[13]				
2L9	3.48	88.84	-8.18	990
SOLID	3.48	93.30	-11.36	132300
Result				
2L9	3.47	93.28	-8.17	990
EBBT	3.41	93.44	0	66
N=1	3.49	92.37	-5.04	198
N=4	3.48	93.37	-10.17	990
N=8	3.48	93.18	-11.71	2970

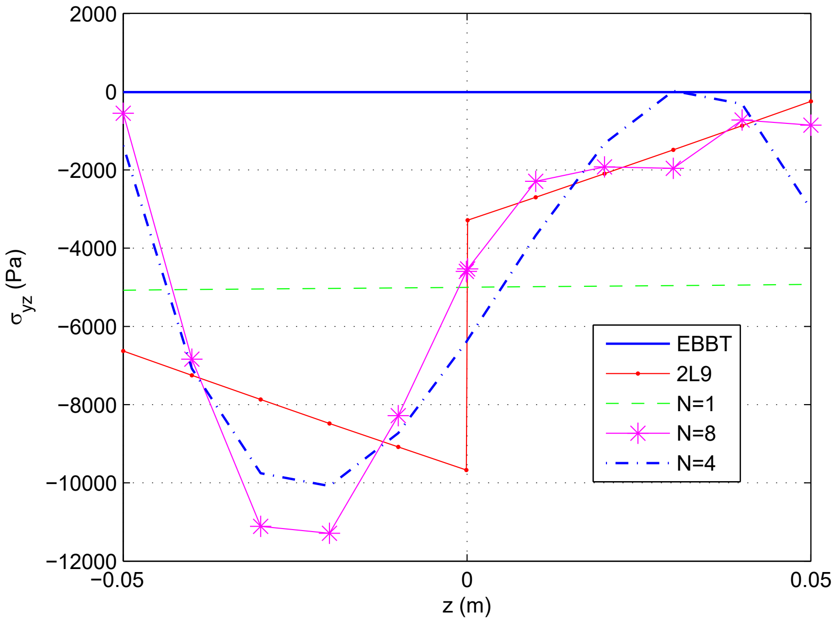

Figure 3.35: Normal stress (σ_{yz}) along the height of the middle cross section of the beam.

3.10.3 Symmetric laminated beam

The same geometry used in the previous analysis is considered again but now with three-layer symmetric [0°,90°,0°]. Material, loads and boundary condition are also the same and the cross-section domain division for analysis is shown in Fig.3.33(b).

3.10.4 Results

The table 3.17 shows the results obtained while in Fig. 3.36 and in Fig. 3.37 are shown normal and shear stresses distribution along the z-axis at the mind-span of beam.

Table 3.17: Deflection and stresses of the symmetric laminated beam.

Model	$-u_z \times 10^{-3}[m]$ [0,L,h/2]	$\sigma_{yy} \times 10^3[Pa]$ [0,L/2,h/2]	$\sigma_{yz} \times 10^3[Pa]$ [0,L/2,-h/4]	DOFs
Reference[13]				
2L9	0.72	269.24	-6.91	1386
SOLID	0.72	311.07	-6.92	195300
Result				
2L9	0.72	311.04	-6.91	1386
EBBT	6.64	311.06	0	66
N=1	0.71	311.06	-5.0	198
N=4	0.72	310.90	-7.36	990
N=8	0.72	310.96	-7.03	2970

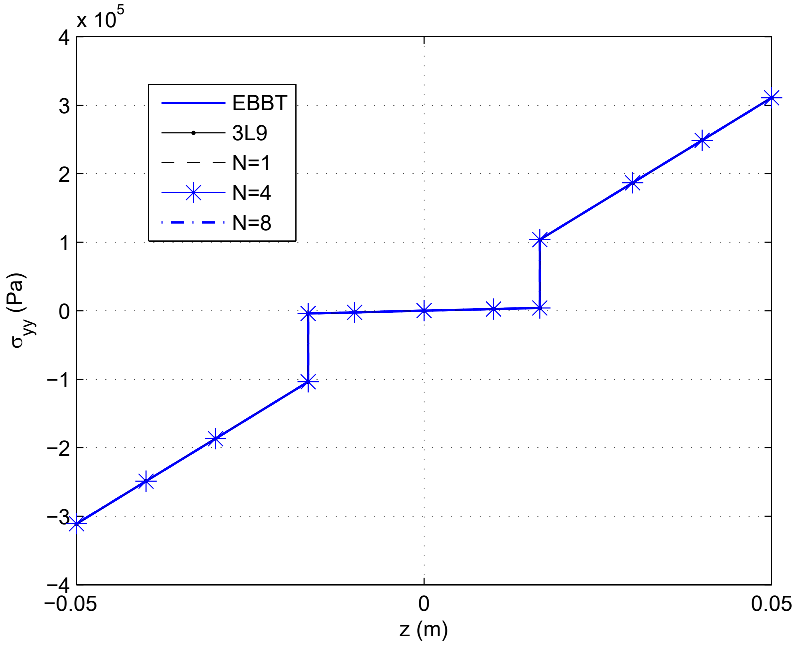

Figure 3.36: Normal stress (σ_{yy}) along the height of the middle cross section of the beam.

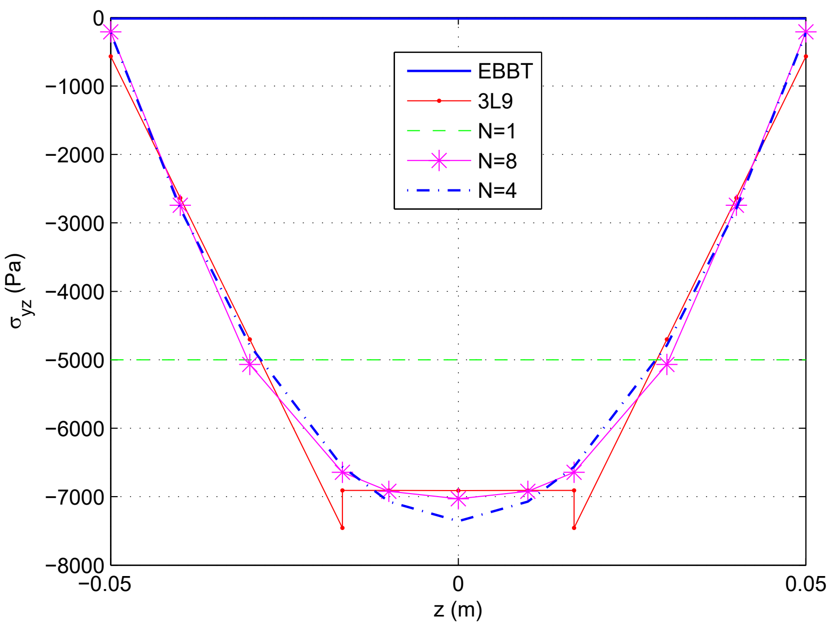

Figure 3.37: Normal stress (σ_{yz}) along the height of the middle cross section of the beam.

3.10.5 Eight-layer composite beam

For the third analysis a thick eight layer cantilever beam is considered. The Fig.3.38 shows the geometric characteristic of beam and the lamination sequence. Two different material are employed for the lamination that are marked with the numbers 1 and 2. Both have the same elastic modulus in the transversal direction $E_T = 1.0GPa$, shear modulus $G_{TL} = 0.5GPa$ and the poisson ratio $\nu = 0.25$ (equal for all direction). They have a different elastic modulus, which is $E_L = 30GPa$ for material one and $E_L = 5GPa$ for material two. Four equal loads are applied at the corners of tip cross-section, each of F=-0.05N.

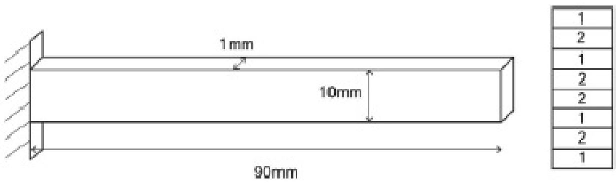

Figure 3.38: Representation of the eight-layer beam and the lamination sequence.

3.10.6 Results

In the Fig.3.39 and 3.40 are shown respectively the normal and shear stress distribution along the z-axis at mid-span while in table 3.18 are summarized the results.

Table 3.18: Maximum deflection and longitudinal stress at mid span of the eight-layers composite beam.

Model	$-u_z \times 10^{-5}[m]$ [0,L,h/2]	$\sigma_{yy} \times 10^3[Pa]$ [0,L/2,h/2]	DOFs
Reference[13]			
8L9	3.03	730	4743
N=1 zz	2.99	730	279
N=2 zz	2.99	730	558
N=3 zz	3.03	729	930
N=9 zz	3.04	661	5115
Result			
8L9	3.03	730	4743
N=1	2.99	730	279
N=2	2.98	730	558
N=3	3.03	730	930
N=9	3.03	730	5115

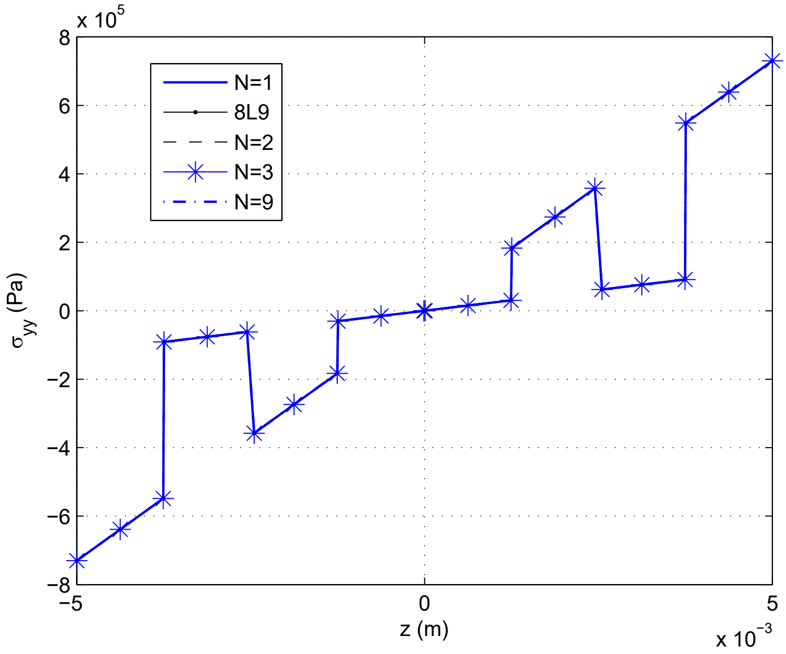

Figure 3.39: Normal stress distribution along the z-axis for the eight-layer composite beam.

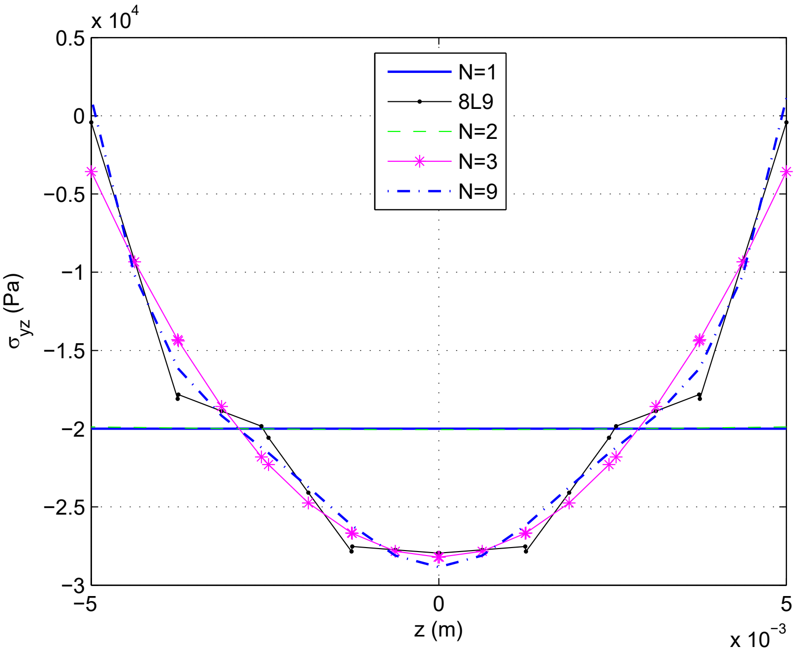

Figure 3.40: shear stress distribution along the z-axis for the eight-layer composite beam.

3.11 Single-cell box beam

In this subsection a beam with a thin-walled cross-section is analyzed . The cross-section dimension are: b=24.2mm, h=13.6mm and t=0.762mm (Fig.3.41) also it is divided in 16 sub-domains as shows the Fig.3.42 .Three different slenderness ratio (L/b) are considered 10,20 and 30 and each wall of beam consist in a two-layer lamination: [0°,90°] for the flangers and [−45°,+45°] for the webs (0° and −45° are placed outwards). The orthotropic material used have the following characteristics: $E_L = 69.0GPa$,$E_T = E_z = 10.0GPa$, $\nu = 0.25$ (for all direction) and G=6GPa (for all direction). The beam is clamped at one edge and loaded with two vertical forces (F=50N) each applied at the top of corners of the tip.

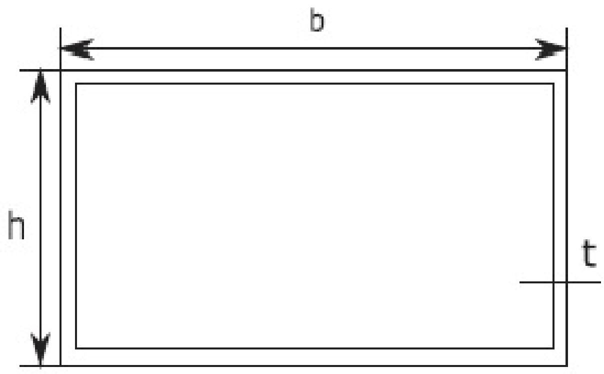

Figure 3.41: Box section geometry.

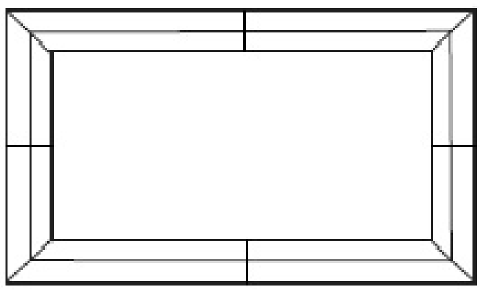

Figure 3.42: Cross-section domain distribution.

3.11.1 Results

In Fig.3.43 are shown the normal stress distribution along the thickness of the top flange at middle section for the slenderness 10 while in Fig.3.44 and Fig.3.45 are shown the shear stress long the inner an outer layer of the right web. Finally in tables 3.19,3.20 and 3.21 are shown the results for the three slenderness.

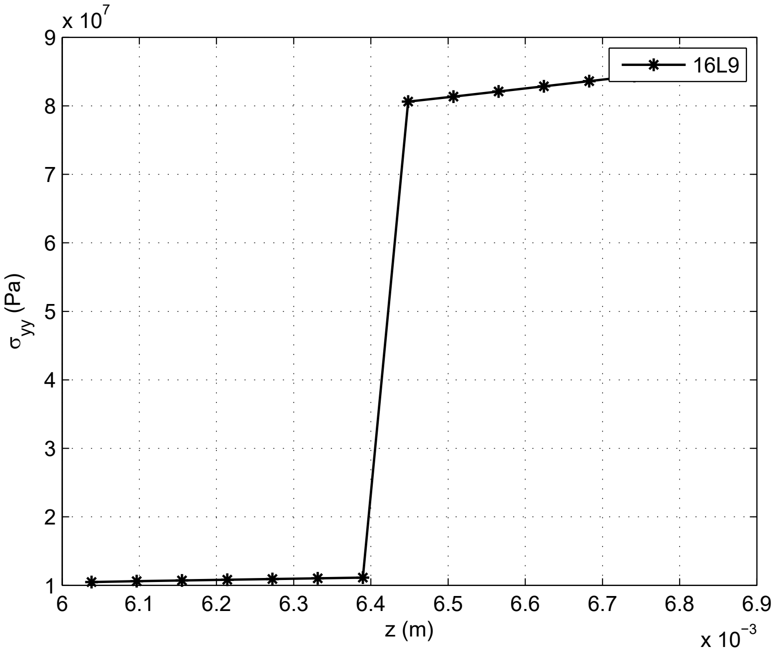

Figure 3.43: Normal stress distribution along the thickness of top flange.

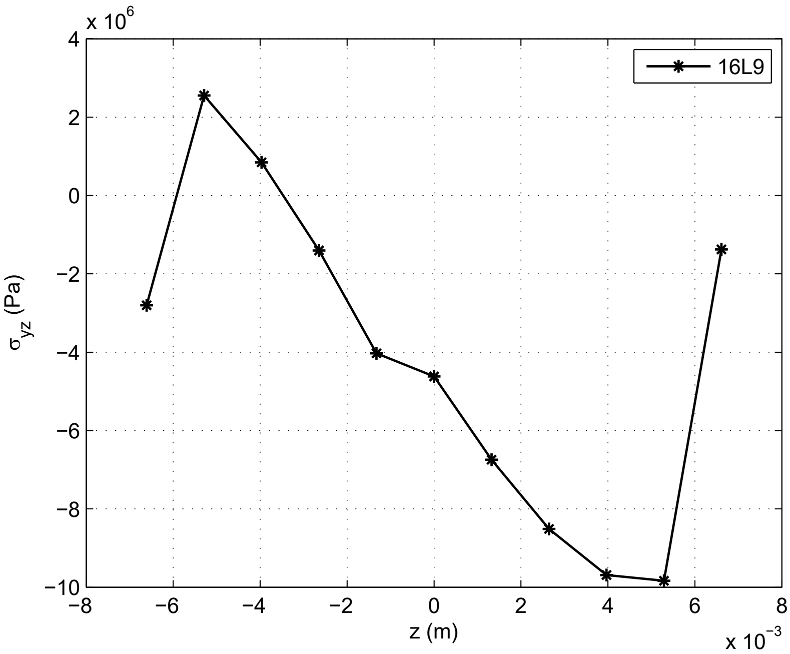

Figure 3.44: shear stress distribution along the z-axis of the right web (inner layer).

Table 3.19: Displacements and stresses of the single-cell beam (L/b=10).

Model	$-u_z \times 10^{-3}[m]$ [0,L,h/2]	$\sigma_{yy} \times 10^6[Pa]$ [0,L/2,h/2]	$\sigma_{yy} \times 10^6[Pa]$ [0,0,h/2]	$\sigma_{yz} \times 10^6[Pa]$ [b/2,L/2,h/4]	DOFs
Reference[13]					
16L9	7.16	85.80	167.74	-8.31	7740
EBBT	7.09	85.24	170.48	0	155
TBM	7.15	85.27	170.51	-6.40	600
N=3	7.09	84.44	163.50	-9.64	930
N=6	7.16	85.30	165.77	-8.94	2604
Results					
16L9	7.16	85.11	163.28	-8.73	7440
EBBT	7.11	85.32	170.63	0	93
TBM	7.17	85.28	163.04	-6.56	155
N=3	7.11	84.65	163.04	-9.72	930
N=6	7.17	85.15	160.47	-7.99	2604

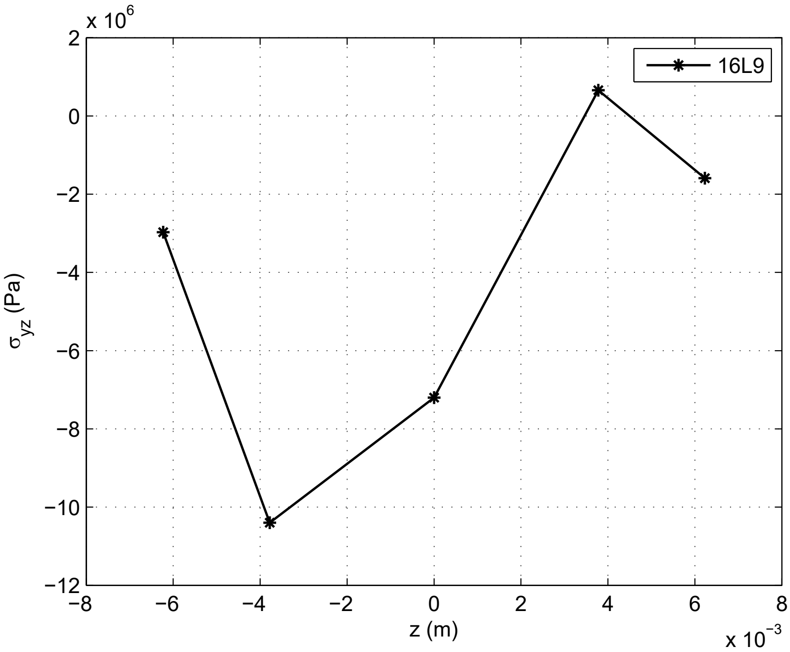

Figure 3.45: shear stress distribution along the z-axis of the right web (outer layer).

Table 3.20: Displacements and stresses of the single-cell beam (L/b=20).

Model	$-u_z \times 10^{-3}[m]$ [0,L,h/2]	$\sigma_{yy} \times 10^6[Pa]$ [0,L/2,h/2]	$\sigma_{yy} \times 10^6[Pa]$ [0,0,h/2]	$\sigma_{yz} \times 10^6[Pa]$ [b/2,L/2,h/4]	DOFs
Reference[13]					
16L9	56.70	170.52	336.49	-12.11	7740
EBBT	56.43	170.48	340.96	0	155
TBM	56.51	170.48	340.96	-10.30	600
N=3	55.86	169.19	331.75	-14.74	930
N=6	56.25	170.88	332.18	-13.66	2604
Results					
16L9	56.76	170.75	331.92	-13.61	7440
EBBT	56.89	170.63	341.27	0	93
TBM	57.0	170.60	341.23	-10.62	155
N=3	56.31	169.20	331.03	-15.32	930
N=6	56.73	170.94	328.81	-11.82	2604

Table 3.21: Displacements and stresses of the single-cell beam (L/b=30).

Model	$-u_z \times 10^{-3}[m]$ [0,L,h/2]	$\sigma_{yy} \times 10^6[Pa]$ [0,L/2,h/2]	$\sigma_{yy} \times 10^6[Pa]$ [0,0,h/2]	$\sigma_{yz} \times 10^6[Pa]$ [b/2,L/2,h/4]	DOFs
Reference[13]					
16L9	191.85	256.23	504.25	-15.63	7740
EBBT	191.45	255.72	511.45	0	155
TBM	191.71	255.72	511.45	-14.21	600
N=3	189.39	253.92	499.62	-19.66	930
N=6	190.59	256.71	500.89	-18.36	2604
Results					
16L9	191.11	256.39	500.58	-18.49	7440
EBBT	192.00	255.95	511.91	0	93
TBM	192.17	255.92	511.87	-14.68	155
N=3	189.70	255.78	498.72	-15.37	930
N=6	190.99	256.26	498.37	-15.51	2604

3.12 Multi cell box beam

A two-cell cantilever beam with a cut is now considered. The lamination and the dimension are the same as the single-cell beam, but a third web is added in the middle of the section with a lamination $[-45°,45°]$ and also a cut is placed at the bottom of the right cell. Two vertical and horizontal point loads of 50N each are applied at the tip section. The two vertical forces are directed upwards and they are located at the two corners of the top flange. The two horizontal loads have a opposite direction and are applied at the two bottom corners, in order to open the right cell.

3.12.1 Results

The Fig. 3.46 displays the deformed configuration of the tip section while the Fig. 3.47 and 3.48 show the normal and shear stresses distribution on the tip section.

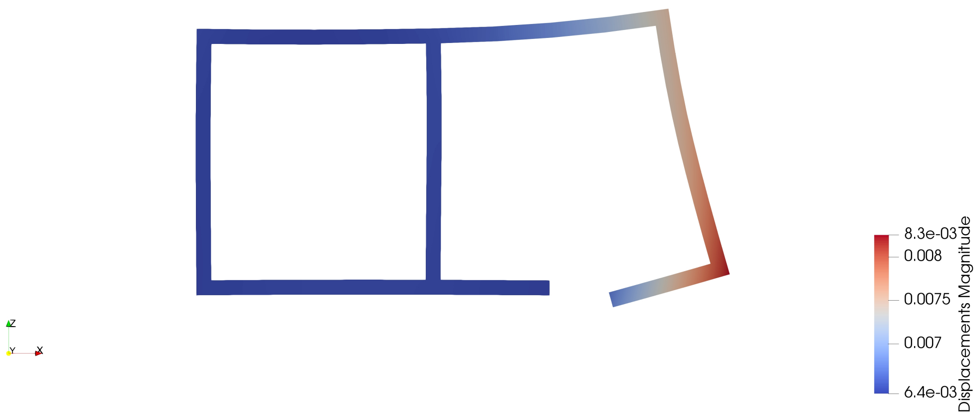

Figure 3.46: Deformed cross-section at the tip of the two-cell beam.

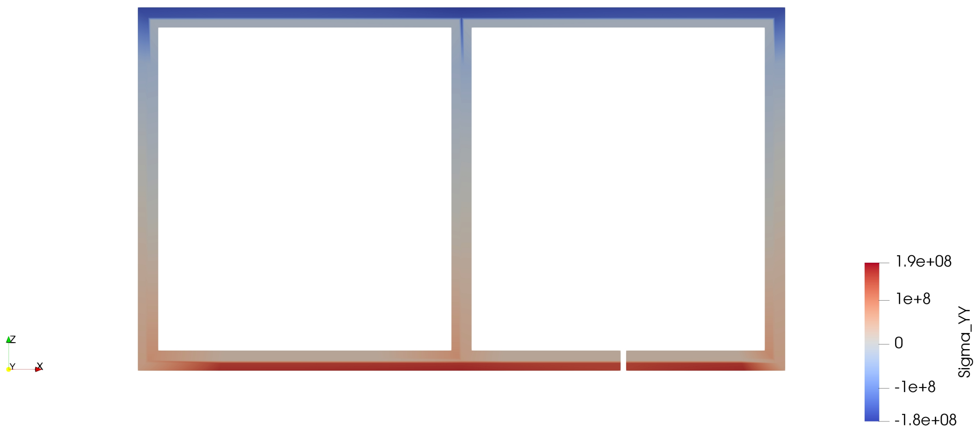

Figure 3.47: Normal stress distribution at mid span.

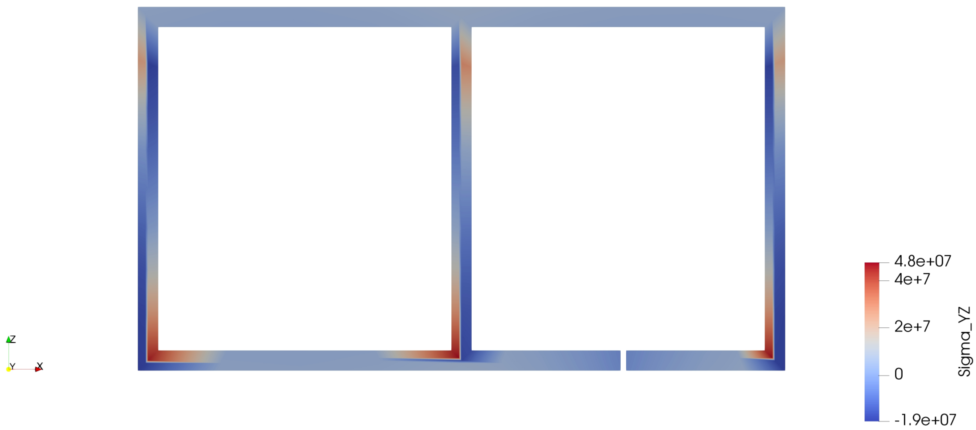

Figure 3.48: Shear stress distribution at mid span.

3.13 Single and double cell static analysis

In this section a new structural model is considered. At the first a single fiber-matrix cell is analyzed, it represent simplest element of a more complex composite structure and it can be assembled in sequence to simulate a realistic one. The Fig.3.49 represents the cross-section of the model and the reference system, it is a square cell with: $b = 0.1mm$, diameter of fiber $d = 0.08mm$ and $L/b = 10$. Two isotropic material are used for fiber and the matrix and the property are the following:

- For fiber $E = 202.038GPaand\nu = 0.2128$
- For matrix $E = 3.252GPaand\nu = 0.355$

The structure is clamped at $y = 0$ and loaded in the point of coordinate $(b/2, L,0)$ with a vertical force $F_Z = -0.1N$. For the analysis are used $40 - B4$ elements for Taylor-like expansion and $10 - B4$ elements for Lagrange expansion, while the cross-section discretization (for both models) is shown in Fig3.49.

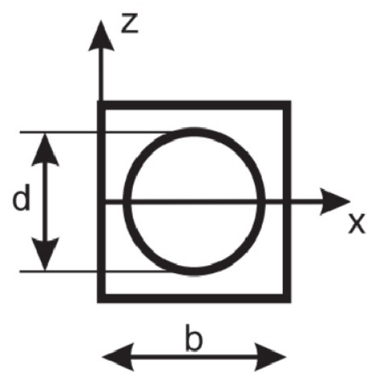

Figure 3.49: Single fibre-matrix cross-section [14]

The double cell model is obtained by two single cell placed side by side how is shown in Fig3.51. For the analysis, the same discretization of the cross-section, number of beam elements and materials are used. It is necessary to specify that

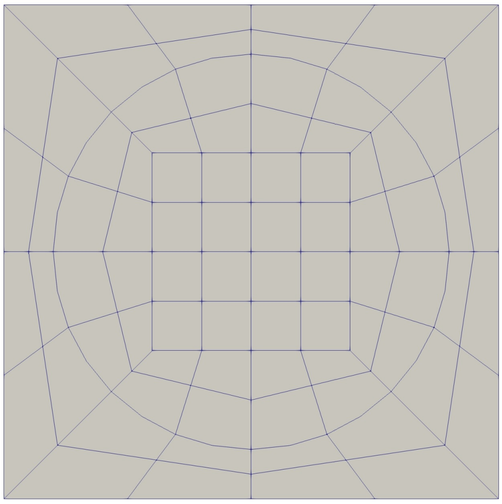

Figure 3.50: Single cell cross-section discretization with 20L9 elements

now $a = 2b$. The structure is clamped at $y = 0$ and loaded with two vertical forces ($F_Z = -0.05$) in A($a/4, L, b/2$) and B($3a/4, L, b/2$).

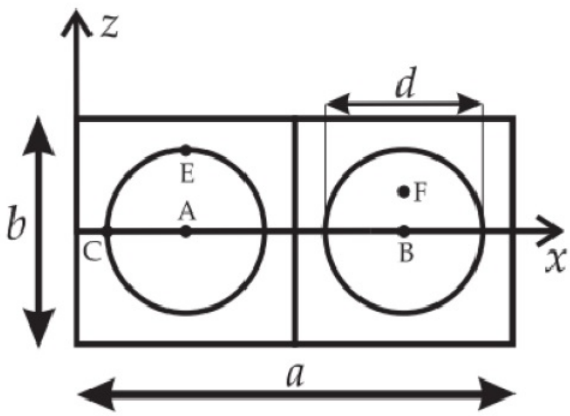

Figure 3.51: Double fibre-matrix cross-section [14]

3.13.1 Results of single cell model

In the tables 3.22 and 3.23 are summarized and compared[14] the results. Furthermore a solid model is created and analyzed by abaqus software and for the analysis a 20 nodes brick is used. In Fig 3.52 and 3.53 are shown the vertical displacement and the σ_{yy} stress on the clamped section.

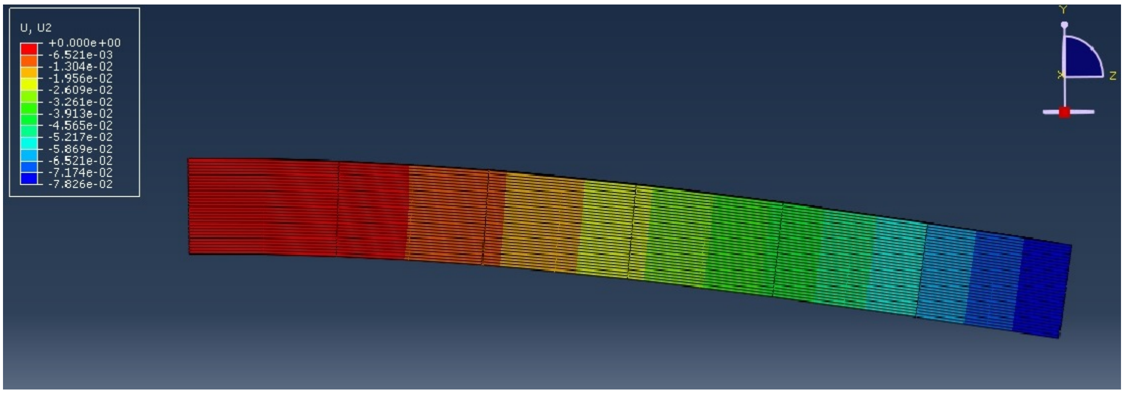

Figure 3.52: Vertical displacement field evaluated by abaqus software

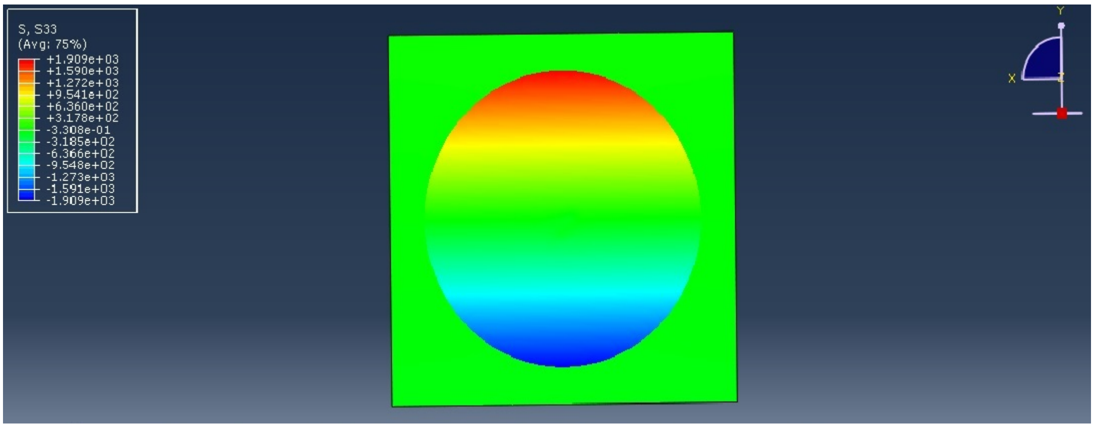

Figure 3.53: σ_{yy} stress on clamped section evaluated by abaqus software

3.13.2 Results of double cell model

In the table 3.24 and 3.25 are summarized and compared[14] the results. Furthermore a solid model is created and analyzed by abaqus software and for the analysis

Table 3.22: Deflection and stresses of single-cell model.

Model	$-u_z \times 10^2[mm]$ [b/2,L,0]	$\sigma_{yy} \times 10^{-2}[MPa]$ [b/2,L/2,d/2]	DOFs
Reference[14]			
EBBT	-7.81	9.47	363
TBT	-7.83	9.47	605
N=1	-7.85	9.47	1089
N=2	-7.77	9.36	2178
N=3	-7.78	9.36	3630
N=4	-7.79	9.33	5445
N=5	-7.78	9.33	7623
N=6	-7.80	9.32	10164
N=7	-7.80	9.32	13068
N=8	-7.80	9.35	16335
12L9+8L6	-7.93	9.45	7533
SOLID	-7.82	9.49	268215
Result			
EBBT	-7.83	9.49	363
TBT	-7.85	9.49	605
N=1	-7.85	9.49	1089
N=2	-7.78	9.37	2178
N=3	-7.79	9.37	3630
N=4	-7.80	9.34	5445
N=5	-7.81	9.34	7623
N=6	-7.81	9.33	10164
N=7	-7.81	9.33	13068
N=8	-7.82	9.36	16335
20L9	-7.82	9.39	8277
SOLID	-7.82	9.46	56613

Table 3.23: Deflection and stresses of single-cell model.

Model	$\sigma_{yy} \times 10^{-2}[MPa]$ [b/2,L/2,0.03]	$\sigma_{yz} \times 10^{-1}[MPa]$ [0.01,L/2,d/2]	DOFs
Reference[14]			
EBBT	7.10	-	363
TBT	7.10	-1.96	605
N=1	7.10	-1.96	1089
N=2	7.02	-2.31	2178
N=3	7.02	-2.46	3630
N=4	7.02	-2.45	5445
N=5	7.11	-2.37	7623
N=6	7.11	-2.37	10164
N=7	7.12	-2.30	13068
N=8	7.05	-2.30	16335
12L9+8L6	7.05	-2.50	7533
SOLID	7.09	-2.38	268215
Result			
EBBT	7.12	-	363
TBT	7.12	-2.83	605
N=1	7.12	-2.83	1089
N=2	7.03	-2.83	2178
N=3	7.03	-2.38	3630
N=4	7.10	-3.13	5445
N=5	7.10	-2.42	7623
N=6	7.11	-2.34	10164
N=7	7.11	-2.12	13068
N=8	7.13	-2.11	16335
20L9	7.09	-3.25	8277
SOLID	7.09	-2.34	56613

a 20 nodes brick is used. In Fig 3.54 and 3.55 are shown the vertical displacement and the σ_{yy} stress on the clamped section.

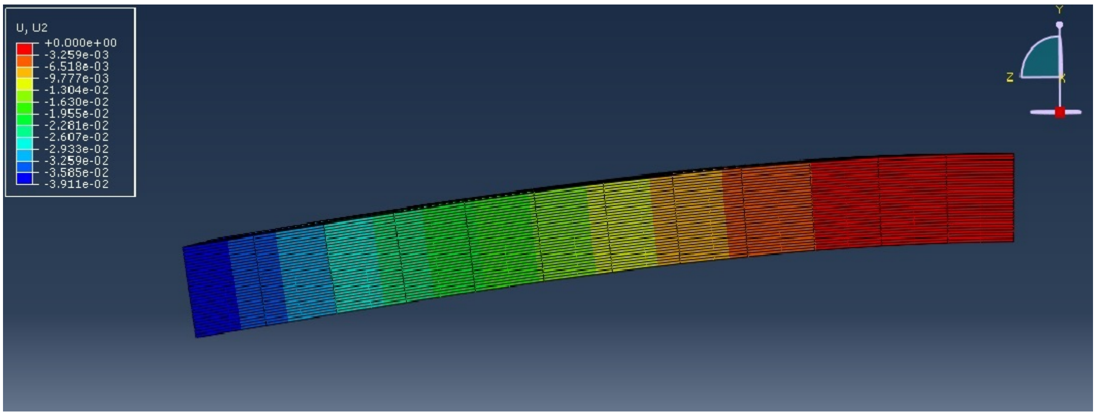

Figure 3.54: Vertical displacement field evaluated by abaqus software

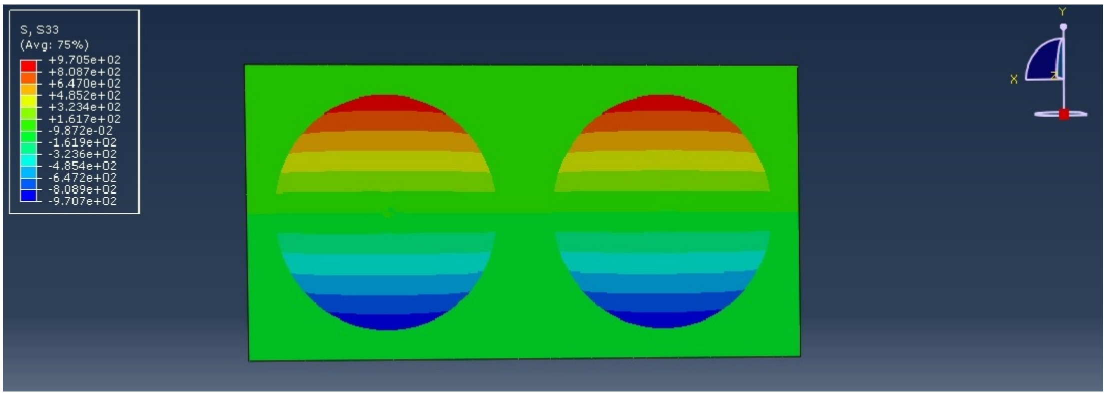

Figure 3.55: σ_{yy} stress on clamped section evaluated by abaqus software

Table 3.24: Deflection and stresses of double-cell model.

Model	$-u_z \times 10^2 [mm]$ [a/4,L,b/2]	$\sigma_{yy} \times 10^{-2} [MPa]$ [a/4,L/2,0.03]	DOFs
Reference[14]			
EBBT	-3.91	4.73	363
TBT	-3.92	4.73	605
N=1	-3.92	4.73	1089
N=2	-3.87	4.68	2178
N=3	-3.87	4.68	3630
N=4	-3.88	4.63	5445
20L9+16L6	-3.96	4.65	12555
SOLID	-3.90	4.74	536430
Result			
EBBT	-3.92	4.74	363
TBT	-3.93	4.74	605
N=1	-3.93	4.74	1089
N=2	-3.88	4.68	2178
N=3	-3.88	4.68	3630
N=4	-3.90	4.63	5445
40L9	-4.05	4.69	16089
SOLID	-3.90	4.72	214437

Table 3.25: Deflection and stresses of double-cell model.

Model	$\sigma_{yy} \times 10^{-2} [MPa]$ [3/4a,L/2,0.03]	$\sigma_{yz} \times 10^{-1} [MPa]$ [0.01,L/2,0]	DOFs
Reference[14]			
EBBT	3.55	-	363
TBT	3.55	-0.98	605
N=1	3.55	-0.98	1089
N=2	3.51	-1.59	2178
N=3	3.51	-1.77	3630
N=4	3.51	-1.76	5445
20L9+16L6	3.52	-1.58	12555
SOLID	3.55	-1.52	536430
Result			
EBBT	3.56	-	363
TBT	3.56	-0.98	605
N=1	3.56	-0.98	1089
N=2	3.51	-1.59	2178
N=3	3.51	-1.77	3630
N=4	3.51	-1.76	5445
40L9	3.54	-1.50	16089
SOLID	3.55	-1.53	214437

3.14 Static Analysis of a cross-ply laminate by different models

Let us consider a cross-ply plate [14], it is composed by three layers oriented at [0°,90°,0°] and it have the following geometric parameters: length $L = 40mm$, width $b = 0.8mm$, height $h = 0.6mm$ and diameter of fibers $d = 0.02mm$ (As shown in Fig 3.56). The same plate is analyzed with four different model and the component have the following mechanical characteristic:

- Fiber is considered orthotropic: $E_1 = 202.038GPa$, $E_2 = E_3 = 12.134GPa$, $G_{12} = G_{13} = 8.358GPa$, $G_{23} = 47.756GPa$, $\nu_{12} = \nu_{13} = 0.2128$ and $\nu_{23} = 0.2704$;
- Matrix is an isotropic material: $E = 3.252GPa$ and $\nu = 0.355$;
- Layer properties are the following: $E_1 = 159.38GPa$, $E_2 = E_3 = 14.311GPa$, $G_{12} = G_{13} = 3.711GPa$, $G_{23} = 5.209GPa$, $\nu_{12} = \nu_{13} = 0.2433$ and $\nu_{23} = 0.2886$;

The plate is clamped at $Y = 0$ and a force ($F_z = -1N$) is applied in the point of coordinate [b/2;L;0].

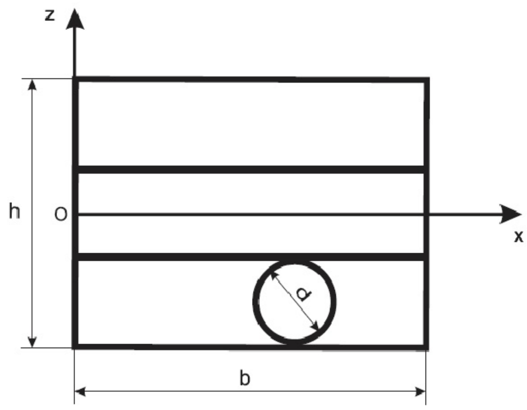

Figure 3.56: Geometry of laminated plate

3.14.1 Model 1

The first model consist in a simple analysis of beam by three layers of orthotropic material (Fig 3.57). For the analysis are used $40 - B4$ elements for Taylor-like expansion, $5 - B4$ elements for Lagrange expansion and 20 nodes brick for solid analysis by abaqus.

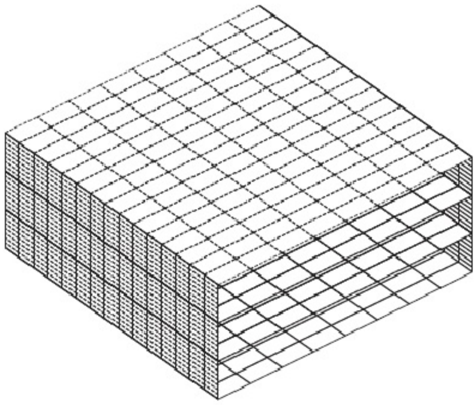

Figure 3.57: Representation of model 1

3.14.2 Model 2

The second model used for the analysis consist in a two layers of orthotropic material and the last layer is the combination of fibers and matrix (Fig 3.58). For the discretization a 20 node brick is used and the analysis is calculated by abaqus software.

3.14.3 Model 3

The third model consist in a one central layer of orthotropic material and the remaining two layers are composed by fibers and matrix (Fig 3.59). For the discretization a 20 node brick is used and the analysis is calculated by abaqus software.

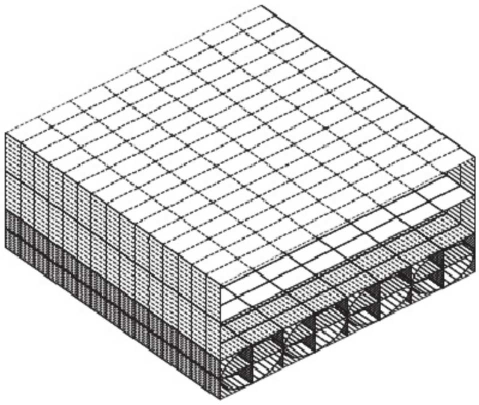

Figure 3.58: Representation of model 2

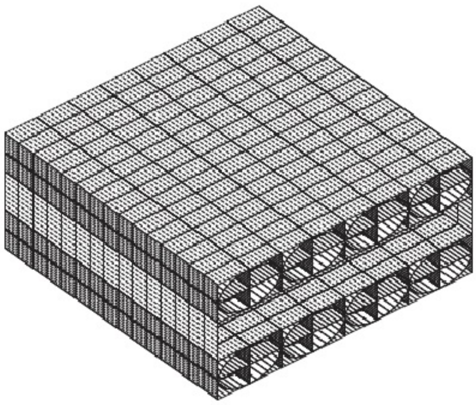

Figure 3.59: Representation of model 3

3.14.4 Model 4

The third model consist in a two layers of orthotropic material and the last one are composed by one fiber and the remaining part of orthotropic materia (Fig 3.60). For the discretization a 20 node brick is used and the analysis is calculated by abaqus software.

3.14.5 Results

In the Fig 3.61 is shown, for model 1, the trend of σ_{yy} along the Z axis and coordinate $X = 0.3$ and $Y = 0$, while in the table 3.26 are summarized and compared[14] the

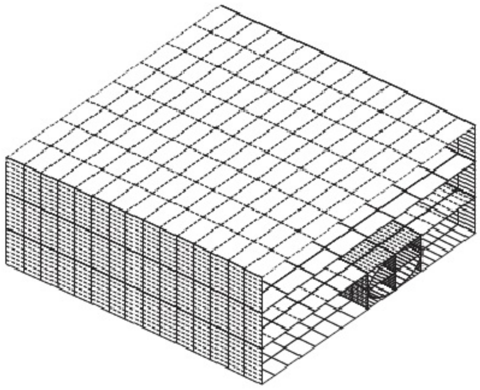

Figure 3.60: Representation of model 4

results. Instead, in the table 3.27 are summarized the result of the solid analysis of the remaining models.

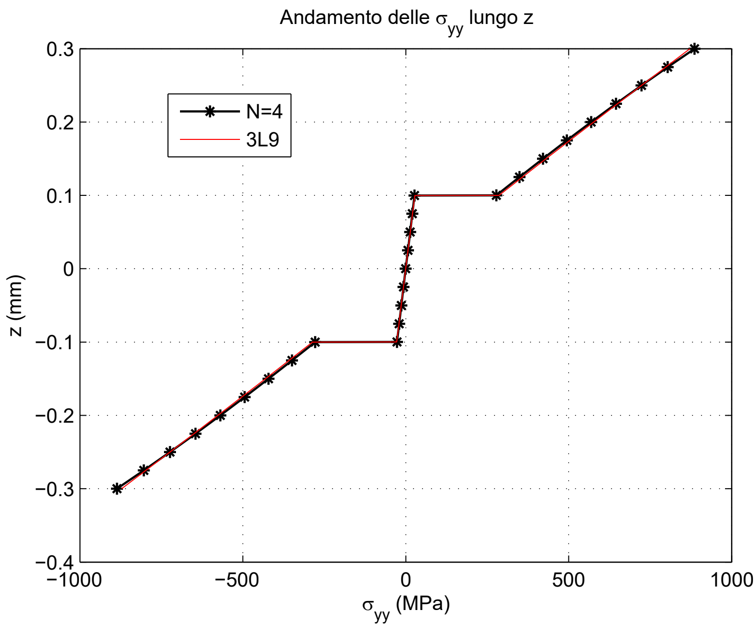

Figure 3.61: σ_{yy} trend along Z axis evaluated with model 1

Table 3.26: Deflection and stresses of model 1.

Model	$u_z \times [mm]$ [b/2,L,0]	$\sigma_{yy} \times 10^{-2}[MPa]$ [0.5,0,-0.2]	$\sigma_{xy} \times [MPa]$ [0.55,0,-0.2]	DOFs
Reference[14]				
N=4	-9.63	-5.71	-	5445
3L9	-9.63	-5.76	3.63	1008
Model 1				
N=4	-9.63	-5.69	-	5445
3L9	-9.63	-5.77	3.57	1008
SOLID	-9.64	-5.74	2.96	3129

Table 3.27: Deflection and stresses of model 2,3 and 4.

Model	$u_z \times [mm]$ [b/2,L,0]	$\sigma_{yy} \times 10^{-2}[MPa]$ [0.5,0,-0.2]	$\sigma_{xy} \times [MPa]$ [0.55,0,-0.2]	DOFs
Model 2				
SOLID	-9.73	-7.32	1.42	23031
Model 3				
SOLID	-9.90	-7.41	1.04	196623
Model 4				
SOLID	-9.66	-7.28	1.32	174888

Chapter 4

Micromechanics

Given that the complex structure of composite materials and the very small diameter of the fibers ($6\mu m$), the failure analysis requests a multiscale approach. As shown in Fig 4.1 [10], the analysis, starting from a big and complex structure, as an airplane, switches over to a laminates and, lastly, it cames to analyze a microstructure composed by a few fibers: it is like a loop because there is a constant exchange of information between the macro and micro scale. For this reason the microscale and consequently the micromechanics are essential for structure failure analysis.
In this work thesis the micromechanics is used for the matrix failure analysis using a code based on Carrera unified formulation (CUF).

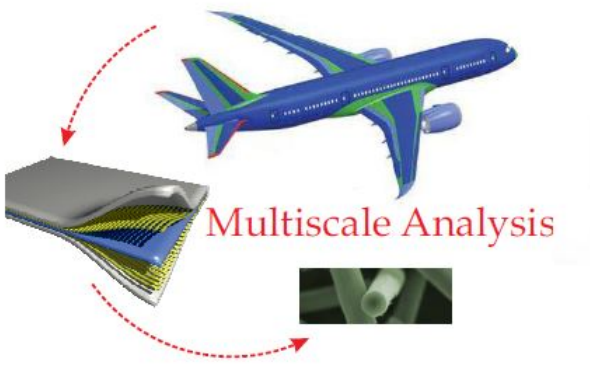

Figure 4.1: Multiscale analysis

4.1 Repeated unit cell (RUC)

The fibers, in a real structure made by composite materials, can be ordered only along one direction while on the cross-section they cannot have a hated arrangement: this happens because during the production process it is impossible to control the transverse placement of the single fiber when fibers and matrix are mixed. So the cross-section fibers arrangement is unknown, but the distance between the fibers influences the stresses distribution which defines the crack initiation. To overcome the problem and find a solution to the failure problem, it is required the micromechanics plus a simplified model and a statistical analysis. The problem could be simplified assuming the existence of a repeating cell in the structure called RUC (Fig 4.2 [10]): it is a rectangular parallelepiped with a square sections and dimension ratio $L/h = 10$, so the macrostructure can be seen as composed by a periodic array of simple cells (RUC). The microscale failure analysis is performed on different RUCs type composed by the same number of the fibers but different arrangement and the final result is evaluated statistically taking account of all the RUCs results. For these reasons the necessary parameters to describe the RUC are:

- The number of the fibers N_f;
- Fiber diameter ϕ_f and dimension ratio $\frac{L}{h}$;
- Volume Fraction=$V_f = \frac{RUC\ Fibers\ volume}{Total\ RUC\ volume}$;

Where "h" is the length of the square RUC cross-section and "L" is the transverse RUC dimension as shown the Fig. 4.2 [10]. All the others parameters, except the fiber centers, can be obtained as combination of the main parameters.

For the matrix failure analysis, have been created 10 different RUCs composed by 5 fibers and random arrangement of fiber (Fig 4.3 [15]). They have the following geometric properties:

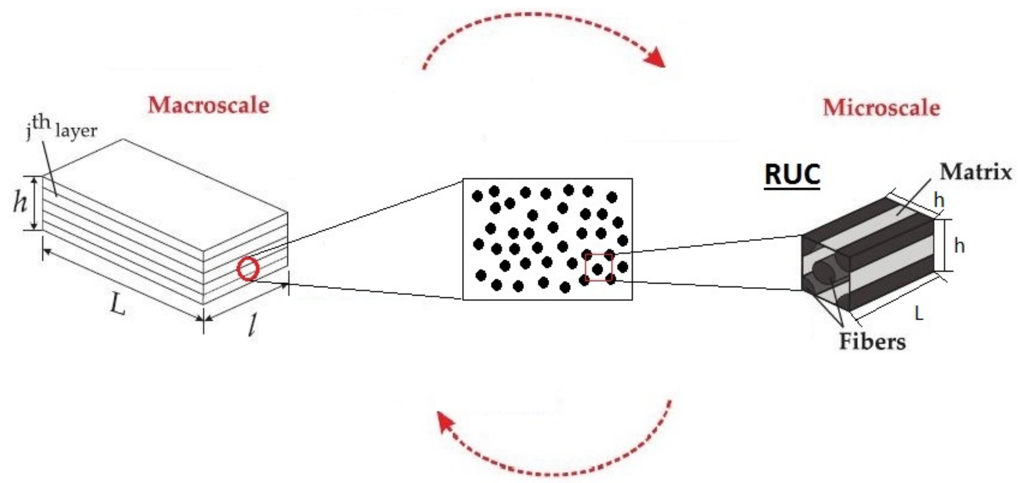

Figure 4.2: Repeated unit cell (RUC)

- Fiber diameter $\phi_f = 6\mu m$;
- Fiber volume fraction $V_f = 0.52$
- $\frac{L}{h} = 10$

Every RUC has a square cross-section, so it is simple to evaluate the dimension of the cell (L and h) from the previous data. The definition of volume fraction is:

$$V_f = \frac{v_f}{v_R UC} \tag{4.1}$$

The unknown is $v_R UC$ because the fibers volume is simply calculable as:

$$v_f = (\pi r_f)^2 \times N_f \times L = L \times 141.372\mu m^2 \tag{4.2}$$

Where N_f is the total fibers number (5). Now it is possible to calculate "h" by the relation:

$$v_{RUC} = h^2 \times L = \frac{v_f}{V_f} = L \times \frac{141.372\mu m^2}{0.52} \tag{4.3}$$

Definitely $h = 16.49\mu m$ while the "L" is evaluated by the dimension ratio $L/h = 10$, so it is equal to $L = 164.9\mu m$.

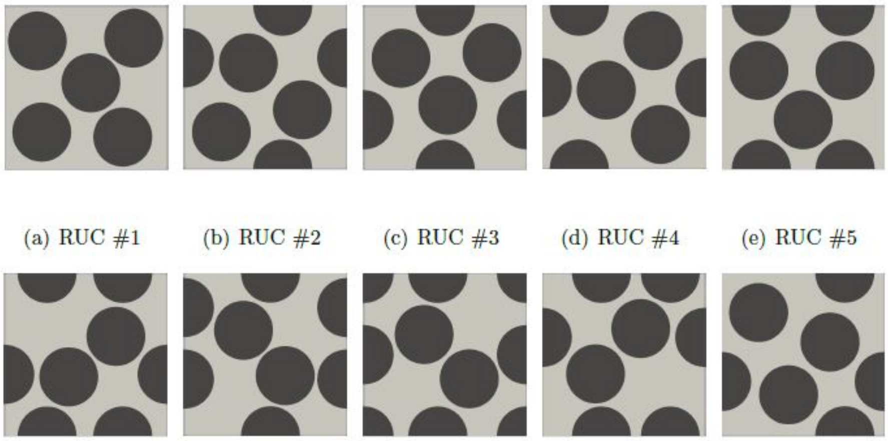

(a) RUC #1 (b) RUC #2 (c) RUC #3 (d) RUC #4 (e) RUC #5

(f) RUC #6 (g) RUC #7 (h) RUC #8 (i) RUC #9 (j) RUC #10

Figure 4.3: Cross-section representation of five RUCs fibers

4.2 Periodic boundary conditions (PBC)

In order to ensure the continuity between two consecutive RUCs, periodic boundary conditions (PBC) are necessary for microscale analysis. The PBC shall ensure that all the RUCs of the structure have the same deformation mode because when the deformation starts there must be no gaps or overlaps between them. In terms of displacements (u,v,w), the boundary nodes of each RUC are constrained by the following equations systems [10]:

$$\textbf{Side1} = \begin{cases} u(l_1, y, z) - u(0, y, z) = \epsilon_{11} l_1 \\ v(l_1, y, z) - v(0, y, z) = 2\epsilon_{12} l_1 \\ w(l_1, y, z) - w(0, y, z) = 2\epsilon_{13} l_1 \end{cases} \tag{4.4}$$

$$Side2 : \begin{cases} u(x, l_2, z) - u(0, y, z) = 2\epsilon_{21} l_2 \\ v(x, l_2, z) - v(0, y, z) = \epsilon_{22} l_2 \\ w(x, l_2, z) - w(0, y, z) = 2\epsilon_{23} l_2 \end{cases} \tag{4.5}$$

$$Side3: \begin{cases} u(x,y,l_3) - u(x,y,0) = 2\epsilon_{31}l_3 \\ v(x,y,l_3) - v(x,y,0) = 2\epsilon_{32}l_3 \\ w(x,y,l_3) - w(x,y,0) = \epsilon_{33}l_3 \end{cases} \quad (4.6)$$

Where sides 1, 2 and 3 are referred to the pairs of cell faces and l_1, l_2 and l_3 are the cell dimension along the x,y and z axes directions (Fig 4.4). In other words, the cell faces belonging to the same "side" deform in the same way, indeed the PBC must be applied at all the node boundary nodes.

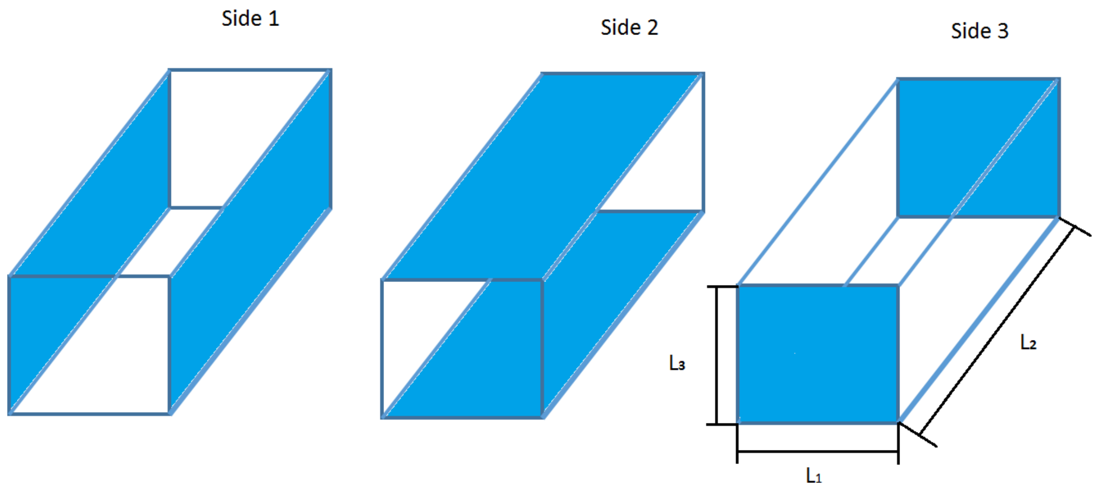

Figure 4.4: BPC sides representation

To clarify the concept, a simple example is now presented (Fig 4.5) [10] , the RUC is represented by only one L9 element on the cross-section and one beam element with three nodes along the beam axis. The PBC are the following:

- PBC of the "side 1" are applied on the nodes i=3,4,5 and j=1,8,7 (regardless of the apex);
- PBC of the "side 2" are applied on the nodes i=5,6,7 and j=3,2,1 (regardless of the apex);
- PBC of the "side 3" are applied on the nodes i=1"',...,9"' and j=1',...,9';

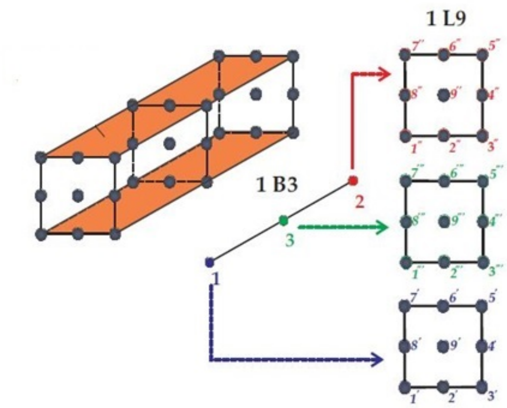

Figure 4.5: Example representation

4.3 Progressive failure analysis of matrix

The failure analysis is an iterative process that solves a linear system equations at each iteration, where the linear system is the typical of the FEM (4.7). The code is based on the "crack band theory for fracture of concrete" [16] that it is not a main topic of this work thesis, for this reason only a reference to the theory will be given.

$$[k]\{U\} = \{F\} \tag{4.7}$$

Since the analysis purpose is the studies of the microcracks effect in the matrix and it is classified as a monolithic material, only the opening mode shown in the Fig. 4.6 [10] is considered for the progressive failure analysis. The crack band theory assumes that the opening direction is a function of the maximum principal stress.

The failure criteria is the maximum strain, it is used to define the failure initiation, and the analysis is strain controlled. The Fig. 4.7 [10] shows how it is conducted the analysis, the RUC is fixed on the left at the coordinate $x = x_0$ while on the other face it is applied a strain Δx because it is strain controlled. At each iteration are evaluated displacement, stress and strain fields in all the domain

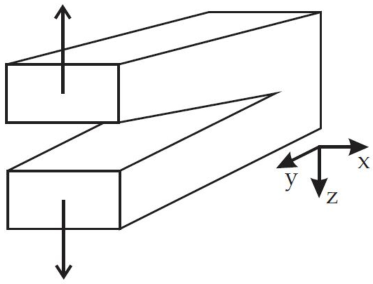

Figure 4.6: Opening mode representation

nodes and if on a L9 cross-section element the value of the strain exceeds the limit value assigned (failure strain ϵ_f), it breaks and the stiffness matrix is penalized. The analysis ends when the RUC is broken in two parts. The Fig. 4.7 [10] shows the typical stress-strain curve for the fracture process, where the stress and strain are calculated as the average values on the right RUC face. Before the peak, a linear elastic behaviour is assumed for the material, when the maximum value of the strain is reached, that is the peak, the curve stops growing and begins to decrease until complete rupture of the cell. The post-peak behaviour describes the progressive strain-softening or rather the decrease of stress at strain increasing [10] while the area under the curve represents all the energy consumed in formation and propagation of the crack in the material, the value of this kind of energy is fixed for all the failure analysis.

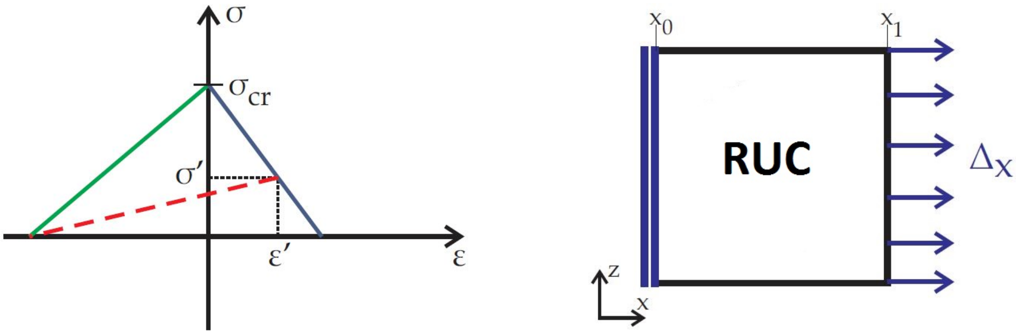

Figure 4.7: Stress-strain diagram for the fracture process (left) and RUC progressive failure analysis (right)

Chapter 5

Results of progressive failure analysis of matrix

This chapter contains all the results of matrix failure analysis, starting from a simple case with only one L9 element on the cross-section, to arrive at the failure analysis of the RUCs with five fibers. The cross-section meshes has been created by abaqus, the main problem was that the abaqus rectangular elements are composed by 8 nodes and the connectivity of elements is ordered differently (Fig. 5.1). A matlab code is used to add the central node and modify the elements connectivity, the central node coordinates (x;z) are evaluated in the following way:

$$\begin{cases} x = \frac{X_5+X_6+X_7+X_8}{4} \\ y = \frac{Y_5+Y_6+Y_7+Y_8}{4} \end{cases} \tag{5.1}$$

They are the average value of the four lateral nodes of the abaqus rectangular element. As stated above, the progressive failure analysis is performed by a code based on Carrera unified formulation and the Crack band theory [16], analyzes only one between all the composite failure modes, the matrix failure. The analysis method has already been described in the previous chapter. It is important to specify that in all the successive analysis only one beam element composed by 3 nodes will be use along the beam axis.

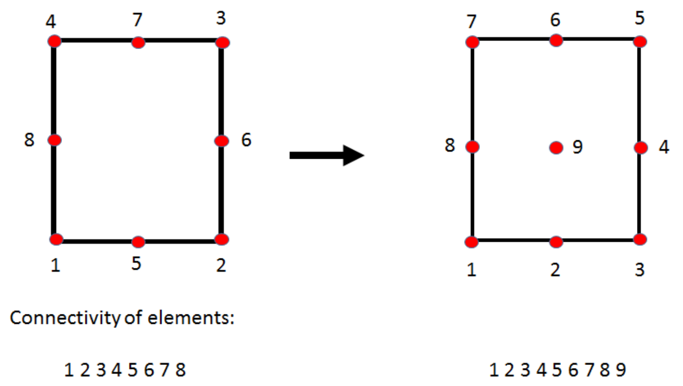

Figure 5.1: Abaqus rectangular element v.s. L9 element

5.1 Homogeneous block

In this section an homogeneous block is analyzed with different material properties and different discretiation of the cross-section, with the scope to show the code operation. The geometrical characteristics of the block are fixed for all the next analysis and they are: $l_1 = l_3 = 0.001mm$ and the transversal dimension is $l_2 = 0.01mm$ (Fig 5.2).

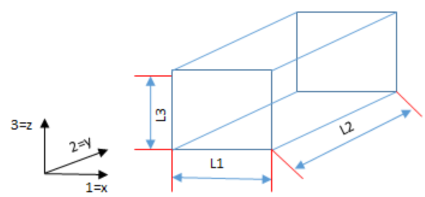

Figure 5.2: Representation of the homogeneous block dimensions

For the last two cases (9 and 25 L9 elements), in order to induce the crack formation in the center of the block and the propagation in vertical direction, a different values of failure stress are assigned at the L9 elements.

5.1.1 One L9 element on the cross-section

The first case analyzed is an homogeneous block discretized with only one L9 element, this example can help the lectors to achieve a better understanding of the failure criteria and generally the code operation. It is the simplest possible case because uses for discretization only one L9 element on the cross-section and one beam element with three nodes along the beam axes. The block is fixed on the left surface while a strain "Δx" is applied on the opposite face at each iteration (Fig. 5.3), for the analysis an isotropic material with the following properties is used:

- Young modulus E= 127600 MPa;
- Poisson ratio ν=0.3;
- Failure stress $\sigma_x = \sigma_y = \sigma_z = 1730$ MPa;

While the parameters setting of analysis is:

- Number of increments $N = 250$;
- Delta increment pulling $\Delta x = 1.0 \times 10^{-4}$;
- Degree of freedom number $NDOFs = 81$;

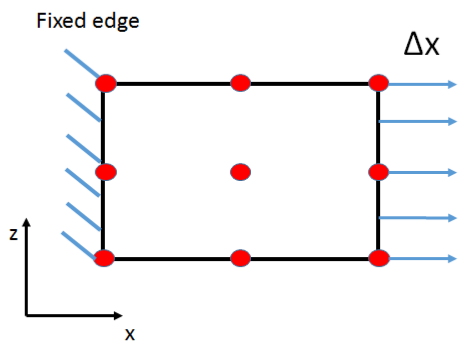

Figure 5.3: Failure analysis representation of one L9 element

The Fig. 5.4 shows the stress strain curve. The material has a linear elastic behavior until the peak, in the peak the strain achieves the critical value which leads to the breaking of the element. The critical value of stress and strain in the peak are the following:

$$\begin{cases} \sigma_{xfailure} = 2318.26MPa \\ \epsilon_{xfailure} = 0.0135 \end{cases} \tag{5.2}$$

It is possible to realize by the graphics that for value of strain around the $\epsilon = 0.019$ the block is completely crushed.

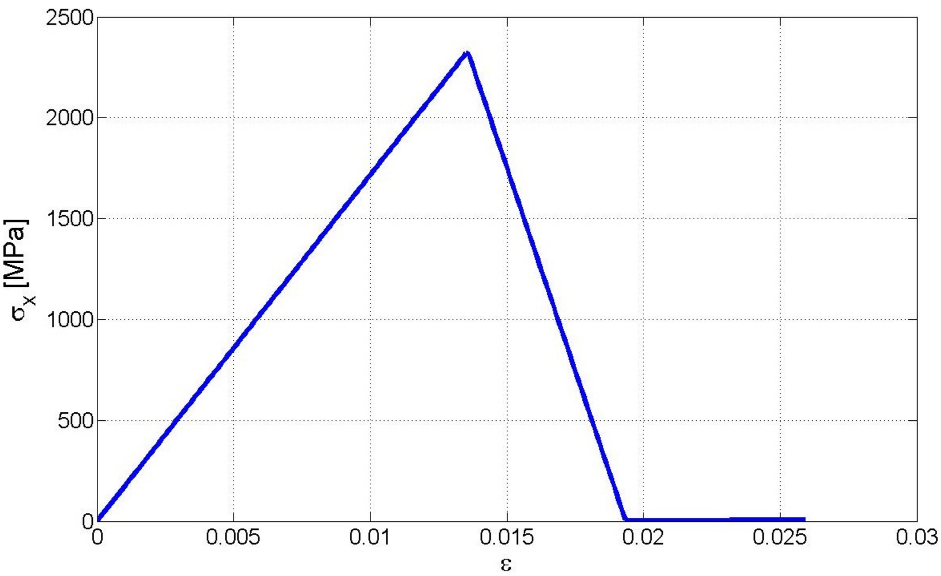

Figure 5.4: Stress-strain curve of one L9 element case

5.1.2 Nine L9 elements on the cross-section

Now the cross-section of homogeneous block is meshed by nine L9 elements while along the beam axes only one beam element with three nodes is used, nine is the minimum number of element necessary to create a failure zone in the center of the block and to force the failure to start in the center (Fig. 5.5[10]). The failure zone is located at the center of the block and it has a thickness t=0.0001 mm while the other dimension are the same of the block and in order to force the failure in the center a different values of failure stress are assigned at different element in order to induce the crack formation in the center. The material properties are:

- Young modulus E=3252 MPa
- Poisson ratio $\nu = 0.355$
- Failure stresses:$\sigma_{f1} = 27.5MPa$, $\sigma_{f2} = 29.5MPa$ and $\sigma_{f3} = 66.5MPa$

The Fig. 5.5 shows the cross-section discretizzation and the failure stress assignment, the numbers in the figure are related to the failure stresses σ_f. The failure is induced to start in the central element because it has the lower value of failure stress $\sigma_{f1} = 27.5MPa$ (Fig. 5.5[10]) and later it is forced to propagate within the upper and lower elements because the failure stress ($\sigma_{f2} = 29.5MPa$) is lower than the remaining elements. The parameters setting of the failure analysis is:

- Number of increments $N = 250$;
- Delta increment pulling $\Delta x = 1.0 \times 10^{-3}$;
- Degree of freedom number $NDOFs = 441$;

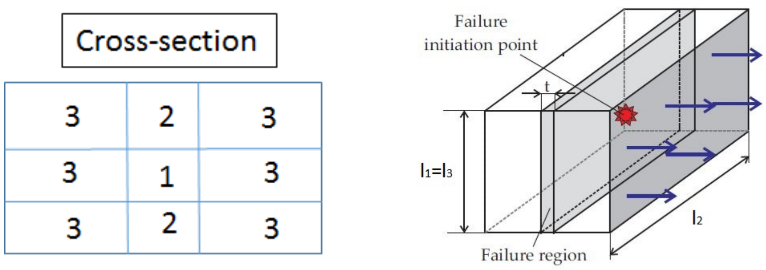

Figure 5.5: Cross-section material assignment(left) and failure initiation point representation(right)

The failure analysis result are shown in the Fig. 5.6, the stress-strain curve has a linear elastic behavior until the first element failure. In this case the failure of the one element does not imply the collapse of the whole block, indeed the peak is after the failure of the central element. The critical value of stress and strain in the peak are the following:

$$\begin{cases} \sigma_{xfailure} = 82.91MPa \\ \epsilon_{xfailure} = 0.02 \end{cases} \tag{5.3}$$

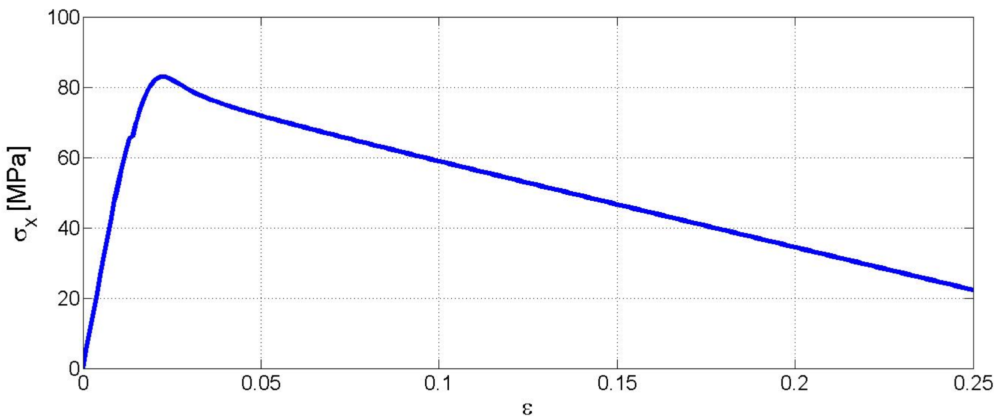

Figure 5.6: Stress-strain curve of nine L9 elements case

5.1.3 Twenty five L9 elements on the cross-section

The last case of failure analysis of homogeneous block is identical to the previous except for the cross-section discretizzation, indeed 25 element are now used so the propagation zone of the failure is now composed by four L9 elements while in the previous case there were only two. Due to the increase of the cross-section elements also the NDOFs rose significantly, in fact now it is $NDOFs = 1089$. The Fig. 5.7 shows the cross-section discretizzation and the failure stress assignment, the numbers in the figure are related to the failure stresses σ_f so the failure is forced to start in the center.

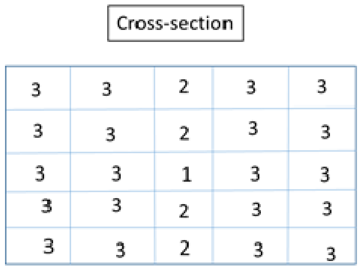

Figure 5.7: Cross-section material assignment of 25 L9 elements case

The failure analysis result are shown in the Fig. 5.8, the curve trend is similar but not identical to the previous case because the NDOFs is changed. The critical value of stress and strain in the peak are the following:

$$\begin{cases} \sigma_{xfailure} = 86.63MPa \\ \epsilon_{xfailure} = 0.02 \end{cases} \tag{5.4}$$

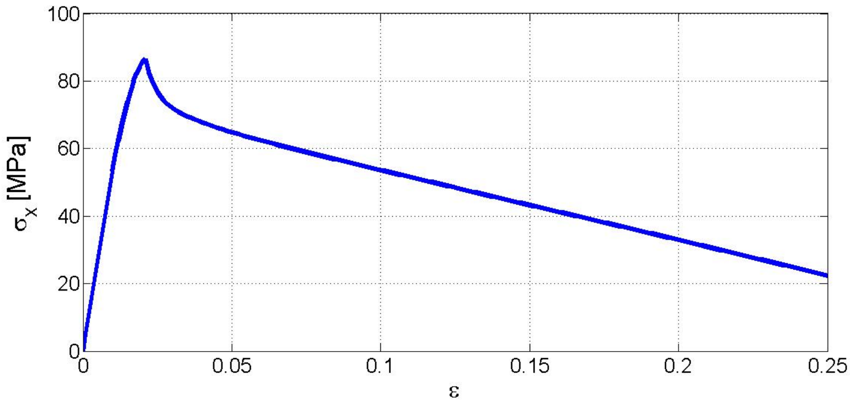

Figure 5.8: Stress-strain curve of twenty five L9 elements case

In the Fig. 5.9 are compared the two solution. The stress σ in the peaks are different, 86.63 MPa versus 82.91 MPa, but the value of the strain is the same

$\epsilon_{xfailure} = 0.02$.

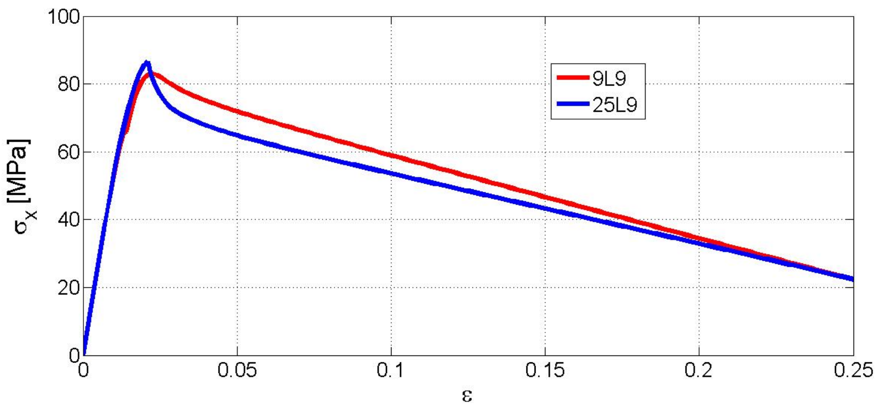

Figure 5.9: Comparison of stress-strain curve between 9 and 25 L9 element cases

5.2 Single fiber

Now a cell composed by one fiber in the center is analyzed, the cross-section and the cell dimensions are shown in the Fig. 5.10. Cell geometric properties are:

- Cross-section dimension $l_1 = l_3 = 0.008mm$;
- Transversal dimension $l_2 = 0.08mm$;
- Fiber diameter $\phi = 6\mu m$;

The two materials, used for the matrix and fiber, are isotropic material with a failure stresses assigned along the three principal directions, their properties are summarized in the table 5.1. The Fig. 5.10 represents the cross-section meshing, twenty L9 elements are used for cross-section discretization of which 12 only for the fiber while along the beam axes the usual 3-node beam element is used. The analysis operation is the same of the previous cases and the parameters setting is the following:

- Number of increments N=200;
- Delta increments pulling $\Delta x = 3.0 \times 10^{-5}$
- Degree of freedom number NDOFs= 801;

The result in terms of stress-strain curve is shown in the Fig. 5.11. The critical value of stress and strain in the peak are the following:

$$\begin{cases} \sigma_{xfailure} = 97.30MPa \\ \epsilon_{xfailure} = 0.00667 \end{cases} \tag{5.5}$$

As in the previous cases, the curve trend is linear until the peak and after it collapses due to the brittle behavior of the matrix material.

Table 5.1: Materials properties

	Matrix	Fiber
Yang modulus E	3252 MPa	250634 MPa
Poisson ratio ν	0.355	0.2456
$\sigma_{xfailure}$	3398.1 MPa	66.5 MPa
$\sigma_{yfailure}$	2052.6 MPa	255 MPa
$\sigma_{zfailure}$	186.8 MPa	74.0 MPa

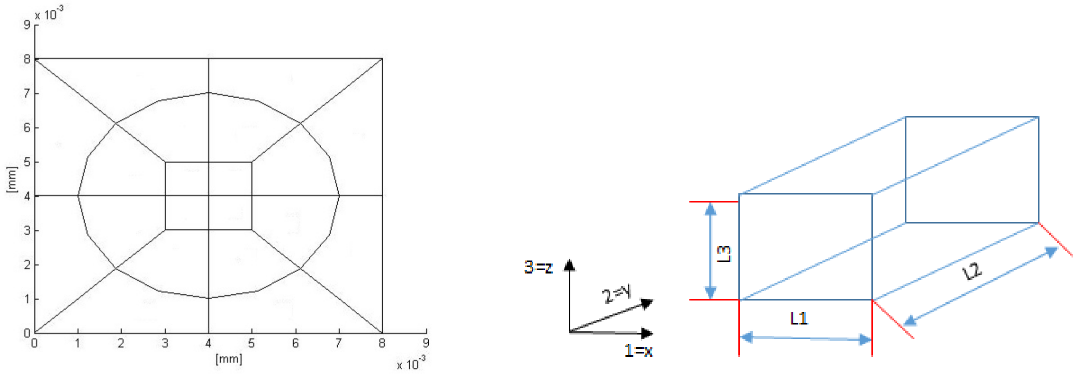

Figure 5.10: Representation of cross-section discretization (left) and representation of cell dimensions (right)

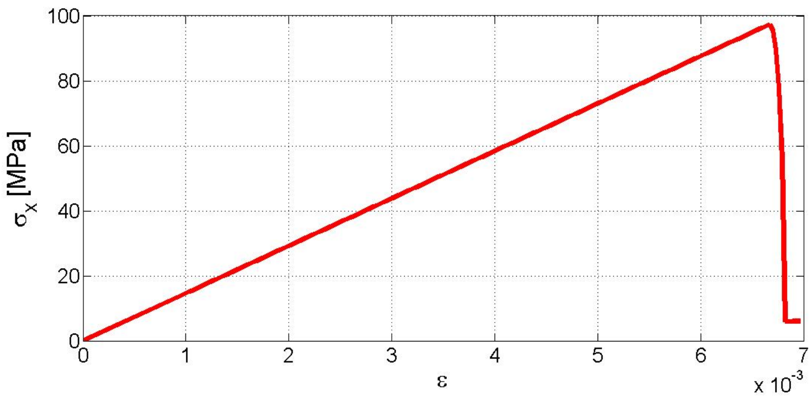

Figure 5.11: Stress-strain curve of one fiber

5.3 Random packed

Lastly, random packed RUCs with five fibers are analyzed. All their cross-section were meshed with the help of the abaqus automatic meshing, but despite the implementation of PARDISO library in the code to reduce the computational time and improve the management of the memory, the analysis requires equally large amount of virtual memory. For this reason the number of L9 elements and nodes on the cross-section is restricted and beyond a limit, the code gives insufficient virtual memory error. Indeed the analysis of the RUC#1, with the cross-section fibers distribution shown in the Fig. 5.13, did not work because the number of the cross-section nodes is greater than all the other cases. The geometrical characteristic of the RUCs are the following:

- Cross section dimension $l_1 = l_3 = 16.5\mu m$ (Fig. 5.12);
- Transversal length $l_2 = 165\mu m$ (Fig. 5.12);
- Fiber diameter $\phi_f = 6\mu m$;
- Fiber volume fraction $V_f = \frac{v_f}{v_total}$

The materials properties used for fibers and matrix are the same of the single fiber case and are summarized in the table 5.1.The Fig. 5.12 [10] shows the analysis operation, as in the previous cases, the left side is fixed while on the opposite one is applied an increment Δx. All the RUCs cross-section with the respective crack propagation are shown in the Fig. 5.14, 5.16, 5.18, 5.20, 5.22, 5.24, 5.26, 5.28 and 5.30, while all the information about every RUCs analysis and the maximum value achieved of stress and strain are summarized in the tables 5.2 and 5.3 where:

- $N_{elements}$ is the number of L9 elements on the cross-section;
- N_{points}in the number of cross-section nodes;

- NDOFs is the total number of degree of freedom;
- $N_{increments}$ is the total number of increments for the analysis;
- Δx represents the quantity of the each increment;
- $\sigma_{xfailure}$ is the maximum value of the stress achieved during the analysis;
- $\epsilon_{xfailure}$ is the maximum value of the strain achieved during the analysis;

The Fig. 5.15, 5.17, 5.19, 5.21, 5.23, 5.25, 5.27, 5.29, 5.31 show all the results in terms of stress-strain curve; during the pulling, a stress concentrations can arise on the cross-section especially in the zones between two close fibers. So any elements can fail early but this does not involve the total collapse of the structure and furthermore it is the reason of curves broken trends.

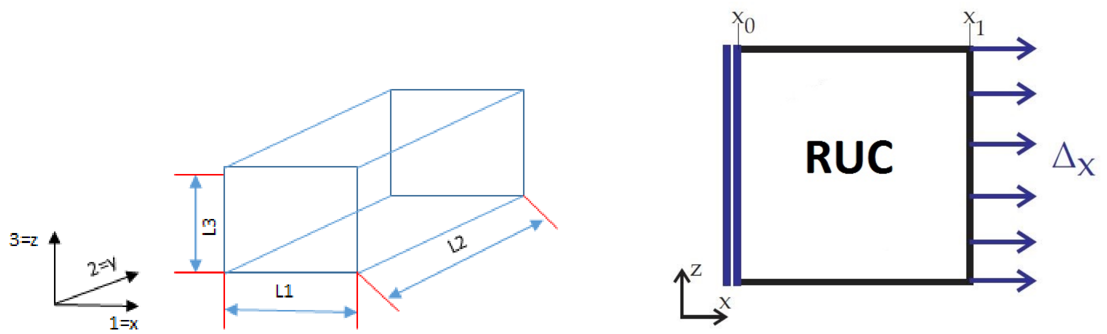

Figure 5.12: RUC dimensions (left) and RUC analysis representation (right)

Table 5.2: Results

	RUC #1	RUC #2	RUC #3	RUC #4	RUC #5
$N_{elememnts}$	204	107	120	120	123
N_{points}	857	463	517	515	527
NDOFs	7713	4167	4653	4635	4743
$N_{increments}$	-	250	180	260	250
$\Delta x \times 10^{-5}$	-	4.4	4.4	4.4	2.8
$\sigma_{xfailure}[MPa]$	-	59.193	61.711	64.711	740597
$\epsilon_{xfailure}$	-	0.00412	0.00386	0.00522	0.00528

Table 5.3: Results

	RUC #6	RUC #7	RUC #8	RUC #9	RUC #10
$N_{elememnts}$	104	143	89	103	106
N_{points}	453	611	395	453	459
NDOFs	4077	5499	3555	4077	4131
$N_{increments}$	200	175	120	160	300
$\Delta x \times 10^{-5}$	4.4	4.4	6.4	4.4	2.4
$\sigma_{xfailure}[MPa]$	55.752	54.874	68.784	63.064	62.739
$\epsilon_{xfailure}$	0.00430	0.00514	0.00561	0.00514	0.00549

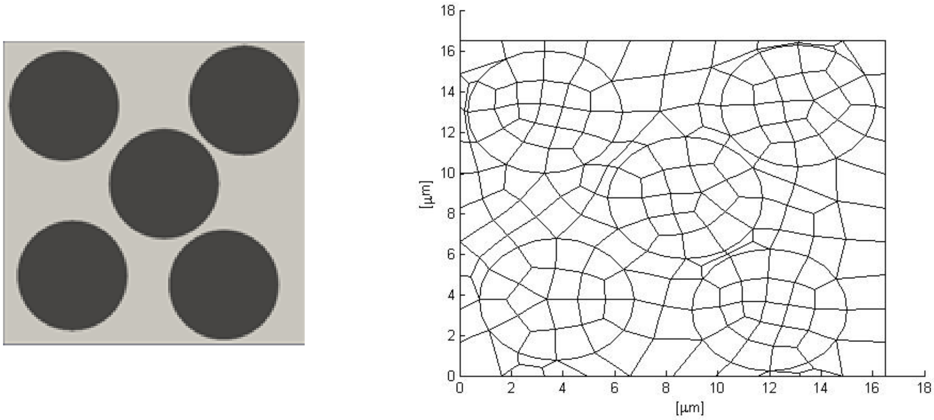

Figure 5.13: RUC#1 cross-section representation (left) and RUC#1 meshing representation (right)

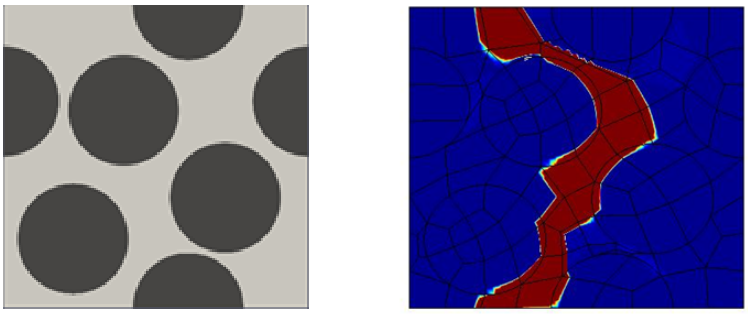

Figure 5.14: RUC#2 cross-section representation (left) and RUC#2 crack-path (right)

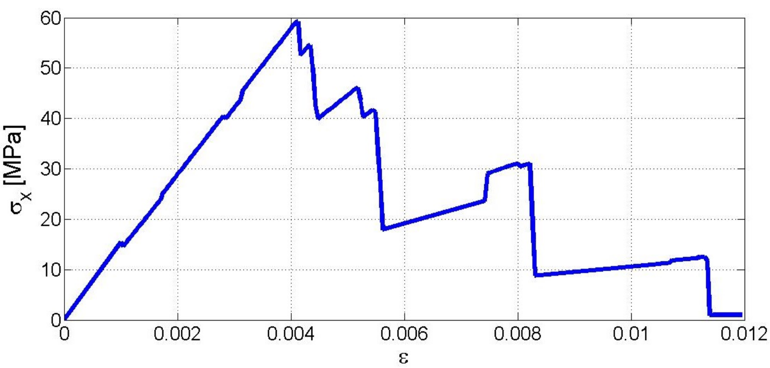

Figure 5.15: Stress-strain curve of RUC #2

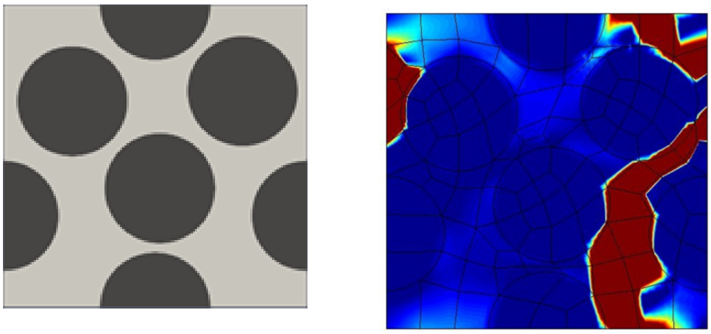

Figure 5.16: RUC#3 cross-section representation (left) and RUC#3 crack-path (right)

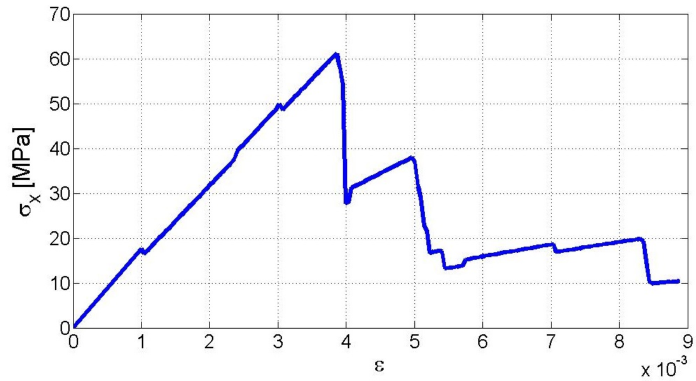

Figure 5.17: Stress-strain curve of RUC #3

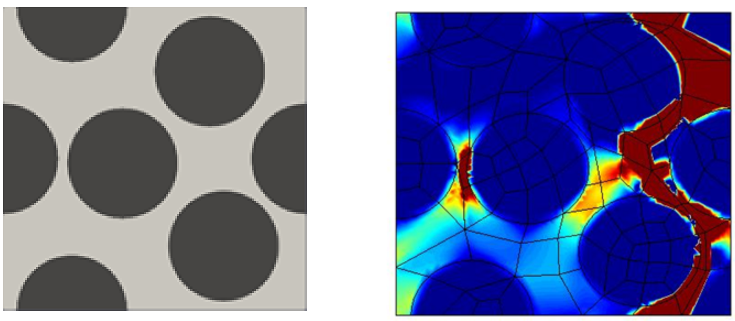

Figure 5.18: RUC#4 cross-section representation (left) and RUC#4 crack-path (right)

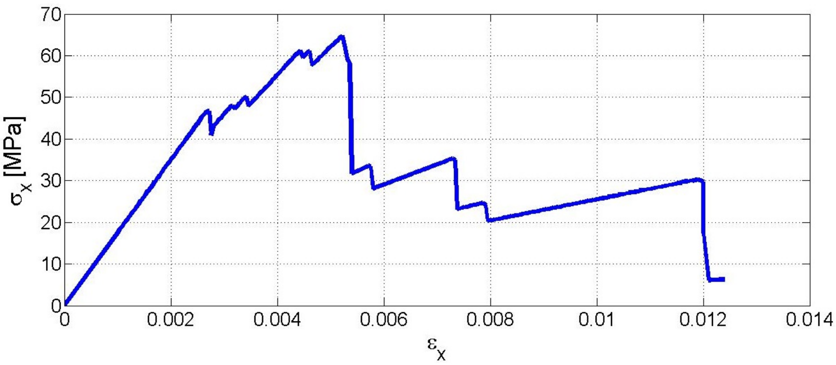

Figure 5.19: Stress-strain curve of RUC #4

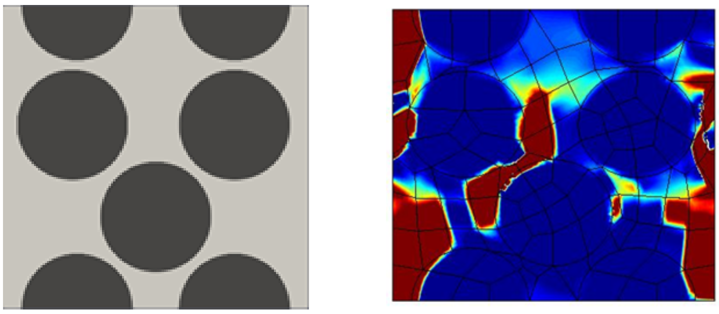

Figure 5.20: RUC#5 cross-section representation (left) and RUC#5 crack-path (right)

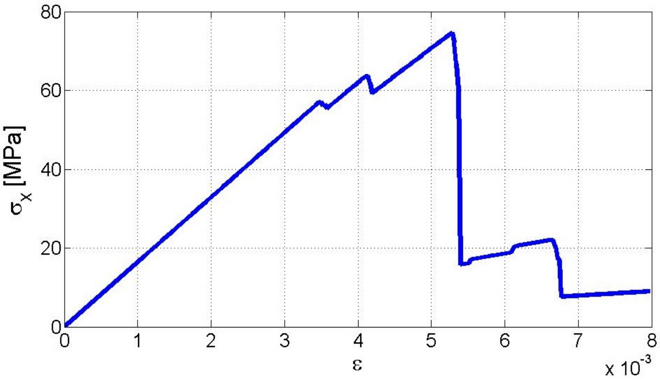

Figure 5.21: Stress-strain curve of RUC #5

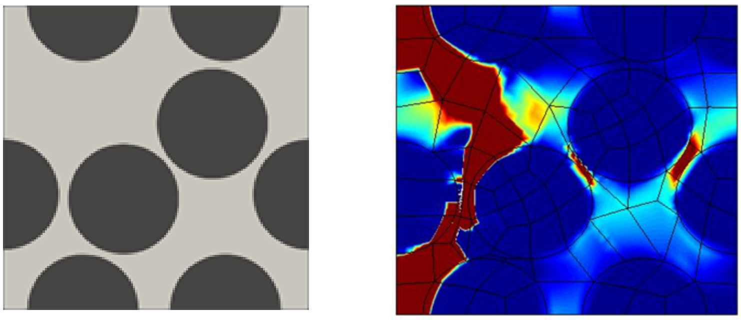

Figure 5.22: RUC#6 cross-section representation (left) and RUC#6 meshing representation (right)

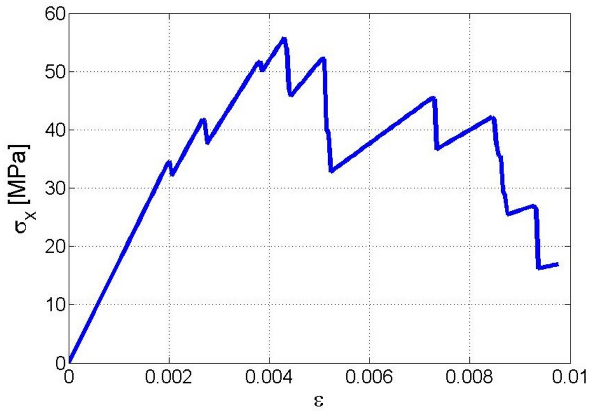

Figure 5.23: Stress-strain curve of RUC #6

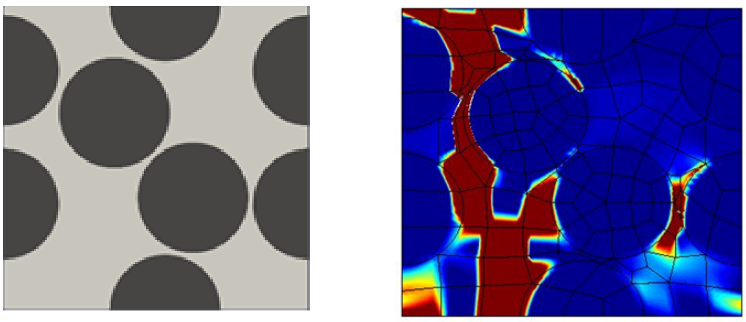

Figure 5.24: RUC#7 cross-section representation (left) and RUC#7 crack-path (right)

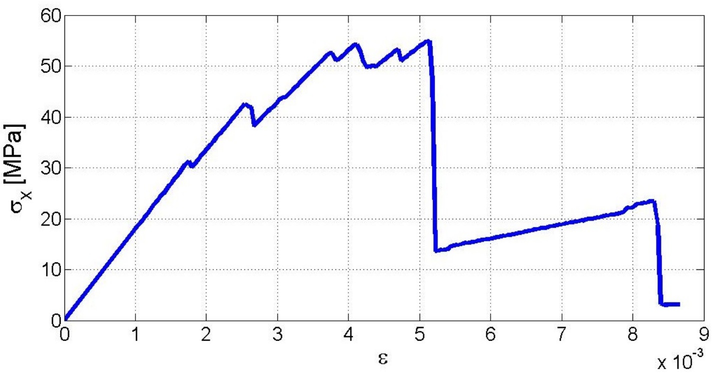

Figure 5.25: Stress-strain curve of RUC #7

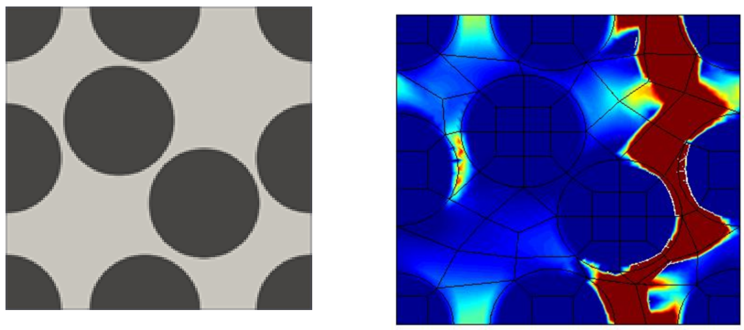

Figure 5.26: RUC#8 cross-section representation (left) and RUC#8 crack-path (right)

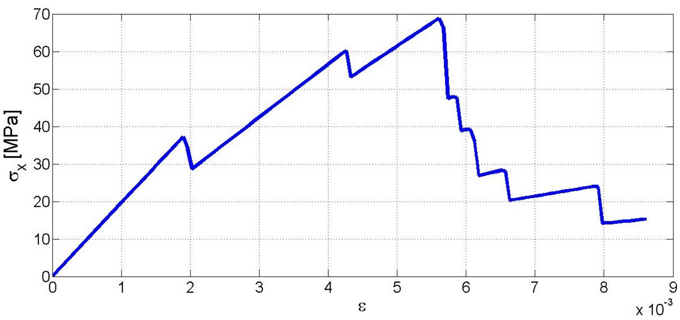

Figure 5.27: Stress-strain curve of RUC #8

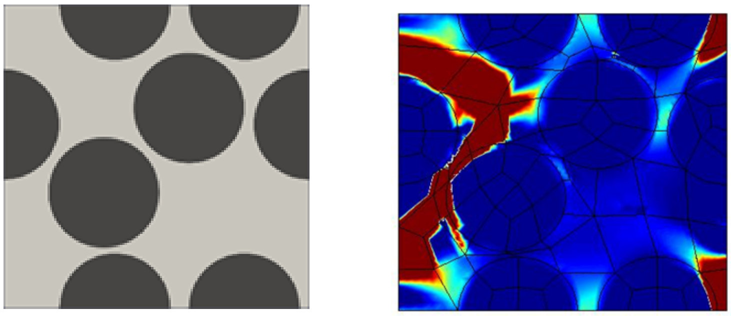

Figure 5.28: RUC#9 cross-section representation (left) and RUC#9 crack-path (right)

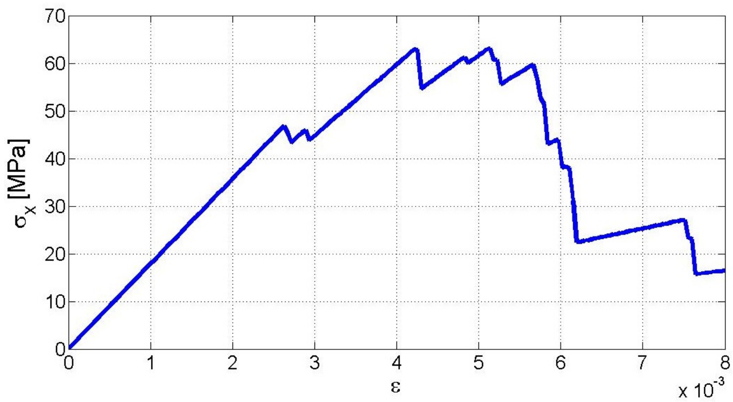

Figure 5.29: Stress-strain curve of RUC #9

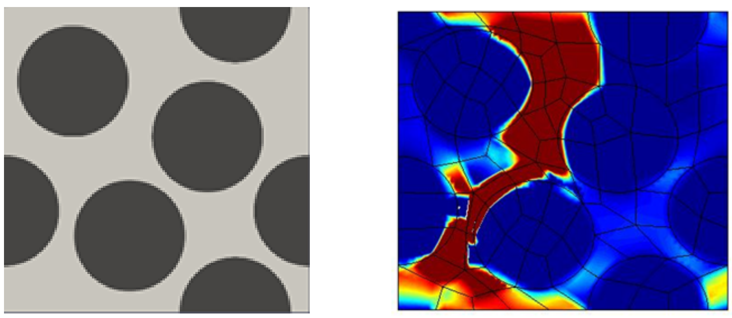

Figure 5.30: RUC#10 cross-section representation (left) and RUC#10 crack-path (right)

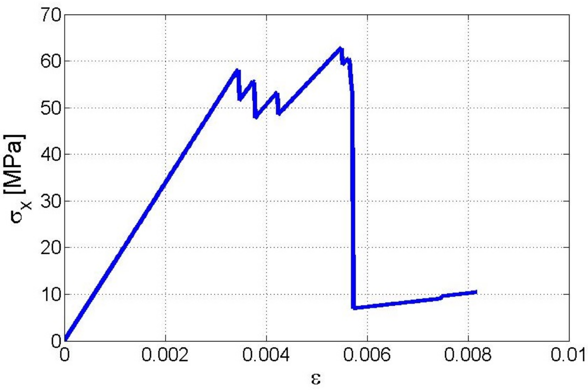

Figure 5.31: Stress-strain curve of RUC #10

Chapter 6

Conclusions

The PARDISO library implementation has allowed to reduce the analysis time and to obtain the results in around eighteen minutes. Nevertheless the virtual memory required for the analysis is still a lot, therefore the number of points used to describe the cross-section was limited. Given that the arrangement of the fiber over the cross-section was unknown, the results obtained in the previous chapter, about the RUCs matrix failure, have been used to obtain an average values of stress and strain. This was possible because the results showed that the maximum values of stresses and their respective strains did not differ significantly. The average values are $\sigma_{avegage} = 56.185MPa$ and $\epsilon_{average} = 0.00445$. Moreover, the generical stress-strain curve could also be extracted by a statistical average of all the curves obtained previously, and it represents the typical trend of a general RUC matrix failure. The order of magnitude of these values is reasonable, but a further work of validation should be done. Given that the computational cost is very low, the next step could be the implementation of this method in a software for multi-scale analysis.

Bibliography

[1] *url : https : //it.wikipedia.org/wiki/materiale_composito.*

[2] *url : http : //digital.library.okstate.edu/oas/oas_htm_files/v56/p104_107nf.html.*

[3] Brando Tuberosa. *Proprietà meccaniche a trazione di compositi pomerici rinforzati con fibre lunghe di carbonio di interresse per il settore automotive.* Tesi di laurea, Università di Bologna, 2012.

[4] Url:https://leehamnews.com/2014/04/15/odds-and-ends-composites-in-future-airplanes-boeing-and-hillary-clinton-757-max-aa-swaps-a321neo-orders/.

[5] Libin Zhao, Tianliang Qin, Jianyu Zhang, and Yuli Chen. *3D Gradual Material Degradation Model for Progressive Damage Analyses of Unidirectional Composite Materials.* Article, Mathematical Problems in Engineering, 2015.

[6] Delia Brauer, Christian Rüssel, Sebastian Vogt, Jürgen Weisser, and Matthias Schnabelrauch. *Degradable phosphate glass fiber reinforced polymer matrices: Mechanical properties and cell response.* Article, Journal of materials science. Materials in medicine, 2008.

[7] Url:https://www.comsol.com/model/mixed-mode-debonding-of-a-laminated-composite-19961.

[8] Katarzyna Makyla Claudiane Ouellet-Plamondon Ingo Burgert Samuel Lorcher, Thomas Winkler and Nico Bruns. *Mechanical unfolding of a fluorescent protein enables self-reporting of damage in carbon-fiber-reinforced composites.* Article, Journal of Materials Chemistry A, 2014.

[9] E. Carrera, M. Cinefra, E. Zappino, and M. Petrolo. *Finite Element Analysis of Structures Through Unified Formulation.* 2014.

[10] Marianna Maiarù. *Multiscale approaches for the failure analysis of fiber-reinforced composite structure using the 1D CUF.* Tesi di dottorato, Politecnico di Torino, 2012.

[11] Olaf Schenk Cosmin G. Petra and Mihai Anitescu. *Real-time stochastic optimization of complex energy systems on high-performance computers.* Article, IEEE Computing in Science & Engineering, 2014.

[12] Miles Lubin Cosmin G. Petra, Olaf Schenk and Klaus Gartner. *An augmented incomplete factorization approach for computing the Schur complement in stochastic optimization.* Article, SIAM Journal on Scientific Computing, 2014.

[13] A. Pagani, A. G. de Miguel, M. Petrolo, and E. Carrera. *Analysis of laminated beams via Unified Formulation and Legendre polynomial expansions.* Article, Elsevier, 2016.

[14] E. Carrera, M. Maiarù, and M. Petrolo. *Component-wise analysis of laminated anisotropic composites.* Article, International Journal of solids and Structures 49, 2012.

[15] Anhony M. Waas Marianna Maiarù, Royan J. D'Mello. *Virtual Testing for the Mechanical Characterization of Cured Polymer Matrix Composites.* Article, American society for composites, 2017.

[16] Zdeněk P. Bažant and Byung Oh. *Crack Band Theory for Fracture of Concrete.* Article, Matériaux et Constructions, 1983.